Selection of the Mars Exploration Rover landing sites

M. P. Golombek,[1] J. A. Grant,[2] T. J. Parker,[1] D. M. Kass,[1] J. A. Crisp,[1] S. W. Squyres,[3] A. F. C. Haldemann,[1] M. Adler,[1] W. J. Lee,[1] N. T. Bridges,[1] R. E. Arvidson,[4] M. H. Carr,[5] R. L. Kirk,[6] P. C. Knocke,[1] R. B. Roncoli,[1] C. M. Weitz,[7] J. T. Schofield,[1] R. W. Zurek,[1] P. R. Christensen,[8] R. L. Fergason,[8] F. S. Anderson,[1,9] and J. W. Rice Jr.[8]

Received 26 February 2003; revised 23 July 2003; accepted 25 August 2003; published 10 December 2003.

[1] The selection of Meridiani Planum and Gusev crater as the Mars Exploration Rover landing sites took over 2 years, involved broad participation of the science community via four open workshops, and narrowed an initial ~155 potential sites (80–300 × 30 km) to four finalists based on science and safety. Engineering constraints important to the selection included (1) latitude (10°N–15°S) for maximum solar power, (2) elevation (less than −1.3 km) for sufficient atmosphere to slow the lander, (3) low horizontal winds, shear, and turbulence in the last few kilometers to minimize horizontal velocity, (4) low 10-m-scale slopes to reduce airbag spin-up and bounce, (5) moderate rock abundance to reduce abrasion or strokeout of the airbags, and (6) a radar-reflective, load-bearing, and trafficable surface safe for landing and roving that is not dominated by fine-grained dust. The evaluation of sites utilized existing as well as targeted orbital information acquired from the Mars Global Surveyor and Mars Odyssey. Three of the final four landing sites show strong evidence for surface processes involving water and appear capable of addressing the science objectives of the missions, which are to determine the aqueous, climatic, and geologic history of sites on Mars where conditions may have been favorable to the preservation of evidence of possible prebiotic or biotic processes. The evaluation of science criteria placed Meridiani and Gusev as the highest-priority sites. The evaluation of the three most critical safety criteria (10-m-scale slopes, rocks, and winds) and landing simulation results indicated that Meridiani and Elysium Planitia are the safest sites, followed by Gusev and Isidis Planitia. *INDEX TERMS:* 6225 Planetology: Solar System Objects: Mars; 5470 Planetology: Solid Surface Planets: Surface materials and properties; 5499 Planetology: Solid Surface Planets: General or miscellaneous; 5409 Planetology: Solid Surface Planets: Atmospheres—structure and dynamics; 5455 Planetology: Solid Surface Planets: Origin and evolution; *KEYWORDS:* Mars Exploration Rover, landing sites, remote sensing, aqueous climatic and geologic histories, Meridiani, Gusev

Citation: Golombek, M. P., et al., Selection of the Mars Exploration Rover landing sites, *J. Geophys. Res.*, *108*(E12), 8072, doi:10.1029/2003JE002074, 2003.

1. Introduction

[2] The Mars Exploration Rovers (MER) Mission is sending "twin" rovers named Spirit and Opportunity, to two different landing sites on Mars, each equipped with a sophisticated set of remote sensing and in situ instrumentation [*Crisp et al.*, 2003]. The rovers will be used to characterize the geology of each landing site and address science questions related to past environmental conditions and water activity [*Squyres et al.*, 2003]. After a 7-month cruise to Mars, the first rover will land on 4 January 2004, and the second one on 25 January 2004. The entry, descent, and landing system is similar to the one used for Pathfinder in 1997. The spacecraft, inside a heat shield, enters the Martian atmosphere directly from the hyperbolic approach trajectory (Figure 1). Approximately 8.5 km above the surface a parachute is deployed, which slows the velocity down from about 430 to 75 m/s. After 20 s, the heat shield drops away. This is followed 10 s later by the lander deploying below the backshell on a 20 m bridle or tether.

[1]Jet Propulsion Laboratory, California Institute of Technology, Pasadena, California, USA.
[2]Center for Earth and Planetary Studies, National Air and Space Museum, Smithsonian Institution, Washington, DC, USA.
[3]Department of Astronomy, Cornell University, Ithaca, New York, USA.
[4]Department of Earth and Space Sciences, Washington University, St. Louis, Missouri, USA.
[5]U.S. Geological Survey, Menlo Park, California, USA.
[6]U.S. Geological Survey, Flagstaff, Arizona, USA.
[7]NASA Headquarters, Washington, DC, USA.
[8]Department of Geological Sciences, Arizona State University, Tempe, Arizona, USA.
[9]Also at Hawaii Institute of Geophysics and Planetology, School of Ocean and Earth Science and Technology, University of Hawaii, Honolulu, Hawaii, USA.

0148-0227/03/2003JE002074$09.00

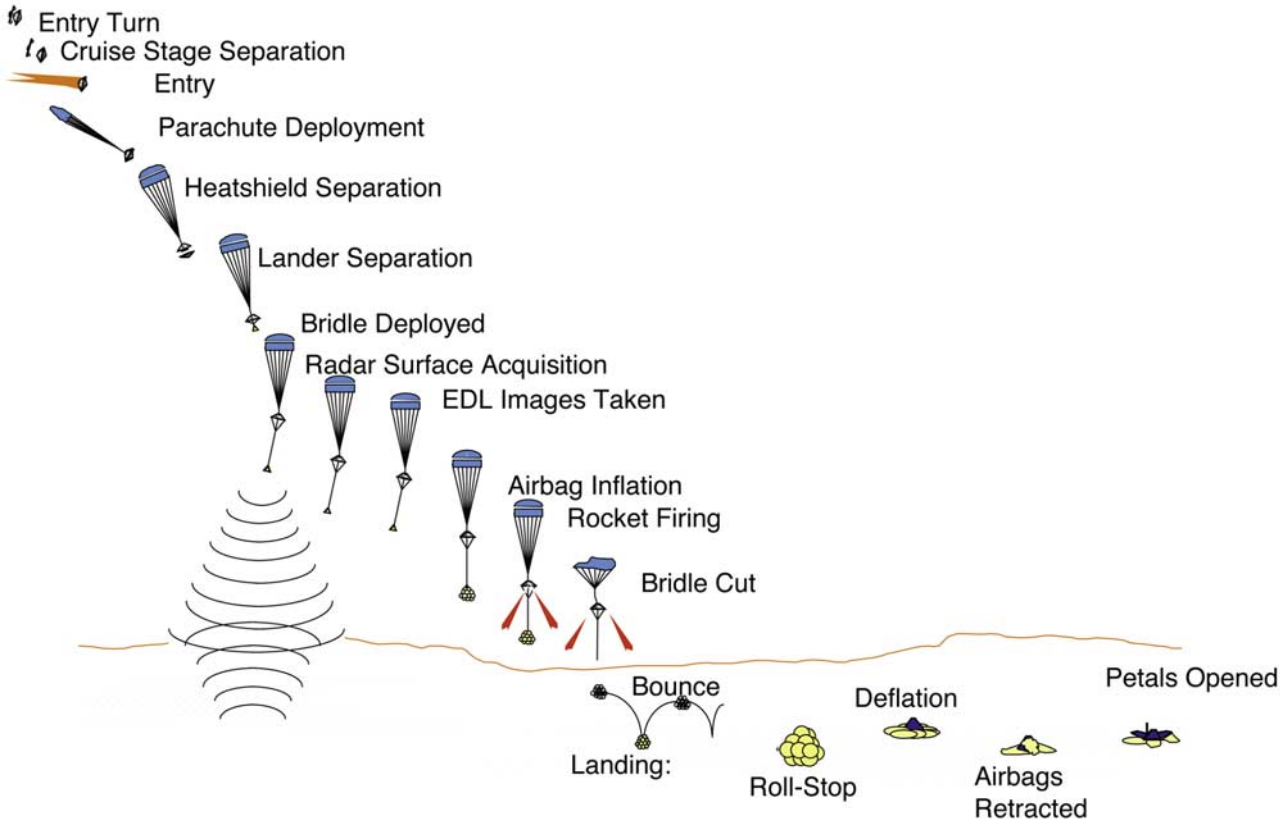

Figure 1. Illustration of the entry, descent, and landing sequence of the Mars Exploration Rover (MER) landers. See [*Crisp et al.*, 2003] for a description of the spacecraft configuration.

A series of descent images are taken and processed to determine the direction and magnitude of the horizontal velocity relative to the surface. At about 2.4 km above the surface, the radar altimeter acquires the ground and triggers inflation of the airbags that surround the lander. Retrorockets start firing at about 115 m above the ground to bring the vertical velocity to near zero (at about 15 m). If necessary, transverse rockets on the backshell are also fired to reduce horizontal velocity. The bridle is cut at about 15 m above the surface, releasing the airbag landing system, which then impacts the surface and bounces many times, likely traveling up to a kilometer before coming to rest. The airbags are deflated and retracted, and the lander petals open so that the rover can stand up and drive off. The rover carries its own computer and antennas for communication with orbiters and directly to Earth. The mobility system is capable of up to 40 m drive distance in one Martian day (a Sol), and the total mission odometry is expected to be at least 600 m. A stereo panoramic camera [*Bell et al.*, 2003] and infrared spectrometer [*Christensen et al.*, 2003b] scan the surrounding terrain and sky from a mast height of 1.5 m. A robotic arm carries a rock abrasion tool [*Gorevan et al.*, 2003], Mössbauer spectrometer [*Klingelhöfer et al.*, 2003], alpha particle X-ray spectrometer [*Rieder et al.*, 2003], and a Microscopic imager [*Herkenhoff et al.*, 2003] for close-up examination of rocks and soils. The mission lifetime is expected to be at least 91 Martian sols (93.5 Earth days).

[3] The process used for selection of the MER landing sites was broadly based on that used for selection of the Mars Pathfinder landing site [*Golombek et al.*, 1997a], including a close coordination between the engineering and science teams to identify potential landing sites and assess their safety and involvement of the science community via a series of open workshops. Like previous site selection efforts, selection of landing sites for MER has involved two parallel and intertwined activities. First, the engineering constraints on the landing site were defined based on preliminary spacecraft design and the landing scenario. These engineering constraints on the landing site were continually revised and reassessed as the spacecraft design matured and as testing was conducted. At the same time, the preliminary engineering constraints were mapped into suitable areas of Mars (i.e., elevation and latitude constraints) and the search for potential landing sites began early to allow time for the acquisition of new remote sensing data by operating orbital spacecraft (initially Mars Global Surveyor, MGS, and later Mars Odyssey). Environmental information was provided to the engineers to aid in spacecraft design as more information was gathered and analyzed. These two activities (defining the engineering constraints and searching for potential sites) were iterative, with the results of one affecting the other. As an example, changes in ellipse size based on tracking methods and the number and time of trajectory correction maneuvers rippled through the identification of potential landing sites after the initial definition, and lander susceptibility to horizontal winds had a major impact on site selection three fifths of the way through the process. Site safety has been of paramount importance in this landing site selection effort (like all to date), for the simple reason that the spacecraft

Table 1. Major MER Landing Site Activities

Date	Event/Activity
Sept. 2000	Preliminary MER engineering constraints identified.
Sept. 2000	One hundred eighty-five potential sites identified based on accessible terrain/engineering constraints.
	Invitation made to the Science Community to identify additional sites.
Jan. 2001	**First Open Community Landing Site Workshop held at NASA Ames, California.**
	Included presentation and discussion of all proposed sites.
	Used community consensus to prioritize based on science/safety requirements.
	Identification of seven highest priority and 17 other sites (some with multiple ellipses).
	Highest priority targeted for "ROTO"[a] MOC imaging, others nadir-only[b] imaging.
March 2001	Refined thermal inertia and albedo requirements of potential landing sites.
	Resulted in elimination of first primary Elysium site and some nadir sites.
June 2001	Remaining Ganges and Candor Chasma sites eliminated based on landing safety concerns.
Aug. 2001	MER Project approves TCM-5/DeltaDOR tracking, thereby reducing ellipse size slightly.
	Leads to search for new sites by Steering Committee, Community, and Project.
	Search included review of sites previously proposed for Mars 2001 Lander.
	Process identified nine new sites, including Athabasca Vallis in Elysium.
Sept. 2001	Refined landing safety and engineering concerns caused growth of ellipses.
	Leads to elimination of three of the new TCM-5/DeltaDOR ellipses.
Oct. 2001	**Second Open Community Landing Site Workshop held in Pasadena, California.**
	Discussion of sites in context of mission science and safety requirements.
	Selected four ellipses/regions and two alternate sites based on community voting.
	Primary sites: Meridiani Planum, Gusev Crater, Melas, Athabasca Vallis.
	Alternate sites: Isidis Planitia and Eos Chasma.
	MOC image acquisition focused on the four primary and two alternate sites.
	Project begins detailed evaluation of primary sites.
	Project decisions made on amount of MOC coverage desired for sites.
Jan. 2002	Athabasca Vallis demoted to alternate site, Isidis Planitia elevated to primary.
	Decision based on radar reflectivity in Athabasca and potential decimeter roughness.
	Mars Odyssey THEMIS imaging begins of sites remaining under consideration.
March 2002	**Third Open Community Landing Site Workshop held in Pasadena, California.**
	Discussion of remaining sites in context of MER-testable hypotheses.
	Provided first look at THEMIS images of the remaining sites.
	Sites evaluated on the basis of science, safety, and public engagement criteria.
	Retained Meridiani, Gusev, Isidis as primary sites; Athabasca as alternate.
	Eliminated Melas and Eos due to expected high winds and slopes.
	Later eliminated Athabasca due to radar roughness.
June 2002	Identified two Elysium "Wind Safe" sites; initiated by results of wind models.
Aug. 2002	**Steering Committee Meeting held at Arizona State University to review THEMIS data.**
	Selected EP78B2 "Wind Safe" site, discussed site science context.
Oct. 2002	Continued imaging of four remaining sites by MOC and THEMIS.
	Defined MOC stereo coverage and resolution desires and THEMIS coverage for sites.
Jan. 2003	**Fourth Open Community Landing Site Workshop held in Pasadena, California.**
	Confirmed Meridiani Planum and Gusev Crater as highest-priority science sites.
	Generated site-specific lists of testable hypotheses for remaining sites.
	Created lists of science "pros" and "cons" for each site.
Jan. 2003	**Athena Science Team Meeting in Pasadena, California.**
	Near-unanimous support for Meridiani and Gusev as highest-priority science sites.
	If Gusev and Isidis eliminated, near-unanimous support for Meridiani and Elysium.
	Above is favored over sending both vehicles to Meridiani.
	If necessary to choose a single site, 2:1 margin for Meridiani over Gusev.
Feb. 2003	**Project recommendation of Gusev for MER-A and Meridiani for MER-B.**
	On the basis of sites satisfying safety and engineering parameters as well as science.
March 2003	**External peer review of landing site selection and process.**
	Approved of project recommendation and selection process.
April 2003	**NASA Headquarters selected Meridiani and Gusev landing sites.**
	Dr. Ed Weiler, Associate Administrator for Space Science was selecting official.
	Accepted slightly greater risk at Gusev for greater potential science return.

[a]ROTO imaging with the Mars Orbiter Camera (MOC) involves rotating laterally off track.
[b]Nadir imaging with MOC involves downward viewing without changing spacecraft orientation.

must land safely before any science results can be obtained. Any other approach would place both the mission and the program at risk.

[4] The landing site selection process for MER has spanned more than two and a half years and incorporated the participation of broad sections of the planetary sciences community (Table 1). The process began with definition of preliminary science and engineering constraints for the mission in September 2000, and the identification of 185 potential landing ellipses on Mars. These sites were prioritized according to their science potential at the first open community landing site workshop held in January 2001 and about 25 sites were targeted for acquisition of MGS Mars Orbiter Camera (MOC) images. Six sites were selected for more detailed analysis at the Second Landing Site Workshop in October 2001. Additional MOC images and Mars Odyssey (which had just arrived at Mars) Thermal Emission Imaging System (THEMIS) images were also acquired of these sites. The six sites were evaluated in detail (and prioritized) in terms of both science and safety at the Third

Table 2. Mars Landing Site Steering Committee Membership

Name	Affiliation
John Grant[a]	Smithsonian Institution
Matthew Golombek[a]	Jet Propulsion Laboratory
Michael Carr	U.S. Geological Survey, Menlo Park
Philip Christensen	Arizona State University
Jack Farmer	Arizona State University
Virginia Gulick	NASA Ames Research Center
Bruce Jakosky	University of Colorado
Michael Malin	Malin Space Science Systems
George McGill	University of Massachusetts
Richard Morris	NASA Johnson Space Center
Timothy Parker	Jet Propulsion Laboratory
Roger Phillips	Washington University
Michael Shepard	Bloomsburg University
Kenneth Tanaka	U.S. Geological Survey

[a]Committee co-chairs.

Landing Site Workshop held in March 2002. Three sites were removed due to safety concerns at this workshop and a fourth site was added based on safety considerations. The Fourth Landing Site Workshop held in January 2003 confirmed two sites (Meridiani and Gusev) as the highest science priority sites and these two sites were endorsed near unanimously by the Athena Science Team (the NASA selected science team that is carrying out the mission [*Crisp et al.*, 2003; *Squyres et al.*, 2003]). The MER project also recommended the Meridiani and Gusev sites on the basis of safety and science in March 2003. This recommendation was endorsed and the selection process approved by an external peer review panel in late March 2003, and the Meridiani and Gusev landing sites were selected by NASA Headquarters in April 2003 (Table 1).

[5] A theme that has been adhered to throughout the landing site selection activities is that the process has been completely open to involvement by any and all interested parties and that there were no predetermined outcomes. In addition to broadcast invitations to the science community, several groups of individuals were specifically targeted for input and attendance at the landing site workshops. The first group comprised a Steering Committee (Table 2) that oversaw the site selection process and provided focused input upon request. Committee membership was largely NASA-appointed, with the exception of the two co-chairs, who were competitively selected, and was designed to encompass a range of critical experience and mission involvement. A group of ex-officio members from NASA Headquarters were invited to ensure participation of representatives from all active and planned Mars missions. Similarly, additional invitations were extended to individuals associated with ongoing or past missions. Finally, investigators receiving funding from the NASA Mars Data Analysis Program were solicited to ensure all relevant data sets were brought to bear in consideration of the proposed sites.

2. Landing Site Engineering Constraints

2.1. Ellipse Size

[6] The capabilities of the MER flight system and mission design define a set of engineering constraints (Table 3) on the safety of the landing site and the quality of the surface mission after landing. Both of these sets of mission success factors were evaluated across landing (99% probability) ellipses, which represent the accuracy to which a landing site can be targeted. The delivery geometry and uncertainty at atmospheric entry are the main drivers on the dimensions and orientation of the landing ellipse, and these characteristics vary with the site latitude and landing day (MER-A versus MER-B). The azimuth of the ellipse is driven by the approach trajectory with the major axis mostly in the direction of approach. The major axis dimension is dominated by the uncertainty in the entry flight path angle, which is driven by the uncertainty in the orbit determination before the final maneuvers. The orbit determination assumes radionavigation of carrier Doppler shift, time-of-flight ranging, and very long baseline interferometry (VLBI). Two different types of engineering margins were included in generating the ellipse sizes. First, margins were added to many of the fundamental orbit determination assumptions used to calculate the navigation delivery accuracy at Mars (e.g., Earth orientation parameters, nongravitational accelerations, etc.). Second, additional engineering margins are added to both the semimajor and semiminor axes of the landing ellipse to account for uncertainties not modeled in the entry, descent and landing Monte Carlo analyses (e.g., additional wind uncertainties, distance traveled from impact to roll stop, and inertial to cartographic map tie uncertainties). The ellipse size changed a number of times during the site selection effort, although all were smaller than previous ballistic entry ellipses at Mars, which for Mars Pathfinder were 200–300 km long down track and 100 km wide across track. Initial ellipse sizes that were used to identify prospective landing sites early in the process (section 5) varied in length with latitude from $\sim$340–80 $\times$ 30 km and were based on

Table 3. Summary of Landing Site Engineering Constraints

MER Mission Engineering Parameter	Requirement for MER Mission Landing Sites
Altitude	less than or equal to −1.3 km w.r.t. MOLA defined geoid
Approximate ellipse dimensions	$\sim$155 km $\times$ 16 km at 11°N, $\sim$96 km $\times$ 19 km at 15°S
Approximate ellipse orientation	$\sim$94° at 11°N to 76° at 15°S (clockwise from north)
Site separation	central angle $\sim$37°
Latitude (MER-A and MER-B)	5°N to 15°S and 10°N to 10°S
1 km length-scale slopes	must be less than 2°
100 m length-scale slopes	must be less than 5°
10 m length-scale slopes	must be less than 15°
Minimal relief	smooth and flat in Viking MDIM
Rock abundance	should be <20% (from thermal inertia)
Minimal hazardous rocks	Should be <1% larger than 0.5 m high
Trafficability	minimal decimeter-scale roughness from radar
Horizontal winds (shear/turbulence)	generally $\leq$0.9/$\leq$2.1 wrt MPF model
Horizontal winds (sustained mean)	must impact surface at <16–21 m/sec
Acceptable vertical winds	must impact surface at <12–15 m/sec
Minimum temperature at site	warmer than −97°C
Thermal inertia	greater than 200–250 SI units (see albedo)
Albedo	less than 0.18 and 0.26 (see thermal inertia)
Local dust environment	relatively dust-free from MGS TES thermal inertia, albedo, and dust index
Surface must be load bearing	radar and thermal inertia
Radar reflectivity	must be >0.03

ranging and two-way Doppler tracking of the spacecraft with five trajectory correction maneuvers (with the 4th, 8 days before entry and the 5th, 12 hours before entry). Incorporation of VLBI measurement techniques and moving the 5th trajectory correction maneuver to 2 days before atmospheric entry (and adding a contingency 6th opportunity for a maneuver 6 hours before atmospheric entry) yielded ellipses that were 95–155 × 16–20 km. These ellipses were used in the evaluation of the science objectives (section 9) and surface characteristics (section 11) of the sites. Ellipses used for siting the final sites (section 12.4) were based on updated analysis of margins and navigation delivery accuracy and varied from 80 to 115 km long and 10 to 12 km wide for MER-A and MER-B, respectively.

2.2. Elevation and Atmosphere

[7] Analysis of the entry, descent and landing system and atmospheric profiles for the season and time of arrival (described later) indicates that the MER spacecraft are capable of landing below −1.3 km, with respect to the MOLA (Mars Orbiter Laser Altimeter) defined geoid [*Smith and Zuber*, 1998]. This requirement stems mostly from the need for an adequate atmospheric density column to deploy the parachute, bring the spacecraft to the correct terminal velocity, and provide enough time for subsequent events (jettison the heat shield, separate the lander from the back shell, measure the descent rate with the radar altimeter, inflate the airbags and fire the solid rockets) to be completed before the lander hits the surface.

[8] Constant horizontal wind over the last few kilometers of the descent results in the lander's horizontal speed matching the wind speed. Unchecked, this horizontal velocity is added to the vertical velocity, possibly increasing the total impact velocity beyond the airbag capabilities. Wind gusts can also induce horizontal velocity through oscillations in the three-body system (parachute, backshell, and lander), resulting in the backshell pointing off vertical when the deceleration rockets fire. Three small horizontal rockets in the backshell can be fired either singly or in pairs to compensate either the affects of wind gusts or constant horizontal winds. By changing the attitude of the large descent rockets, these small horizontal rockets impart an effective velocity of about 27 m/s in one of six directions. This system can counter sustained winds of 35–50 m/s, bringing the tangential velocity of impact into a range that the airbags can survive. Similarly, the system can counter the effect of backshell angles up to roughly 20°. Significant changes in vertical winds between the radar solution and landing can also result in excessive impact velocities, however modeled winds at the sites show only small variations in the vertical component, so this was not a discriminator.

2.3. Latitude and Spacing

[9] The lifetime of the rover is determined by its ability to collect energy during the day, and its ability to use that energy to maintain thermal control during the night. During the day the rover will collect energy, heat up an insulated box containing the rover electronics, and charge batteries for use during the night. At night, the rover uses energy from the batteries, the stored thermal energy in the insulated box, and heat energy from radioisotope heater units to keep from getting too cold. The rover cannot survive the night when the energy it is able to collect and store is less than the energy needed to survive nighttime temperatures. As a result, landing sites near the subsolar latitude will receive more solar energy with a cosine loss for angles off of 90°, mitigated slightly by atmospheric diffusion of the light. The subsolar latitude starts at around 13°S (at the landing of MER-A) and heads north through the required 90 sol lifetimes of MER-A and MER-B. The lifetime requirement, the assumed solar panel degradation due to dust accumulation, and the modeled nighttime temperatures resulted in landing site latitude constraints of 15°S to 5°N for MER-A and 10°S to 10°N for MER-B.

[10] The MER rovers return approximately 70% of their data through the Odyssey and Mars Global Surveyor (MGS) orbiters. These relays can each only communicate with one rover at a time, and so if two rovers are too close to each other, then their data return would be reduced by the fraction of time that they had to share an orbiter pass. In the extreme case, if the rovers land at the same location, all orbiter passes would have to be shared, and the overall data return would be reduced by approximately 30%. In order to maximize the data return of both missions, the landing sites are constrained to be separated by at least 37° in central angle.

2.4. Slopes

[11] A radar altimeter measures the distance to the surface and the descent velocity. The final measurement is taken just before airbag inflation about 9 s before landing. If there are significant changes in the elevation between the final measurement and landing, then the lander altitude estimate will be incorrect, which is called "spoofing" the radar. In that case, the solution for when to fire the descent rockets and when to cut the bridle in order to minimize the impact velocity will be incorrect, possibly resulting in an impact that exceeds the capability of the airbag system. The lander can move on the order of 100 m horizontally between the last radar solution and landing. The altitude change over that distance should be limited to less than 9 m, which gives maximum slopes at these scales of about 5°.

[12] The multiple bounces of the lander on a relatively flat surface with an overall tilt in one direction could cause the lander to bounce in that direction and experience an increase in energy instead of a decrease. This would lead to an excessive impact velocity and system failure. Such failures can be avoided if slopes on the scale of 1 km are limited to about 2° or less.

[13] High slopes on the scale of the airbags (∼10 m), can result in an increased chance of failure through inopportune conversions between horizontal and vertical velocity. For example, the lander may have a barely acceptable combination of horizontal and vertical velocity on the first impact, but the encountered slope results in bouncing the lander straight up. The vertical velocity on the second impact then exceeds the capability of the airbags, and the system fails. As a rough guide, the slopes at the ∼3 m scale should not exceed 15° in order to avoid these failures. Finally, extreme roughness at the scale of the rover wheel (26 cm diameter) is probably not trafficable.

2.5. Rocks

[14] Rocks can cause failure of the airbags by ripping the outer layers or by tensile failure of the interior bladder

against triangular or pyramid shaped rocks. Ripping of the outer layers is exacerbated by high tangential velocity. Tensile failure of the inner bladder is more likely with high normal velocity, although this failure has been largely ameliorated by the addition of a second interior bladder. In either case the system failure is not immediate, but rather the failure of the bladder results in a loss of pressure, increasing the risk of failure on the next impact. The airbags have been repeatedly successful in tests against rocks 0.5 m high, and engineering analysis suggests that the likelihood of failure does not increase significantly until the height exceeds 0.7 m. For rocks higher than 0.7 m, the hazardous nature of the rock increases slowly with increasing height as a function of the lander velocity at impact and orientation of the lander (tetrahedral corners having less stroke than tetrahedral faces). Airbag drop tests on 0.5 m high rocks show they can withstand total impact velocities as high as 26 m/s, normal impact velocities as high as 16 m/s, and surface impact grazing angles as low as $\sim$15°. Initially based on the Mars Pathfinder constraint [*Golombek et al.*, 1997a], an upper limit of 20% rock coverage was set on the landing sites, which corresponds to roughly 1% area covered by 0.5 m high rocks based on rock size-frequency distributions [*Golombek and Rapp*, 1997]. Because simulations suggest the first four and occasionally one in the next six bounces may be energetic enough to cause failure if the lander is traveling at a high velocity, a large area is sampled by the lander (9–17 m^2 per bounce) and the probability of impacting a potentially hazardous rock rises significantly for areas with >10% rock coverage [*Golombek et al.*, 2003b]. Tests show that the rovers can drive through areas with 20% rock coverage, although progress slows with rock abundances >15%.

2.6. Radar Reflectivity and Surface Dust

[15] The radar altimeter requires a radar reflective surface to properly measure the closing velocity. Areas with weak radar echoes, generally interpreted as very dusty areas with low bulk densities are not suitable. Such areas may not be load bearing, which would inhibit rover operations. Dust could also coat rocks, obscuring their composition and/or mineralogy to remote sensing instruments and dust could be deposited on the solar panels, reducing the surface mission lifetime. The descent imaging and processing system requires an adequate surface contrast in order to locate and match features for the measurement of horizontal velocity and very dusty areas have uniform albedo, which could impede the effectiveness of this system. Finally, very dusty areas have high albedo and low thermal inertia, which results in cold near-surface atmospheric temperatures. Nighttime temperatures below −97°C would limit mission lifetime and the spacecraft was not qualified to temperatures colder than −120°C (which may be insufficient margin below this nighttime temperature) during thermal vacuum testing.

3. Potential Landing Sites

[16] The three main constraints on identifying potential areas to land on Mars are elevation, latitude and surface dust. MOLA data were used to define acceptable elevations within 15° of the equator, which was the preliminary latitude band acceptable for MER landing (Figure 2). Because the southern hemisphere of Mars is dominantly heavily cratered highlands, little area is actually below −1.3 km in elevation for MER-A (5°N to 15°S); the largest region below this elevation is in southern Elysium and Amazonis Planitiae. Unfortunately, most of this area (150°W to 200°W) is dominated by extremely low thermal inertia (interpreted to be covered by potentially thick deposits of dust), with fine component thermal inertias below 125 J m^{-2} $s^{-0.5}$ K^{-1} or SI units and so was excluded. For the latitude band of MER-B (originally 15°N to 5°S, later 10°N to 10°S), more area is below −1.3 km elevation. Nevertheless, most of the area between 135°W and 190°W is excluded on thermal inertia grounds. Areas available to seek landing sites are thus reduced to southern Isidis and Elysium Planitiae in the eastern hemisphere and western Arabia Terra, Terra Meridiani, Xanthe Terra, Chryse Planitia, and the bottom of Valles Marineris in the western hemisphere. These areas which satisfy the basic engineering requirements of the mission represent just 5% of the surface area of Mars and form the starting locations to begin identifying potential landing ellipses.

[17] Three-σ (99% probability) landing ellipses were placed in all locations that are below −1.3 km in elevation, have acceptable fine component thermal inertia values (>125–165 SI units), and are free of obvious hazards in the MDIMs (Mars Digital Image Mosaics [*U.S. Geological Survey* (*USGS*), 2001]). Only sites that appear smooth and flat in the MDIM without scarps, large hills, depressions or large fresh craters (>5 km) were acceptable [*Golombek et al.*, 2001]. For MER-A, preliminary ellipses varied linearly in length and azimuth from 77 × 30 km, oriented at 66° at 15°S, to 219 × 30 km, oriented at 88° at 5°N. For MER-B, preliminary ellipses varied linearly in length and azimuth from 130 × 30 km, oriented at 79° at 10°S, to 338 × 30 km, oriented at 99° at 10°N.

[18] Nearly 200 potential landing ellipses met these initial criteria: 100 ellipses for MER-A and 85 for MER-B (Figure 2). Even though the area available to land north of the equator is at least twice as great as south of the equator, the smaller ellipse size toward the south compensates. Geologic units accessible are diverse and range from Noachian Plateau dissected, hilly, cratered, and subdued cratered units to Hesperian ridged plains, channel materials, and the Vastitas Borealis Formation to Amazonian smooth plains, channel materials, volcanics, knobby materials, and the Medusae Fossae Formation [*Scott and Tanaka*, 1986; *Greeley and Guest*, 1987].

4. Science Objectives

[19] Each MER rover carries the Athena science payload [*Squyres et al.*, 2003], which is a suite of scientific instruments and tools for geologic exploration of the Martian surface. The rovers may be thought of as robotic field geologists. Their task is to search for evidence of past aqueous activity and, especially, to assess the past habitability of the environment in which the rocks at the landing sites formed. The essential scientific driver for landing site selection is therefore the likelihood that past aqueous activity may have created a habitable environment, and the likelihood that evidence for past habitable conditions

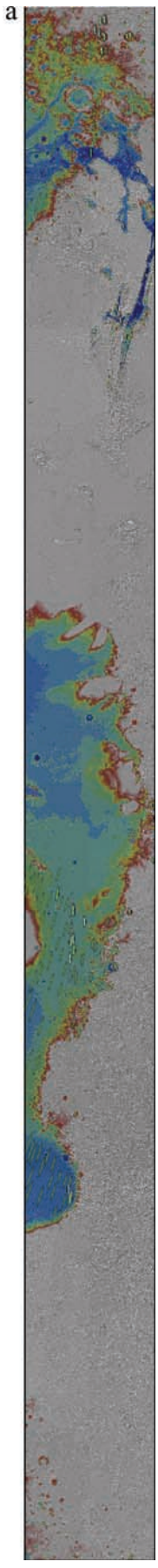

will be preserved in a form that can be studied using the Athena payload.

[20] The Athena payload is described in detail elsewhere in this issue. The topography, morphology, and mineralogy of the scene around each rover will be revealed by Pancam [*Bell et al.*, 2003] and Mini-TES [*Christensen et al.*, 2003b]. Pancam is a high-resolution, multispectral stereo camera. Mini-TES is an infrared spectrometer that produces high spectral resolution images in the wavelength range of 5–29 μm. Once promising targets have been identified using Pancam and Mini-TES, they will be studied in more detail using two in situ compositional instruments mounted on an instrument arm. These are an alpha particle X-ray spectrometer (APXS) [*Rieder et al.*, 2003] for elemental chemistry and a Mössbauer Spectrometer (MB) [*Klingelhöfer et al.*, 2003] for the mineralogy of Fe-bearing species. The instrument arm also carries a Microscopic Imager (MI) [*Herkenhoff et al.*, 2003] that will obtain high-resolution images of the same materials for which compositional data will be obtained, as well as a Rock Abrasion Tool (RAT) [*Gorevan et al.*, 2003] that can remove the outer, potentially weathered, surface material of rocks, exposing fresh materials underneath for examination by all the instruments.

5. Initial Landing Site Identification

[21] Because the number of sites that meet the basic engineering constraints is large, the selection process used the science objectives of the mission as the main discriminator of sites to be investigated in detail. This contrasts markedly with previous site selection efforts for the Viking and Mars Pathfinder missions, in which the sites studied in detail were dominated by engineering considerations [*Masursky and Crabill*, 1976a, 1976b, 1981; *Golombek et al.*, 1997a]. Because of this approach, the evaluation of those factors that distinguish potential landing sites with respect to mission success for MER has had to go beyond what was required to only find the two safest sites. Furthermore, the safety evaluation for the MER landing sites has been exhaustive in the identification of all mission success factors that depend on the landing site environment, and in the generation of environmental models to address all of those factors quantitatively in the evaluation of mission success.

[22] The first landing site workshop occurred in January 2001 and included presentations on various aspects of

Figure 2. (opposite) Potential landing ellipses for MER-A and MER-B. (a) Equatorial slice of Mars, 15°N–15°S. Areas in gray are above −1.3 km elevation and are thus too high to land MER. Colored areas are lower in elevation (see elevation scale in Figures 2b and 2c) and form a western hemisphere section (top or right) and an eastern hemisphere section (bottom or left). The eastern portion of the eastern hemisphere section has thermal inertias too low and so was excluded. The remaining area is ~5% of the surface area of the planet. Potential MER-A ellipses are shown in gray; potential MER-B ellipses are shown in green. White ellipses are those recommended following the First Landing Site Workshop (Table 4). (b) Detail of the eastern hemisphere, 180°–280°W, with potential MER ellipses. (c) Detail of the western hemisphere, 0°–90°W, with potential MER ellipses.

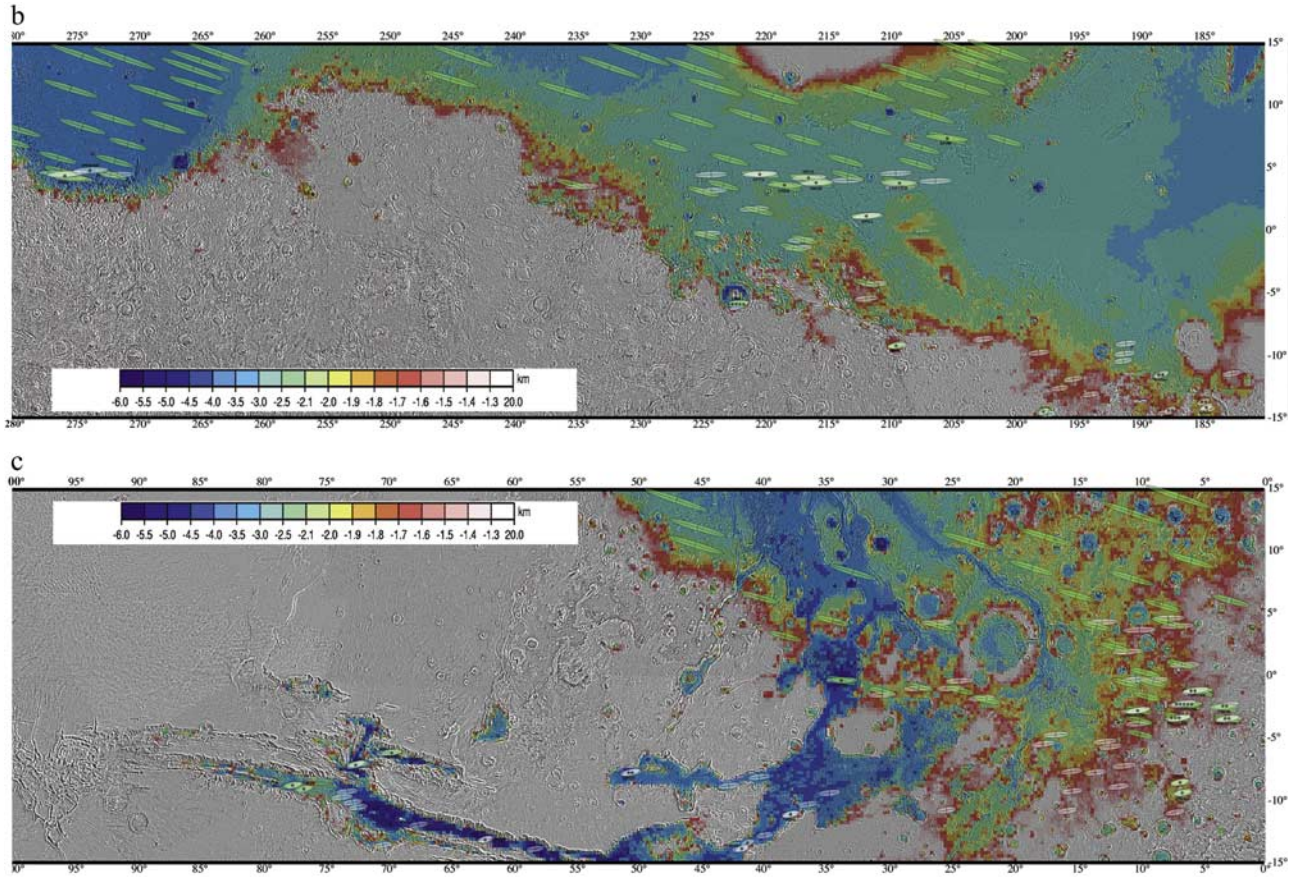

Figure 2. (continued)

landing site selection relevant for the MER missions. High-priority science sites were identified by the community and were targeted by MOC during the initial period of the extended mission. Roughly 30 ellipses were identified as high-priority science sites (Table 4), with remarkable consensus on one site, the Meridiani Planum (Hematite) site centered near 2°S, 2°W. This site was the subject of about 10 talks at the workshop and was recommended by 14 participants. Crater lakes were also a focus with multiple presentations for Gale, Gusev, and other crater lakes and similar fluvial outflow regions. Sites in Valles Marineris and outflow environs were also discussed as were sites in Elysium, Isidis and the highlands. Discussion at the workshop prioritized the sites into two groups that were subject to MGS MOC ROTO (Roll Only Targeted Observations), which were the highest-priority sites, and those that were only imaged (nadir) when the ground track went over the site (Table 4).

[23] Evaluation of the thermal environment of the spacecraft on the surface showed that extremely low temperatures (below −97°C) would reduce surface lifetime below the required 90 Sols. Evaluation of the near surface atmospheric temperatures showed that sites with bulk thermal inertias greater than a line defined by a thermal inertia of 270 SI units at 0.30 albedo and a thermal inertia of 210 at 0.10 albedo, would satisfy these temperature requirements [*Martin et al.*, 2003]. This places more stringent thermal inertia requirements on the landing sites than the initial identification and removed two sites in Elysium Planitia, one site at Apollinaris Patera and another in Durius Vallis from consideration in March 2001.

[24] Of the remaining sites, one site in Ganges Chasma and two sites in Candor Chasma were later eliminated (June 2001) on the basis of high topographic relief, steep scarps, and hummocky topography. This left about 17 sites in which ellipses were located and thermophysical properties gathered. These sites were: Meridiani Planum, Melas Chasma, Isidis Planitia, Gusev crater, Gale crater, Eos Chasma, NE and central Vallis Marineris, Meridiani crater, Boedickker crater, an unnamed crater (9°S, 209°W) and Meridiani highlands. Ellipses for these sites (that included margin) varied in length with latitude from 340 to ~80 × 30 km and were based on ranging and two-way Doppler tracking of the spacecraft with five trajectory correction maneuvers, the last of which would be 12 hours before entry.

[25] In the summer of 2001, the MER project evaluated the possibility of using simultaneous tracking of the spacecraft by two Deep Space Network stations (DeltaDOR). Preliminary results suggested ellipse sizes would be up to a factor of 2 smaller (without margin) [*Golombek et al.*, 2002]. Because landing sites of this size had never been evaluated for MER, new landing sites with ellipses that varied in length between 100 km at 10°N to about 40 km at 15°S were considered. All landing sites proposed for the '01 lander and all areas that had significant MOC coverage within the latitude and elevation bounds for MER that were at least as scientifically compelling as existing sites were

Table 4. Landing Sites Being Considered After the First Site Selection Workshop

Location	Location of Ellipse Center, deg	MER-A	MER-B	Geological Unit[a]	Elevation, km	Identifier
		Highest-Priority Sites[b]				
Eos Chasma	13.34S, 41.39W	X		Hch	−4.0	VM41A
Elysium Outflow	7.40N, 205.60W		X	Ael_1	−3.0	EP49B
Gale	5.81S, 222.23W	X		S	−4.5	EP82A
Gusev	14.85S, 184.16W	X		Hch	−1.9	EP55A (S)
Meridiani	2.50S, 3.30W		X	Npl_2	−1.3	TM21B
	1.99S, 6.01W		X	Npl_2	−1.3	TM20B
	1.20S, 5.30W		X	Npl_2	−1.3	TM19B
	2.20S, 6.60W	X		Npl_2	−1.7	TM10A
	1.20S, 5.60W	X		Npl_2	−1.3	TM9A
Isidis	4.64N, 275.88W		X	Aps	−4.0	IP98B
	4.7N, 274.68W	X		Aps	−4.5	IP85A
Melas Chasma	8.8S, 77.8W	X		Avf	−3.5	VM53A
	8.8S, 77.8W		X	Avf	−3.5	B Site
		High-Priority Sites[c]				
Apollinaris	~9.50S, 190.20W	TBD	TBD	AHa	−2	TBD
Boedickker Crater	15.30S, 197.44W	X		Npl_1	−2.1	EP64A
Central Valles Marineris	13.10S, 62.50W	X		Avf	−4.5	VM44A
Durius Valles	14.6S, 188.1W			Npl_1		EP56A
Meridiani	3.40S, 7.20W		X	Npl_2	−1.7	TM22B
	3.10S, 3.10W		X	Npl_2	−1.4	TM23B
	3.60S, 2.90W	X		Npl_2	−1.3	TM12A
	3.40S, 6.90W	X		Npl_2	−1.6	TM11A
Isidis	4.50N, 271.90W	X		Aps	−4.5	IP84A
	4.48N, 271.60W		X	Aps	−4.5	IP96B
Meridiani Crater	8.60S, 7.1W	X		S	−1.9	TM15A
	9.36S, 6.76W	X		S	−1.9	TM16A
Meridiani Highlands	3.00S, 10.00W	X		Hr	−1.8	TM13A
	2.80S, 10.10W		X	Hr	−1.8	TM24B
NE Valles Marineris Outflow	11.10S, 38.05W	X		Hch	−4.0	VM37A
Unnamed crater	9.20S, 209.60W	X		Npl_1	−1.7	EP69A

[a]Geological units from maps by *Scott and Tanaka* [1986] and *Greeley and Guest* [1987]. The first letter refers to the age: N, Noachian; H, Hesperian; and A, Amazonian. Hch, channel and chaotic material; Aps, smooth plains material; Ael_1, Elysium Formation (unit 1); Avf, Valles Marineris floor material; AHa, Apollinarus Patera Formation; Hr, ridged plains material; Npl_1, cratered plateau material; Npl_2, subdued crater plateau material; S, smooth crater floor material.

[b]Targeted by MGS MOC when accessible by rotating off the orbit track (ROTO) and during nadir passes.

[c]Targeted by MGS MOC during nadir passes only.

considered. Nine new locations met these criteria: Margaritifer Valles, Crommelin crater, two Athabasca Valles sites in Elysium Planitia, Ares Vallis tributary, Sinus Meridiani, Highlands (8°N, 12°W), and additional sites in Melas (SE) and Isidis.

[26] In September 2001, the MER project completed a full analysis of landing ellipse sizes that included DeltaDOR tracking, a 5th trajectory correction maneuver 2 days before atmospheric entry, a new arrival date for MER-B, and a full assessment of navigation errors and margin. The new arrival date for MER-B shifted the latitude band from the initial 15°N–5°S to 10°N–10°S. and corresponding landing ellipse lengths grew to 140–95 km, depending on latitude, with widths of 16–20 km. Three of these new sites (Margaritifer Valles, Crommelin crater, and SE Melas) were removed based on these longer ellipses.

[27] The remaining 24 sites were discussed at the Second Landing Site Workshop, 17–18 October 2001, in Pasadena, CA [*Golombek et al.*, 2002]. This workshop focused on evaluation of the science that can be accomplished at each site. Each site had a science spokesperson who discussed the science potential, the testable hypotheses, and specific measurements and investigations possible by the Athena science instruments at that site. In addition, safety considerations for the sites were discussed (ellipses did not fit within Gale, Boedickker, and the unnamed craters, or central and NE Valles Marineris, Table 4). Consensus was reached on four prime sites: Meridiani Planum (Figure 3), Gusev crater (Figure 4), Melas Chasma (Figure 5), and Isidis Planitia (Figure 6); and two backups: Eos Chasma (Figure 7) and Athabasca Valles (Figure 8). Ellipse locations were moved slightly after the workshop to improve their science potential or safety. Presentations at the workshop indicate all of the sites show evidence for surface processes involving water and appear capable of addressing the science objectives of the MER missions.

6. Data and Models Used to Evaluate Surface Characteristics and Safety

6.1. Introduction

[28] Unlike all previous landing site selection activities, MER had an unprecedented profusion of new information available and the ability to acquire data from two orbiting spacecraft during the selection process. In contrast, the Viking landing site selection activity relied mostly on Mariner 9 information prior to arrival and then an intense effort to find new sites after arrival when previously identified sites appeared too dangerous in orbiter images [*Masursky and Crabill*, 1976a, 1976b, 1981]. Although Mars Pathfinder had little new data since Viking, there was a much greater appreciation and models of how the

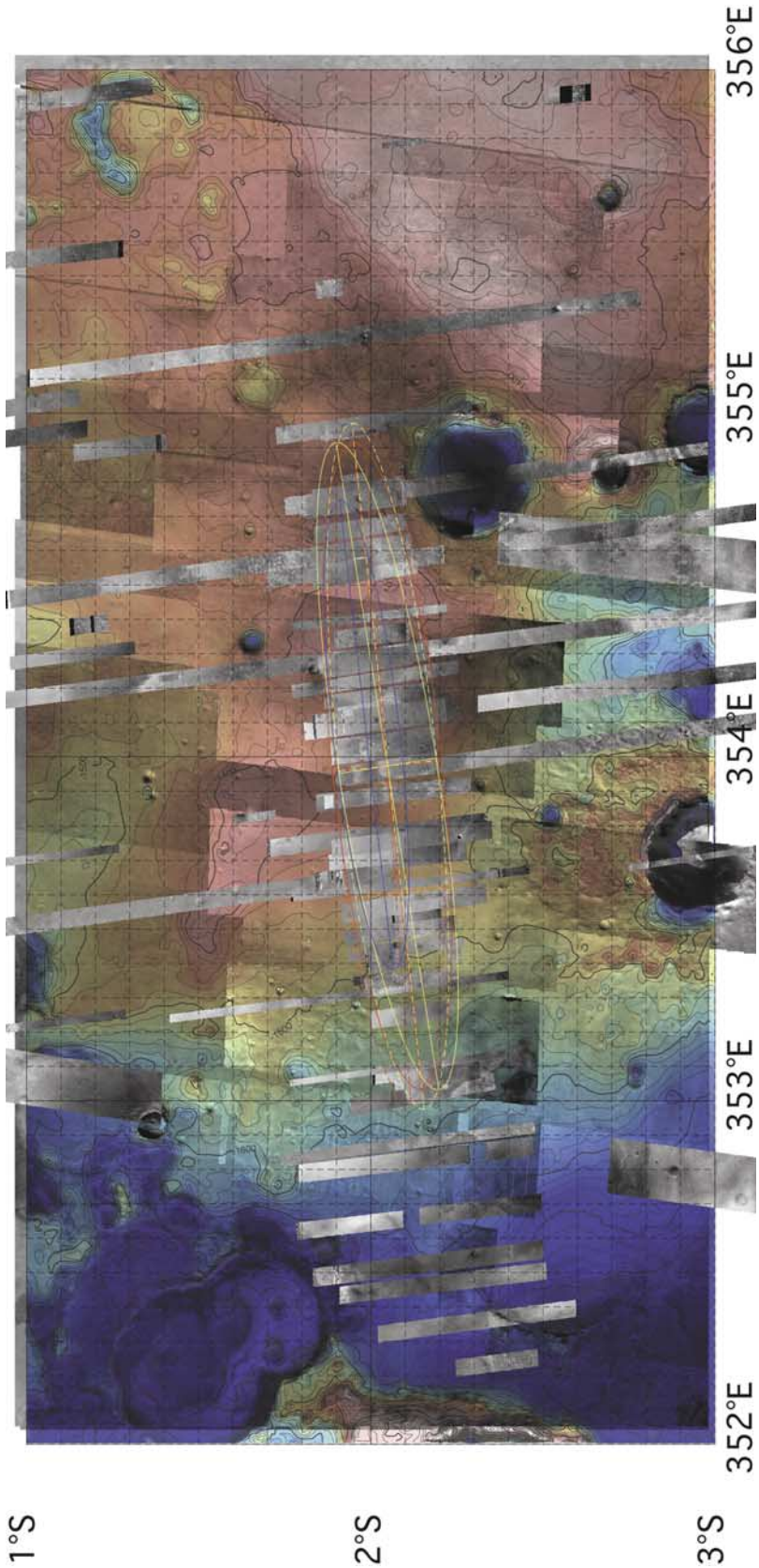

Figure 3. Meridiani Planum site mosaic. The background is the THEMIS daytime thermal (100 m/pixel) and visible (18 m/pixel) images, overlain by MOLA elevations in color (IAU 2000 grid). Thin image strips are MOC high-resolution images through R05 of the MGS extended mission. Wider image strips are THEMIS visible images at 18 m/pixel. Ellipse TM20B2 for MER-B, shown dashed in red, is 117 × 18 km, oriented at 86° for the opening of the launch window (solid for the close of the launch window). Ellipse TM10A2 for MER-A, shown dashed in yellow, is 119 × 17 km, oriented at 84° for the opening of the launch window (solid for the close of the launch window). The final ellipse, TM20B3 (in blue), is centered at 1.98°S, 354.06°E and is 81.5 × 11.5 km, oriented at an azimuth of 84.5°.

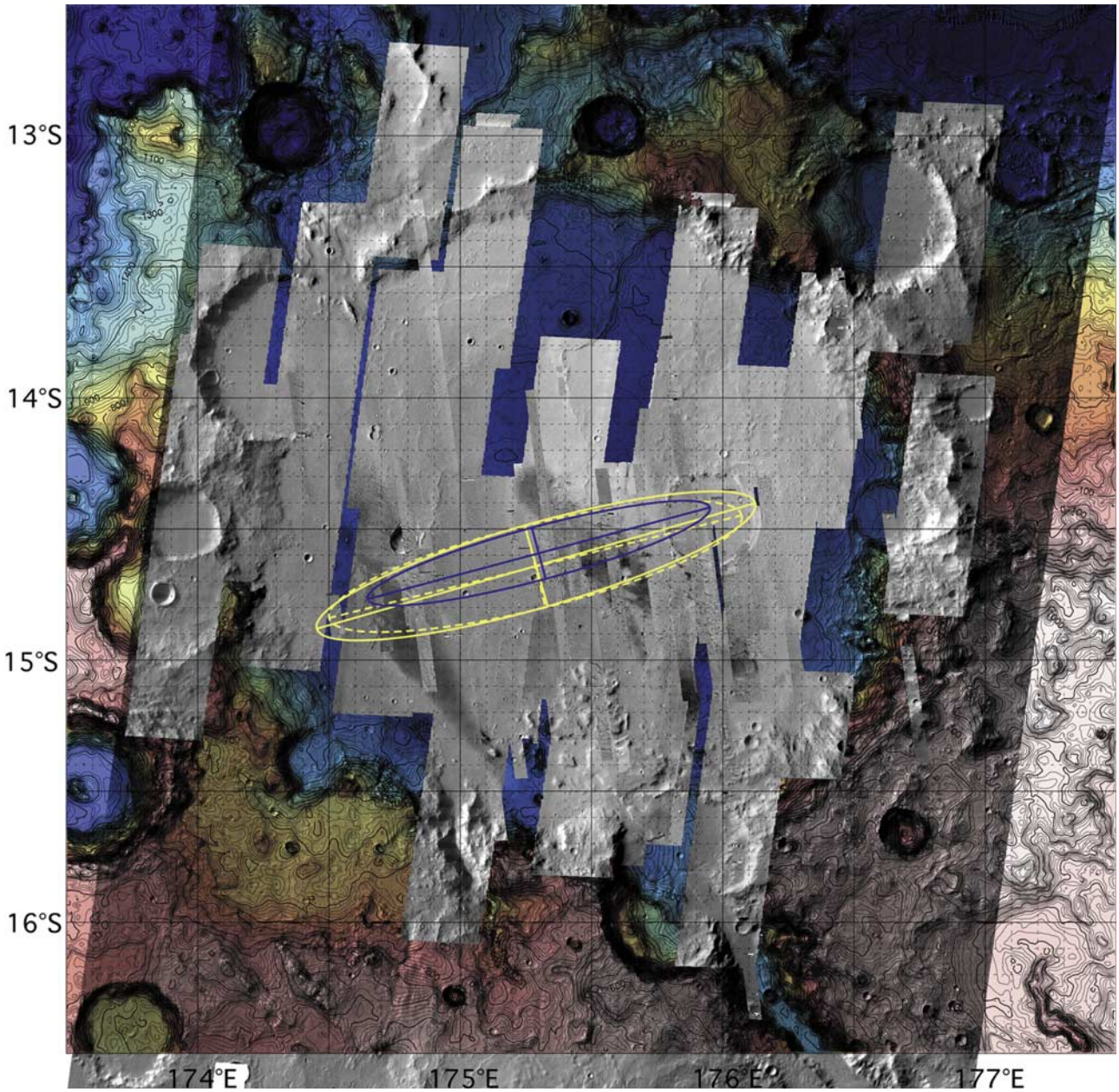

Figure 4. Gusev crater site mosaic. The background is the THEMIS daytime thermal images (100 m/pixel), overlain by MOLA elevations in color (IAU 2000). Thin image strips are MOC high-resolution images through R05 of the MGS extended mission. Wider image strips are THEMIS visible images at 18 m/pixel. Ellipse EP55A2 for MER-A, shown dashed in yellow, is 96 × 19 km, oriented at 76° for the opening of the launch window (solid for the close of the launch window). The final ellipse, EP55A3 (in blue), is centered at 14.59°S, 175.30°E and is 81 × 12 km, oriented at an azimuth of 75°.

VL1 (Viking Lander 1) and VL2 (Viking Lander 2) landing surfaces related to Viking Orbital data and a clear Earth analog [*Golombek et al.*, 1997a] that correctly predicted the surface characteristics of the landing site [*Golombek et al.*, 1997b, 1999]. In comparison, MER has received a plethora of new information from MGS and Odyssey that has resulted in the best-imaged, best-studied locations in the history of Mars exploration. These data have allowed the major engineering constraints and the science potential (including specific testable hypotheses) to be addressed in detail. Specific data used in the MER site selection effort include: Viking images, Viking Infrared Thermal Mapper (IRTM) data, data from the Viking and Mars Pathfinder landing sites, Earth-based radar, MGS MOLA, TES (Thermal Emission Spectrometer) and MOC data, and Mars Odyssey THEMIS data.

6.2. Viking Image Data

[29] At the start of the MER landing site selection process the digitally mosaiced Viking orbiter images (230 m/pixel)

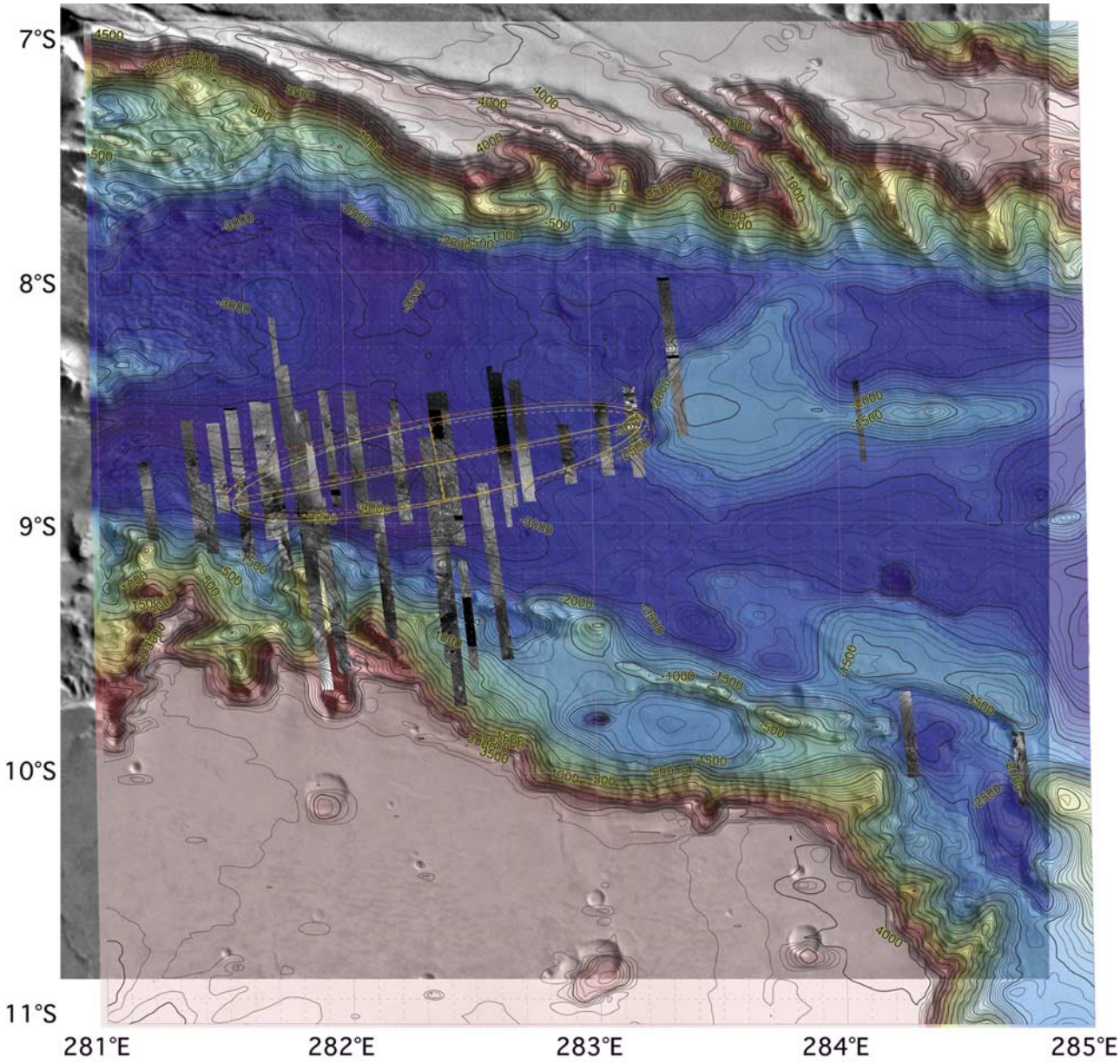

Figure 5. Melas Chasma site mosaic. The background is the Viking MDIM 2.0 mosaic, overlain by MOLA elevations in color (IAU 1991). Thin image strips are MOC high-resolution images through E11 of the MGS extended mission. Ellipse VM53B2 for MER-B, shown dashed in red, is 105 × 20 km, oriented at 82° for the opening of the launch window (solid for the close of the launch window). Ellipse VM53A2 for MER-A, shown dashed in yellow, is 103 × 18 km, oriented at 80° for the opening of the launch window (solid for the close of the launch window).

were used to assess areas that did not contain obvious scarps or slopes at about 1 km scale. This MDIM 2.0 version (planetographic, positive west longitude) was produced at the start of the MER landing site activity by the U. S. Geological Survey, Flagstaff [*USGS*, 2001] and included an improved cartographic frame that resulted from information gathered by the Mars Pathfinder mission.

6.3. MOLA Data

[30] For the first time, definitive elevation data were provided by MOLA [*Smith et al.*, 2001a] and when combined with gravity data [*Tyler et al.*, 2001] allowed the definition of the Martian geoid and its general relationship with atmospheric surface pressure [*Smith and Zuber*, 1998]. The initial definition of potential MER ellipses was made using the MDIM 2.0 and the MOLA elevations; potential ellipses had to be entirely smooth and flat in the MDIM 2.0 and be below −1.3 km. Standard mosaics produced for each landing site in this paper include the MDIM 2.0 and MOLA data as bases for placing higher-resolution images. MOLA topographic data in the mosaics were plotted on a positive east planetocentric coordinate system referenced to the IAU/

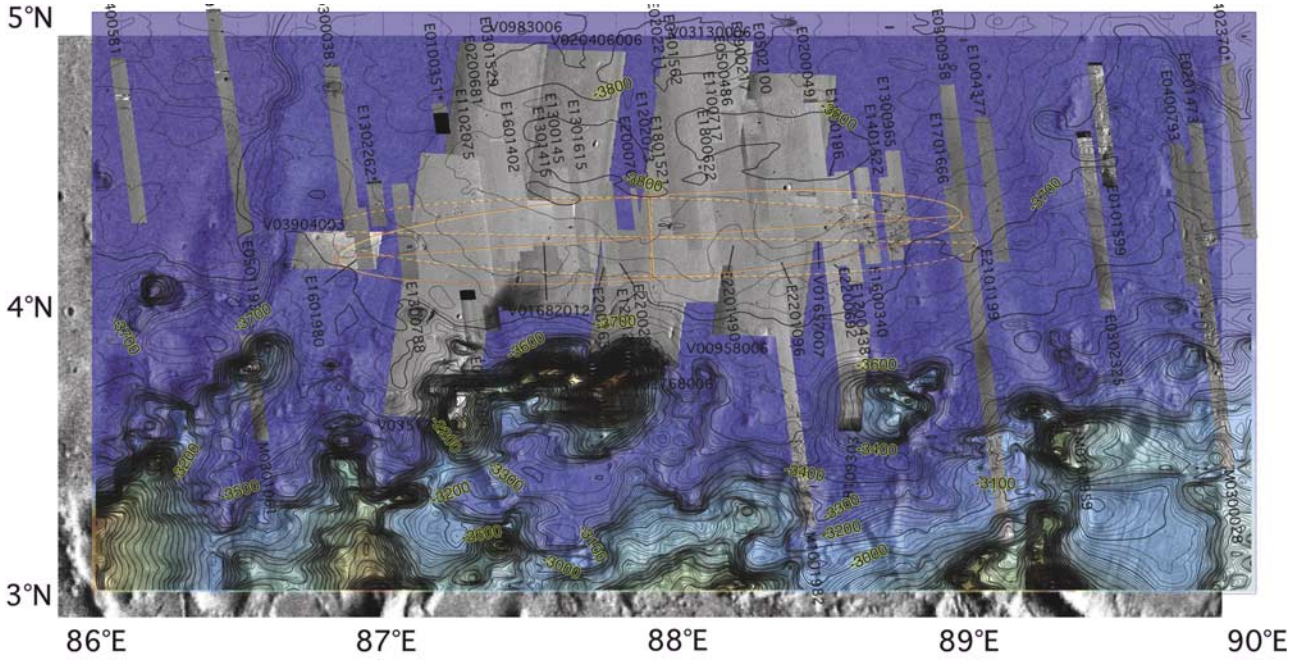

Figure 6. Isidis Planitia site mosaic. The background is the Viking MDIM 2.0 mosaic, overlain by MOLA elevations in color (IAU 1991). Thin image strips are MOC high-resolution images through E22 of the MGS extended mission. Wider image strips are THEMIS visible images at 18 m/pixel. Ellipse IP96B2 for MER-B, shown dashed in red, is 140 × 16 km, oriented at 91° for the opening of the launch window (solid for the close of the launch window). Ellipse IP84A2 for MER-A, shown dashed in yellow, is 132 × 16 km, oriented at 88° for the opening of the launch window (solid for the close of the launch window).

IAG 1991 system (available when site analysis began) that contained an offset from the MDIM 2.0. Final maps were referenced to the IAU/IAG 2000 frame, which can be easily converted to the inertia coordinates used by the spacecraft navigation team. MOLA data also provided definitive slopes at the 1 km scale as well as slopes at longer and shorter baselines down to the 300 m spacing between laser shots along orbit tracks [e.g., *Smith et al.*, 2001a; *Kreslavsky and Head*, 1999, 2000; *Aharonson et al.*, 2001]. The Allan variation (relief) at a number of length scales was used to infer roughness at smaller scales by extrapolation of the Hurst exponent [*Shepard et al.*, 2001; *Campbell et al.*, 2003; *Anderson et al.*, 2003]. At most of the landing sites these results generally compare favorably with estimates of roughness at the 75–150 m scale derived from the spread of the returned MOLA laser pulse, with and without the longer slopes subtracted out [*Garvin et al.*, 1999; *Smith et al.*, 2001a; *Neumann et al.*, 2003]. As a result, in addition to providing definitive elevations and geopotential surfaces for locating potential landing sites, MOLA data also directly assessed slopes at 1 km and 100 m scale, which are of engineering concern. Finally, gridded MOLA data were used to construct shaded relief maps to evaluate surface morphology and geology [e.g., *Smith et al.*, 2001a].

6.4. Thermophysical Properties

[31] Data on the thermosphysical properties of the surface include data from the Viking era, as well as from MGS and Odyssey. Thermal inertia measures the rate at which surface materials change temperature, which can be related to particle size and cohesion [*Kieffer et al.*, 1977; *Jakosky*, 1986; *Christensen*, 1986a; *Christensen and Moore*, 1992]. Surfaces dominated by loose dust have low thermal inertia and high albedo, whereas those dominated by rock or duricrust have high thermal inertia and typically (but not always) lower albedo. The fine component thermal inertia is the thermal inertia of the surface after the thermal radiance attributable to the rocky component is factored out [*Kieffer et al.*, 1977; *Christensen*, 1986b]. A combined digital data set of IRTM thermal inertia measurements was used that included (1) bulk inertia in 2° × 2° footprints [*Kieffer et al.*, 1977; *Palluconi and Kieffer*, 1981], (2) high-resolution bulk inertia in 0.5° × 0.5° footprints [*Christensen and Malin*, 1988], (3) rock abundance in 1° × 1° footprints [*Christensen*, 1986b], (4) fine component thermal inertia in 1° × 1° footprints [*Christensen*, 1982, 1986a, 1986b], and albedo in 1° × 1° footprints [*Pleskot and Miner*, 1981]. For initial MER ellipses, fine component thermal inertia had to be greater than 125–165 J m^{-2} $s^{-0.5}$ K^{-1} or as commonly abbreviated, SI units, to avoid surfaces dominated by potentially thick deposits of dust. These same data were used to help select the Pathfinder landing site [*Golombek et al.*, 1997a] and proved their worth by making predictions of surface characteristics that were ultimately verified by ground truth data returned by the Pathfinder lander [*Golombek et al.*, 1997b, 1999]. Acceptable thermal inertias for landed missions that are load bearing, trafficable and not dominated by loose dust are outlined in *Golombek et al.* [1997a].

[32] Later in the site selection process high-resolution TES thermal inertia and albedo became available, initially at

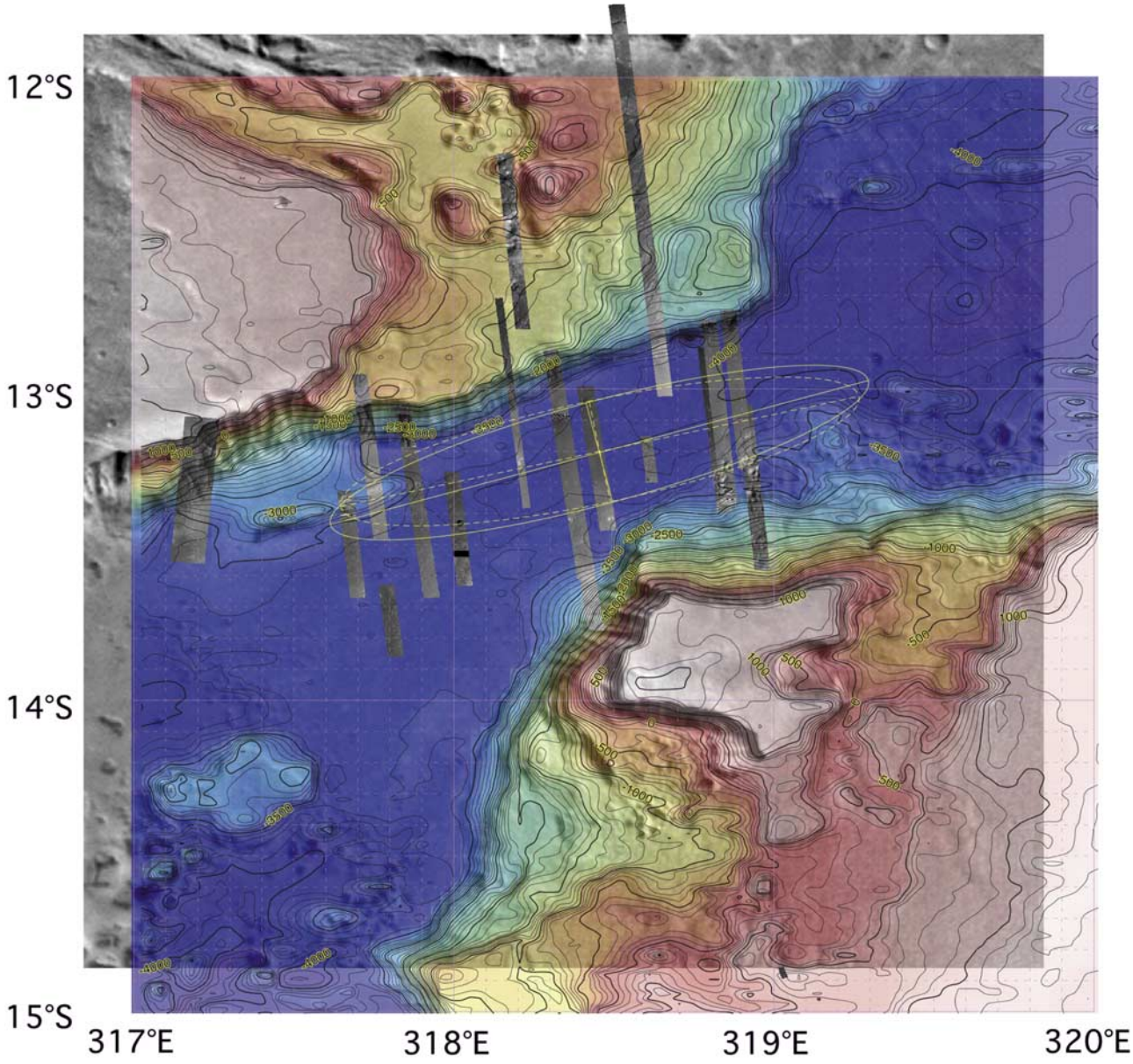

Figure 7. Eos Chasma site mosaic. The background is the Viking MDIM 2.0 mosaic, overlain by MOLA elevations in color (IAU 1991). Thin image strips are MOC high-resolution images through E04 of the MGS extended mission. Ellipse VM41A2 for MER-A, shown dashed in yellow, is 98 × 19 km, oriented at 76° for the opening of the launch window (solid for the close of the launch window).

broad 100 km scale [*Jakosky et al.*, 2000] and later in 15 km/pixel [*Mellon et al.*, 2000; *Christensen et al.*, 2001a] and at roughly 3 km/pixel bins [*Jakosky and Mellon*, 2001]. TES data confirmed the broad regions of low thermal inertia/high albedo observed in the IRTM data, but also showed more variability at smaller spatial scale, including the identification of areas with high thermal inertia [*Mellon et al.*, 2000], likely resulting from the greater presence of rock and duricrust [e.g., *Jakosky and Christensen*, 1986; *Mellon et al.*, 2000; *Golombek et al.*, 2003b]. The amount of dust cover at the landing sites was evaluated by the general thermal inertia and albedo and the TES dust index, which includes a more explicit measure of the particle size [*Ruff and Christensen*, 2002]. High-resolution TES thermal inertia data were also used to evaluate the surface properties of the landing sites [*Jakosky and Mellon*, 2001; *Pelkey and Jakosky*, 2002]. These data were used to evaluate the minimum 1 m atmospheric temperature requirement of −97°C that placed more stringent constraints on bulk thermal inertia, which had to be greater than a line defined by a thermal inertia of 270 SI units at 0.30 albedo and a thermal inertia of 210 SI units at 0.10 albedo [*Martin et al.*, 2003]. Finally, THEMIS daytime and nighttime thermal images at 100 m/pixel scale offered the ability to separate out thermophysical units that could be mapped contiguously across the surface [*Christensen et al.*, 2003a]. These images reveal the thermophysical properties of surface units at unprecedented scale, showing bare outcrop, rocky crater

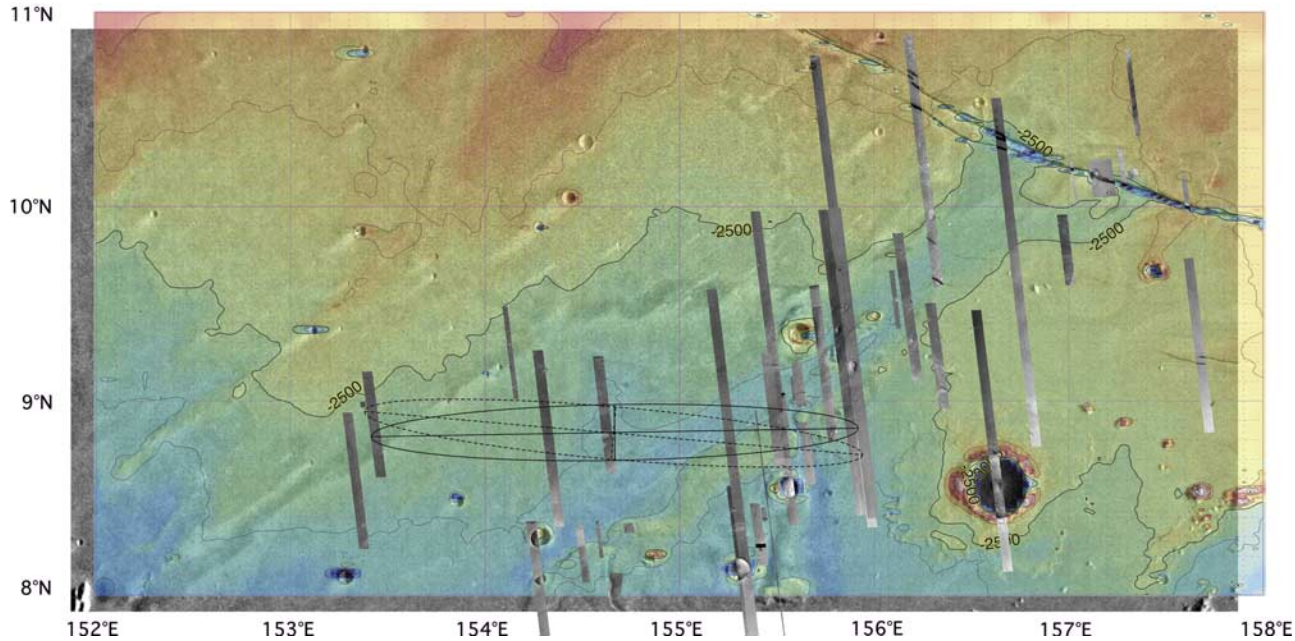

Figure 8. Athabasca Valles site mosaic. The background is the Viking MDIM 2.0 mosaic, overlain by MOLA elevations in color (IAU 1991). Thin image strips are MOC high-resolution images through E11 of the MGS extended mission. Ellipse EP49B2 for MER-B, shown dashed in black, is 152 × 16 km, oriented at 95° for the opening of the launch window (solid for the close of the launch window).

ejecta, areas covered by significant thicknesses of dust, and mapable areas with different thermal inertia. Nighttime thermal images also provided a predawn estimate of the surface temperature that were used to constrain the atmospheric temperatures the spacecraft will encounter.

6.5. Rocks

[33] Spectral differencing of the IRTM thermal data allow the separation of the high-inertia and low-inertia components of the bulk inertia [*Christensen*, 1982, 1986a, 1986b]. The models assume that rocky components make up the high-inertia component and are composed of rocks of diameter 0.1–0.15 m or greater. Despite the inability of distinguishing hazardous rocks from outcrop and nonuniform distributions of rocks possible over the scale of the pixel (1° latitude × 1° longitude), all three landing sites have rock abundance estimates within 20% relative to the IRTM value [*Christensen*, 1986b; *Moore and Jakosky*, 1989; *Moore and Keller*, 1990, 1991; *Golombek et al.*, 1999, 2003b]. Later preliminary TES estimates of rock abundance show similar average values at the landing sites, albeit with a greater range [*Nowicki and Christensen*, 1999]. However, these estimates were not validated in time for use in the MER site evaluation effort.

[34] Model rock size-frequency distributions for Mars based on the Viking landing sites and a wide variety of rocky locations on the Earth also allow an estimate of the number or area of rocks of any size range [*Golombek and Rapp*, 1997]. The cumulative fractional area versus diameter distributions follow simple exponential equations with the total area covered by all rocks provided by the IRTM estimate [*Christensen*, 1986b]. These models accurately predicted the overall rock distributions measured at the Mars Pathfinder landing site as well as the number and area of potentially hazardous rocks (diameters greater than 1 m or 0.5 m high) [*Golombek et al.*, 1999, 2003b]. *Golombek et al.* [2003b] uses these model distributions to calculate the probability of impacting potentially hazardous rocks at the prospective MER landing sites.

6.6. MOC and THEMIS Imaging Data

[35] Once specific landing sites were defined, requests were made to obtain high-resolution MOC images at 1.5–6 m/pixel [*Malin and Edgett*, 2001]. These images are at an unprecedented resolution allowing identification of features at scales approaching that of the airbag-encased lander (~3 m). Although these images cover a small area (typical landing site images were acquired at 3 m/pixel and are 3 km wide and a few tens of kilometers long), over time most of the high-priority sites and ellipses had received significant MOC coverage. These closely spaced MOC images in the ellipses allowed the first decameter-scale high-resolution photogeologic mapping on Mars. In addition, MOC images were acquired in both nadir views as well as pointed via ROTO maneuvers, which allowed the targeted acquisition of stereo images at ~3 m/pixel. Most nadir MOC images also have a MOLA elevation track that allows assessment of relief of features present in the images [*Anderson and Golombek*, 2001; *Soderblom and Kirk*, 2003; *Anderson et al.*, 2003]. Finally, THEMIS visible images at 18 m/pixel showed broader areas at intermediate resolution, which in most cases allowed the precise placement of MOC images within the ellipse mosaics.

[36] To obtain quantitative information on topography and slopes within the ellipses, digital stereogrammetry and two-dimensional photoclinometry (PC, known more

descriptively as shape-from-shading) have been applied to MOC narrow-angle images of the candidate landing sites [*Kirk et al.*, 2002, 2003; *Ivanov and Lorre*, 2002; *Beyer and McEwen*, 2002; *Beyer et al.*, 2003]. Because stereogrammetry is based on matching finite patches in two images, it yields digital elevation models (DEMs) with a horizontal resolution no better than 3 pixels, or 10 m for the 3 m/pixel MOC images used. Two-dimensional PC algorithms were therefore used to construct DEMs of selected image regions with single-pixel (~3 m) resolution [*Kirk et al.*, 2003; *Beyer and McEwen*, 2002; *Beyer et al.*, 2003]. The accuracy of these DEMs depends crucially on the validity of photometric assumptions [*Kirk et al.*, 2001]. While the surface photometry of Mars is adequately constrained [*Kirk et al.*, 2000], the atmospheric haze contribution to any given image is essentially an unknown. The PC analysis is therefore calibrated by choosing a haze estimate that gives results consistent with stereogrammetry. Such calibration can be uncertain to several tens of percent and is hence the leading error source in slope estimation by photoclinometry [*Kirk et al.*, 2003], but morphologic units at the landing sites are readily distinguished despite this level of error. Summary statistics of roughness derived from the DEMs produced by *Kirk et al.* [2003] provide an indication of the relative safety of different morphologic units in the landing sites and were used in numerical simulations of the landing process discussed in section 12. Slope maps of broad regions produced by point photoclinometry [*Beyer and McEwen*, 2002; *Beyer et al.*, 2003] were also used to delineate hazard units throughout the landing ellipses for comparison with one another and with photogeologic mapping results.

6.7. Radar Reflectivity and Roughness

[37] The MER landing depends critically upon the functioning of the on-board radar altimeter and decimeter to decameter length-scale roughness can negatively impact both landing and roving. Both of these properties can be addressed with Earth-based radar data. Scattering of X-band (3.5 cm wavelength) and S-band (12.6 cm) radar energy is controlled in different incidence angle regions by surface roughness elements at scales ranging from 1 to about 100 times the wavelength scale. Near nadir incidence backscattered energy is dominated by mirror-like, or specular reflections controlled by surface facets from 10 to 100 times the wavelength scale. The incidence angle dependence of this scattering behavior is described well for Mars by the Hagfors model [*Simpson et al.*, 1992; *Butler*, 1994; *Haldemann et al.*, 1997], which depends on normal reflectivity, and a roughness parameter, related to root-mean-square (RMS) slope. Beyond the 10° of nadir incidence, diffuse scattering is important. Diffuse scattering as a function of backscatter incidence angle is generally well fit by a cosine raised to some power (generally between 1 and 2). Diffuse scattering is controlled by scales of surface roughness at or near the wavelength scale, which, for example, can be associated with rocks. A more detailed summary of the interpretation of Earth-based radar data for landing site selection can be found in the work of *Golombek et al.* [1997a].

[38] Generally however, the radar data are best evaluated by comparing the information available for a proposed site with the information available from a known location, either on Mars or Earth. Further, the radar data should not be evaluated purely on their own merits, but in conjunction with other physical properties remote sensing data sets. *Haldemann et al.* [2003; Radar properties of the proposed Mars Exploration Rover landing sites, submitted to *Journal of Geophysical Research*, 2003, hereinafter referred to as Haldemann et al., submitted manuscript, 2003] review all available Earth-based radar backscatter behavior for all seven proposed landing sites as well as for both Viking sites and the Pathfinder site. Specular and diffuse scattering information is available at 3.5 cm for all the landing sites from Goldstone Solar System Radar (GSSR) delay-Doppler experiments and GSSR-VLA (Very Large Array), respectively. Several of the landing ellipses are sampled directly in both specular and diffuse scattering regimes. When this is not the case, *Haldemann et al*. [2003; submitted manuscript, 2003] rely on data available for the same Mars geologic unit as the ellipse. At 12.6 cm, Arecibo Observatory data and some GSSR data exist for most of the sites in either or both scattering regimes. When data are not directly available at S-band, *Haldemann et al*. [2003; submitted manuscript, 2003] resort to the scattering model parameters of *Moore and Thompson* [1991], which were based on GSSR 12.6 cm experiments and other remote sensing properties.

7. Atmosphere Definition

7.1. Vertical Structure of the Atmosphere

[39] The atmosphere is one of the key constraints on where missions can land on Mars. Of particular importance are the atmospheric density and vertical structure. They control a number of engineering issues in most landing systems. In particular, they define the maximum elevation at which a given system can land safely. The main factor controlling the atmospheric density (and thus the potential landing elevations) is the CO_2 seasonal cycle [*Zurek et al.*, 1992]. Unfortunately for MER, the missions will land near L_s ~335 which is near the minimum in the seasonal pressure cycle. This emphasized the need for accurate profiles of temperature (T, in K), pressure (p, in mbar) and density (ρ, in kg/m^3) versus altitude (z, in km relative to the MOLA geoid).

[40] An atmospheric profile is affected by weather and other time varying phenomena. Thus it is necessary to investigate the climatology for the landing site, season and local time. This leads to developing a set of dispersed profiles covering the potential variability that can then be used in the Monte Carlo EDL modeling. These profiles need to capture the average behavior, the variability and the typical vertical structure expected.

[41] The MER atmosphere model was only developed for two cases: MER-A at L_s ~328, Local True Solar Time or LTST = 14:25 and MER-B at L_s ~347, LTST = 12:40. The MER-B landing changed to L_s = 339 and LTST ~13:10 after the case was developed, but this change will not have a significant impact on the atmospheric model. Both models are designed to implicitly cover an equatorial latitude band (5°N to 15°S for MER-A and 10°N to 10°S for MER-B) and allow for the selection of surface elevations between −4.181 km and −0.3 km. For numerical simplicity, the model uses the VL1 elevation (−3.681 km) as a reference

altitude. To easily mesh with the rest of the EDL modeling, the atmosphere profiles are given a 1/4 km altitude grid.

[42] In order to insure that each atmospheric profile is internally consistent, we used the following approach. First, a reasonable random temperature profile is created. Next, a surface pressure at the VL1 reference elevation is randomly selected. Combined with the hydrostatic approximation, this determines the pressure profile. Using the temperature and pressure profiles, the density profile is easily derived from the ideal gas law with the appropriate Martian atmospheric constants. This is done altitude by altitude based on the pressure and temperature profiles.

[43] Constructing the temperature profile starts off with a "baseline" profile for that lander/case built from temperature profiles retrieved by TES [*Smith et al.*, 2001b]. Nadir and limb profiles from the appropriate season (10 sol window) and equatorial region (all longitudes) are averaged separately and then a profile is fit between the two (Figure 9). This is extended isothermally to an altitude of 130 km for numerical purposes. Near the surface, the profile is smoothly joined to a "cold" surface temperature at the VL1 elevation.

[44] The TES observations do not provide temperature information below ~10 km. For Mars, the near surface atmospheric temperature is dominated by the surface albedo and thermal inertia (for a given opacity, LTST and season), regardless of the elevation. The results of a 1-D diurnal model by Jim Murphy [*Pollack et al.*, 1990; *Haberle et al.*, 1999; *Martin et al.*, 2003] were used to select an expected surface atmospheric temperature (representing an altitude of about 20 m above the surface). This is then used as the mean of a Gaussian distribution for surface temperature (using a 5 K standard deviation). The atmosphere is assumed to cool adiabatically until it reaches the "baseline."

[45] In order to represent weather and climate phenomena (and especially waves), it is necessary to add a vertical perturbation to the temperature profile. We used the Ames MGCM (Mars Global Circulation Model) [*Pollack et al.*, 1990; *Joshi et al.*, 2000] to estimate the expected temperature variability. This allowed us to better examine the local time of day effects as well as effects above ~40 km. By inspection, it was found that the variability was well represented by the following equation:

$$\Delta T(z) = f(z)\left[A_0 + \sum_{n=1}^{10} A_n \cos\left(\frac{nz\mathrm{p}}{52} + \Phi_n\right)\right],$$

where $\Delta T(z)$ is the perturbation at altitude z relative to the reference surface, $f(z)$ is an altitude-dependent scaling factor, A_0 is a constant temperature offset, the sum is over $n = 1$ to 10 (representing the first 10 Fourier frequencies), A_n, is the amplitude for the frequency n, and Φ_n, is the phase shift for that frequency. The constant 52 km is half the wavelength of the first frequency used in the process. $f(z)$ was chosen to be quadratic based on Ames MGCM (with a minimum at about 15 km above the surface). The coefficients are chosen empirically for each lander, with $f(z) \sim 1.5 - 0.1z + 0.003z^2$. An additional 2 K of variability was added to reflect phenomena that are not captured by the MGCM. This is primarily important below 20 km and is based on the Pathfinder ASI/MET observations [*Schofield et al.*, 1997].

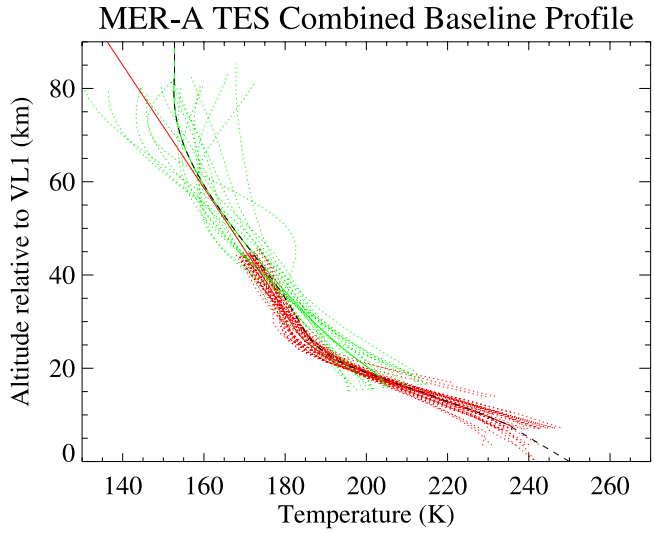

Figure 9. MGS-TES temperature profiles and the extracted "baseline" profile. The vertical axis is the altitude relative to the VL1 reference elevation. All of the profiles have been interpolated to this altitude scale for intercomparisons. The dotted red profiles are the TES temperature retrievals from the nadir observations. Each profile is the mean of many profiles in a 10° latitude bin. Each dotted green profile is an individual TES limb profile. The solid curves are the averages of the two sets, and the dashed black line is the selected "baseline" profile for the MER-A lander.

[46] The phases (Φ_n) are all a random value between 0 and 2π. The amplitudes (A_0 through A_{10}) are determined for a profile in the following manner:

$$C_n = 2 \times 10^{(-\mathrm{K1}n - \mathrm{K0})},$$

$$A_0 = C_0 R_n,$$

$$A_n = C_n + 0.5 C_n R_n, n \neq 0$$

where R_n is a random Gaussian (mean 0, standard deviation of 1). The functional form of C_n and the selected K0 and K1 constants are based on a Fourier analysis and least squares fit to the mean spectrum of the MGCM temperature profiles and yield K0 ~ 0.5 and K1 ~ 0.05, with slightly different values for MER-A and MER-B.

[47] It is important to note that while the vertical temperature structure in the MGCM results is based on physical processes, the model for EDL simulations does not contain the actual physics, only a parameterization of the physics based results. On the other hand, as shown by Figure 10, the resulting profiles appear reasonable based on our physical understanding of the Martian atmosphere as well as comparisons to available observations. They also cover the expected climatological range, and can be rapidly generated.

[48] The second component of the model is to determine a pressure on the reference surface. This was based on the VL1 pressure record at the MER landing season [*Barnes*, 1981; *Zurek et al.*, 1992]. Unfortunately, the Viking lander

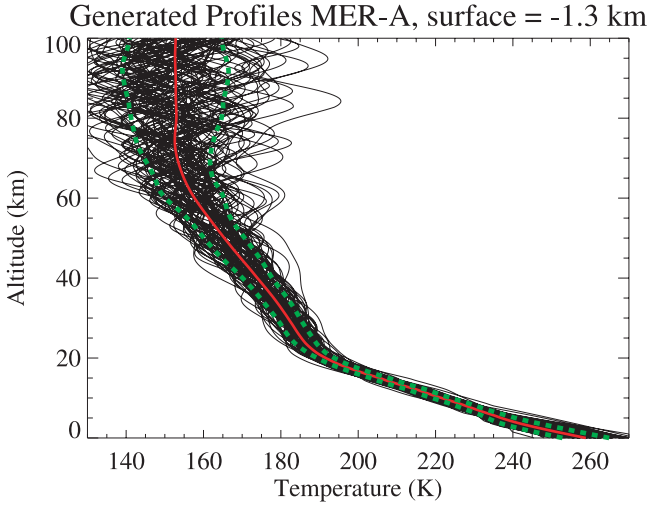

Figure 10. A family of 100 model temperature profiles produced from the complete model for the MER-A case with a surface elevation of −1.3 km. The solid red curve is the mean of the family (useful as a nominal case), and the dashed green lines show the one standard deviation in temperature at each altitude. Note that these are not expected profiles (instead, each individual profile will vary with altitude).

pressure data were coarsely digitized due to the limited precision of the lander electronics (despite the high precision of the actual instrument), masking the diurnal cycle. The VL1 observations during the ∼60 sols of the pressure minimum (where the mean is constant) were averaged on an hourly basis. This produces the diurnal pressure cycle for the season of interest. The cycle is very similar to the one seen at Pathfinder (where it is clearly resolved in the observations [*Schofield et al.*, 1997; *Haberle et al.*, 1999], despite it being at the opposite season.

[49] The mean reference surface pressure for MER-A is ∼8 mbar and for MER-B, ∼8.1 mbar. The difference is due entirely to the diurnal cycle. After accounting for the diurnal component, surface pressures at elevations of 0 km and −1.6 km are comparable to the ones estimated by *Smith and Zuber* [1998] from preliminary MOLA data and Ames MGCM results. The mean is perturbed for each profile with a Gaussian random variable, using a standard deviation of ∼0.37 mbar. The variability is chosen to give about a 5% variation in surface density for a −1.3 km case. The MGCM results and the Viking lander observations imply a variability closer to 0.2 mbar, but that is probably an underestimate for the zonal band and elevation range the model covers. It is also not clear that either the model or observations captures the full variability of Martian weather at this season.

[50] Once the temperature profile and surface pressure have been determined, the corresponding consistent pressure profile is then calculated using the hydrostatic approximation:

$$p(z_i) = p(z_{i-1}) \exp\left(\frac{-2(z_i - z_{i-1})}{H(z_i) + H(z_{i-1})}\right),$$

where $p(z_i)$ is the pressure at layer z_i and $H(z_i)$ is the scale height at the altitude of layer z_i. The starting altitude is the VL1 reference altitude, using the surface temperature until the actual surface is reached. $H(z)$ is calculated using

$$H(z) = \frac{RT(z)}{mg(z)},$$

where R is the gas constant (8.3143 J/K/mol), m is the mean Martian atmospheric molecular weight (43.49 g/mol), and $g(z)$ is the gravitational acceleration (m/s^2) at an altitude of z (including the point source, J2 correction and corriolis correction). Note that while the units of H are odd, they cancel correctly in the previous equation when z is in kilometers.

7.2. Wind Modeling

[51] The Pathfinder mission landed in the early morning hours during northern midsummer on the margins of the Chryse basin, a time and place where the Martian atmosphere was relatively calm. By contrast, the MER rovers will be landing just after midday, when the insolation is at the peak and the atmosphere the most dynamic. Furthermore, the MER landing system has been modified from the Pathfinder system and is quite sensitive to winds, wind shear (or gusts) and turbulence during the landing. Except at the two Viking Lander sites and for a short period at the Mars Pathfinder site, there are few direct wind measurements from Mars itself. (Owing to payload mass and schedule constraints, neither MER carries a wind sensor and so will not add to this data set.) In the absence of representative wind data, numerical wind models, adapted to Mars from their terrestrial counterparts, are used to provide estimates of the winds that could occur at selected landing sites. Previously (e.g., Viking and Mars Polar Lander), GCMs [*Pollack et al.*, 1990; *Joshi et al.*, 2000; *Richardson and Wilson*, 2002] were used to estimate the meteorological environments for spacecraft landing on Mars [e.g., *Pollack et al.*, 1976]. These GCMs have global domains, but relatively coarse spatial resolution (many tens to a few hundred km).

[52] Mesoscale Models (MMs) (MRAMS-Mars Regional Atmospheric Modeling System [*Rafkin and Michaels*, 2003]; Mars MM5 [*Toigo and Richardson*, 2003]) have much higher spatial resolution (∼1 km horizontal grid spacing and vertical spacing that varies from ∼10 m near the surface to ∼300 m on average at higher altitudes). Current computational capabilities restrict their horizontal domains to regions, whose time-dependent lateral boundary conditions are specified. Often, the MMs use nested grids in which an outer grid is regional with resolutions matching the GCMs but then zoom in to much higher resolution on a localized inner grid. Similar models have been used for weather forecasting on Earth for at least a decade but are new to Mars. Because the lack of "ground truth" makes it difficult to evaluate the numerical accuracy of the results, the analysis of the simulations reported herein focus on intercomparisons of the landing sites.

[53] These models were analyzed in two ways to compare the winds at the various landing sites [*Kass et al.*, 2003]. The first approach was a statistical analysis. This covered both the effective (or mean) horizontal wind as it affects the lander as well as the shear and turbulence. An average over the possible landing times and over the landing ellipse was performed. Given the smooth, flat nature of the landing sites, they did not show any geographic dependency within the

Table 5. Summary of MER Landing Site Criteria After Third Landing Site Workshop[a]

Major Questions/Criteria	Landing Sites[b]					
	Meridiani	Gusev	Isidis	Melas	Eos	Athabasca
Science Criteria[c]						
Evidence for water activity	O	O	O	O	O	O
Climate/geologic history addressable	O	O	O	O	O	...
May preserve (pre) biotic materials	O	O	...	...	...	...
Enables hypothesis testing	O	O	O	...	...	O
Accessible diversity within the site	O	...	O	...	...	O
Differs from other MER sites	O	O	O	O	O	O
Differs from VL and MPF sites	O	O	O	O	O	O
Has materials for Athena analyses	O	O	O	O	O	O
Acceptable rock abundance	...	...	O	...	O	O
Good site trafficability	O	O	...	...	...	X
Degree of dust obscuration	O	...	...	O	O	...
Expected mission lifetime	...	...	O	O	O	...
Relief at scale of Rover traverse	...	...	...	O	...	O
Has potential Earth analogs	O	O	O	O	O	O
Safety Criteria						
1 km slope <2°	O	O	O	X	X	O
100 m slope <5°	O	O	O	X	...	O
10 m slope <15°	O	...	...	X	...	O
Any local high relief (craters)?	O	...	...	X	...	...
Rock abundance/trafficability?	O	O	...	...	X	X
No potentially hazardous rocks	O	O	...	...	X	...
Horizontal winds (shear/turbulence)	O	...	...	...	...	...
Horizontal winds (sustained mean)	O	...	...	X	X	...
Acceptable vertical winds	...	O	...	...	...	...
Expected temperature at site	...	...	O	...	O	...
Local dust environment	O	...	...	O	O	...
Surface is load bearing	O	O	O	O	O	O
Elevation less than −1.3 km (MOLA defined)	O	O	O	O	O	O
Radar reflectivity >0.03	O	O	O	O	O	O
Public Engagement						
Site aesthetics	...	...	O	O	O	O
Site differs from VL or MPF sites	O	O	...	O	O	O
Potential habitability for life	O	O	...	...	...	...
Explainable to public	O	O	O	O	O	O

[a]Does not include criteria such as latitude, site separation, etc., used to distinguish sites prior to 3rd Workshop.

[b]O, no obvious concerns with respect to parameter; . . ., potential concerns with respect to parameter; X, recognized concerns with respect to parameter.

[c]Top three science criteria are considered to be the highest priority for all sites.

landing error ellipses, although there were both temporal and spatially random ''chaotic'' variability at all the sites. Significant differences between sites were largely due to effects of the complex regional topography (e.g., crater versus canyon). This analysis allowed for the sites to be easily compared and gave a preliminary look at site safety. As part of a more detailed Monte Carlo engineering analysis, a number of wind profiles from each site were randomly selected and augmented by adding in the high-frequency turbulence not directly represented by the mesoscale models.

8. Final Landing Sites

8.1. Third Landing Site Workshop

[54] The Third open Landing Site Workshop for the Mars Exploration Rovers was held in Pasadena, CA, in March of 2002 and dealt exclusively with discussion of the Meridiani Planum (Figure 3), Gusev crater (Figure 4), Isidis Planitia (Figure 6), Melas Chasma (Figure 5), Eos Chasma (Figure 7), and Athabasca Valles (Figure 8) sites. Focus was on detailed presentation of engineering concerns and constraints and discussion of scientific hypotheses relevant to the science objectives of the mission that could be tested using the Athena science payload on board the rovers [*Golombek et al.*, 2003a]. Table 5 summarizes the outcome of the meeting, which was generated from community discussion and consensus on the last day of the workshop and includes consideration of the probable ''public engagement potential'' of the sites.

[55] With respect to science, emphasis was placed on the relative merits of the sites for preserving evidence for past water activity, the likelihood of encountering an addressable geologic and climatic history, and the possibility for preservation of either biotic or prebiotic materials (Table 5). On the basis of these criteria, the Meridiani and Gusev sites were deemed the highest priority because of the possibility of constraining the origin of the coarse-grained hematite and associated deposits and for accessing paleo-lacustrine materials, respectively [e.g., *Arvidson et al.*, 2003; *Cabrol et al.*, 2003; *Greeley et al.*, 2003]. The Isidis and Melas sites were deemed slightly lower in priority overall primarily because of concerns related to the preservation potential of organics and possible issues regarding dust, rock abundance, and/or rover trafficability [e.g., *Weitz et al.*, 2003; *Crumpler and Tanaka*, 2003]. Overall science potential was deemed lowest at Eos and Athabasca Valles due to a variety of factors

Figure 11. Topographic map of 15°N–10°S showing areas evaluated for low-wind ellipses. Areas in deep blue are below −1.5 km elevation, and areas in green and orange are above 0 km elevation. Areas in light blue are above −1.5 km and below 0 km in elevation. Four main areas in light blue are eastern Meridiani (EM), southeast of Isidis (SEI), south of VL1 (SVL1), and Amazonis Planitia, which is too dusty (TD).

(Table 5). Trafficability at Athabasca was as a major source of concern as limited mobility could preclude or hinder attaining mission science objectives [*McEwen et al.*, 2001; *Burr et al.*, 2002a, 2002b; Haldemann et al., submitted manuscript, 2003].

[56] Discussion of engineering, or safety criteria (Table 5) produced a similar consensus on the relative merits and/or concerns of the landing sites. The Meridiani site clearly possesses the fewest potential risks to landing and mobility, whereas Gusev and Isidis are slightly riskier as a result of concerns related to the potential for relief and local slopes, dust, and winds (especially the horizontal component and possible associated shear, see *Kass et al.* [2003]). Hazards related to high horizontal winds and slopes at all length scales are even more apparent at the Melas and Eos canyon sites, with additional potential concerns related to high rock abundance. At Athabasca, concerns related mostly to radar-implied decimeter-scale roughness [*McEwen et al.*, 2001; Haldemann et al., submitted manuscript, 2003] that could significantly impact the ability to land safely and/or navigate on the surface. The expected low nighttime temperatures, local dust environment, winds, and rock abundance comprise additional potential issues at Athabasca.

[57] The science and safety criteria discussed above provided a template for more general decisions regarding the status of the individual sites emerging from the third workshop. The public engagement potential was deemed acceptable for all of the sites and was not used as a major discriminator. Broad concurrence was reached regarding the status of the Meridiani and Gusev sites as the highest priority from a science perspective, with Gusev carrying some uncertainty regarding potential wind shear (associated with the potential presence of a low-latitude jet crossing relief forming the bounding crater rim, see section 10 and *Kass et al.* [2003]) and accessibility of desired materials. Concerns related to the geologic provenance of materials at the Isidis site and potential occurrence of significant slope winds resulted in a slightly lower ranking, whereas concerns related to high winds, slopes, and rock abundance at Melas and Eos resulted in their being removed from consideration as potential sites. Finally, issues related to occurrence of significant decimeter-scale surface roughness at the Athabasca site coupled with somewhat lower perceived science potential led to the demotion of this site to a backup and later removal from further consideration.

[58] All of the above events and decisions were unanimously supported by the Landing Site Steering Committee and received the concurrence of both the MER Project and Athena Science Team. The realization, however, that the list of viable landing sites had been narrowed to Meridiani, Gusev, and Isidis following the third workshop coupled with the recognition that winds were an important safety consideration led to identification of a fourth "wind safe" site located to the southwest of Elysium Mons in Utopia Planitia. A detailed discussion of the science and engineering potential and concerns related to these final four sites set the stage for discussions at the fourth open workshop.

8.2. Identification of a Low-Wind Site

[59] The search for a safe, low-wind site involved identifying atmospherically quiet regions in two global circulation models (GCM) for the season and time of arrival [*Joshi et al.*, 2000; *Richardson and Wilson*, 2002]. Both models were run in high-resolution modes (with ~2° grids). This was found to be marginal for resolving many intermediate sized topographic features (e.g., Gusev crater or Valles Marineris), but did resolve many larger features (e.g., Isidis basin or Elysium Mons). For each model, the winds were examined at altitudes of ~1 km, ~3 km and ~5 km. At each level, a 10-Sol mean and variance were calculated for a LTST window around the landing times. In addition the MRAMS medium resolution (~1° grid) results were also used, where available [*Rafkin and Michaels*, 2003].

[60] Because definition of low-wind regions were the prime consideration, latitudinal (15°S to 10°N) and elevation (less than −1.3 km) constraints were relaxed from those originally considered to include areas up to 15°N and areas up to 0 km elevation (Figure 11). Four potential areas were investigated: east of the existing Meridiani site, northern Isidis, southeast of Isidis, and Elysium Planitia. The regions south and east of VL1 were also considered briefly, but were rejected given that the GCMs indicate these areas to be potential pathways (i.e., "storm tracks") for weather systems generated at high northern latitudes during the season of MER arrival and moving down over the Acidalia-Chryse lowlands [*Hollingsworth et al.*, 1996; *Collins et al.*, 1996]. Such storms could also reach into the northern Isidis region via the Utopia-Elysium pathway. In contrast, the GCMs suggested that the other regions would have light winds, and this was supported for the Meridiani and Elysium sites by detailed mesoscale model runs [*Rafkin and Michaels*, 2003].

[61] A handful of prospective sites were identified in each area and evaluated on the basis of science potential and safety. The sites east of Meridiani are likely too cold (i.e., low thermal inertia) and too close to the existing site (thereby reducing mission data return due to competition for UHF downlink relay via orbiters) and the areas southeast of Isidis were deemed to have low science appeal. The sites with the highest science interest were in the highland/

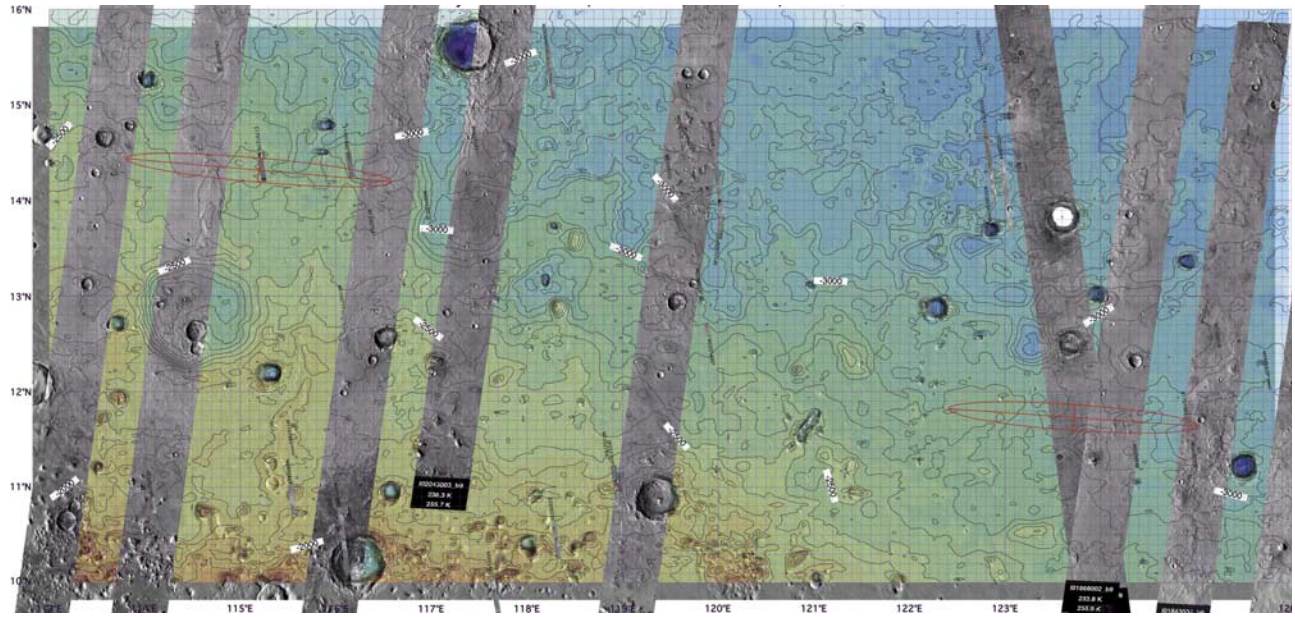

Figure 12. Elysium Planitia mosaic of two low-wind ellipses: EP80B2 (west) is 165 × 15 km, oriented at 95°, and EP78B2 (east) is 155 × 16 km, oriented at 94°, both for the opening of the launch window. The background is the Viking MDIM 2.0 mosaic, overlain by MOLA elevations in color (IAU 1991). Wide image strips are THEMIS thermal images at 100 m/pixel. Thin image strips are MOC high-resolution images through E17 of the MGS extended mission.

lowland boundary in Elysium Planitia (EP78B2 ellipse is 155 × 16 km oriented at an azimuth of 94° at 11.91°N, 236.10°W and EP80B2 ellipse is 165 × 15 km oriented at an azimuth of 95° at 14.50°N, 244.63°W in MDIM2 coordinates).

[62] Both Elysium ellipses (Figure 12) were targeted for the acquisition of new MOC and THEMIS images and safety and science potential were further evaluated. Rock abundance estimates from thermal differencing techniques show an average of 5% at EP78B2 and 9% at EP80B2, but other bulk thermophysical properties are similar [*Christensen*, 1986a, 1986b, 1982; *Mellon et al.*, 2000]. EP78B2 also appears smoother than EP80B2 in: MOLA estimates of 1.2 km scale adirectional and bidirectional slopes, 100 m scale MOLA pulse spread [*Smith et al.*, 2001a], extrapolations of the 100 m relief from Hurst exponent fits to the Allan variation at longer baselines [*Haldemann and Anderson*, 2002; *Anderson et al.*, 2003], and six MOC images and four THEMIS images per ellipse that had been acquired. High-resolution mesoscale wind models [*Rafkin and Michaels*, 2003; *Kass et al.*, 2003] for the two sites show slightly lower horizontal winds are expected at EP78B2 (similar to Meridiani) than EP80B2 (similar to Gusev), with similar estimates of wind shear and turbulence (both sites are comparable to Meridiani, but slightly more turbulent). EP78B2 is also slightly farther south so solar power should be greater. Science evaluation showed no strong preference of one site over the other and both sites appear to be on reworked highlands material. EP80B2 has greater relief, but less thermophysical variation in THEMIS thermal images with more dust and sand dunes in the lows. On the basis of these evaluations, EP78B2 was selected as one of the final four ellipses (Figure 13) and EP80B2 was eliminated at a meeting of the Mars Landing Site Steering Committee and the THEMIS team at Arizona State University on 26–27 August 2002.

9. Science Objectives of the Final Four Sites

[63] The focus of this section of the paper is to define science objectives associated with each of the candidate MER landing sites. Along with the objectives, working hypotheses are outlined that can be tested using the rovers and the Athena Payload (Tables 6–9). Of course, these hypotheses may be quickly updated and/or discarded once surface operations begin and rover-based data are received and analyzed. However, the development of hypotheses focused thinking about rover operations and how the measurements can be used to address science objectives associated with the Mars Exploration Program. In all cases the intent is to focus on evidence for the interaction of water and crustal material on Mars, following the integrating theme of planetary habitability.

9.1. Meridiani Planum

9.1.1. Geologic Setting

[64] The prime Meridiani Planum landing ellipses are TM10A2 and TM20B2 (Figure 3). Both are centered at 2.060°S, 354.008°E as defined in the planetocentric IAU 2000 coordinate frame. The first ellipse has margined 3σ dimensions of 119 × 17 km, with a long axis oriented at a heading (i.e., clockwise from north) of 84°. The second ellipse is 117 × 18 km, with a long axis orientation of 86°.

[65] The entire landing ellipse is located within a plains unit that is inferred from analyses of MGS TES spectra to contain approximately 15–20% by fractional area of the

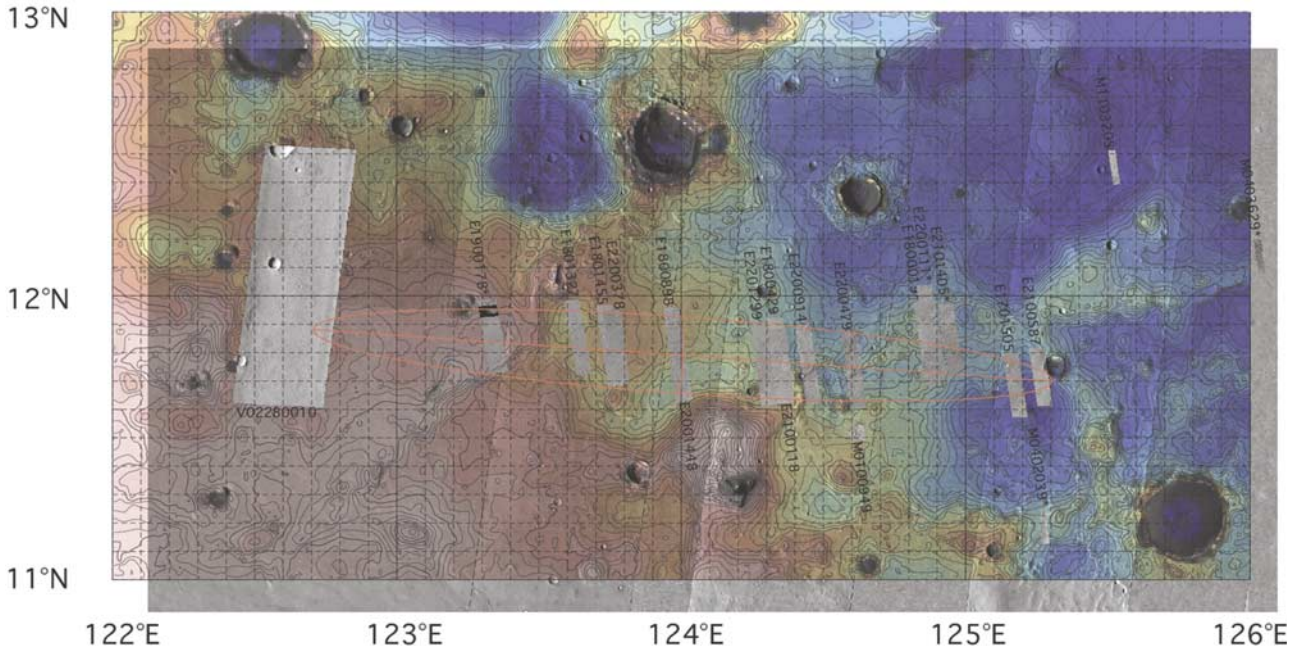

Figure 13. Elysium Planitia site mosaic. The background is the Viking MDIM 2.0 mosaic, overlain by MOLA elevations in color (IAU 1991). Thin image strips are MOC high-resolution images through E22 of the MGS extended mission. Wider image strips in the background are THEMIS thermal images at 100 m/pixel, with one THEMIS visible image in the foreground at 18 m/pixel (westernmost image). Ellipse EP78B2 for MER-B, shown in red for the opening of the launch window, is 155 × 16 km, oriented at 94°.

mineral hematite [*Christensen et al.*, 2000, 2001b; *Arvidson et al.*, 2003], either as discrete grains [*Christensen et al.*, 2001b], crystals embedded in glassy coatings [*Minitti et al.*, 2002], or as platy outcrops of the mineral [*Lane et al.*, 2002]. Mapping of the deposits shows that the hematite-bearing unit is the top stratum of a layered sequence of materials that overlies Noachian cratered terrain that has been dissected by valley networks [*Hynek and Phillips*, 2001; *Arvidson et al.*, 2003]. The valley network geometries indicate that flow was from the southeast to the northwest, consistent with the hypothesis that the valleys were carved after formation of the Tharsis plateau in late Noachian time [*Phillips et al.*, 2001], with associated flexure of the lithosphere beneath Meridiani Planum to the northwest [*Hynek et al.*, 2002]. Superposition relationships clearly show that the valleys are buried by the layered sequence.

[66] The layered sequence that is capped by the hematite-bearing stratum is approximately 600 m thick [*Hynek et al.*, 2002]. The hematite-bearing stratum has a low albedo relative to the units below it, and in some places the material may have been reworked by wind into dune-like patterns [*Arvidson et al.*, 2003]. The unit underlying the hematite-bearing stratum is exposed at many places within the landing ellipse. It is brighter and has a distinct etched appearance that suggests emplacement, erosion to some level, and then accumulation of the hematite-bearing stratum. This etched unit is extensively exposed beyond the hematite deposits and shows evidence of layering, dike-like features, and extensional fracture patterns.

9.1.2. Science Objectives and Testable Hypotheses

[67] A major science objective at the Meridiani Planum site would be to determine what process was primarily responsible for the formation of hematite (Table 6). There are several mechanisms by which hematite can form on Earth. Most of them, though not all, involve the action of liquid water. They include [*Christensen et al.*, 2000, 2001b; *Minitti et al.*, 2002; *Lane et al.*, 2002; *Noreen et al.*, 2001; *Arvidson et al.*, 2003]: (1) Direct precipitation from oxygenated Fe-rich water: this process implies the former existence of a substantial standing body of water. (2) Precipitation from Fe-rich hydrothermal fluids: this process involves water percolating through the ground at high temperatures. (3) Low-temperature dissolution and precipitation (i.e., leaching): this process also involves water percolating through the ground, but at low temperatures. (4) Surface weathering and development of coatings: this process involves gradual alteration in the presence of trace amounts of liquid water. (5) High-temperature oxidation of magnetite-rich lava: liquid water is not required at all for this process. (6) High-temperature oxidation of mafic volcanic glass and pyroxene: again, liquid water is not required for this process.

[68] These processes vary enormously in the extent to which liquid water was involved, and hence in their implications for habitability. The first two in particular could imply that a very habitable environment once existed at Meridiani Planum, the second and third would be ambiguous, and the fifth and sixth would provide little or no evidence for past habitability. So determining where the formation of the Meridiani Planum hematite lies in this spectrum of possibilities is of primary scientific importance.

[69] Some insight into the processes that most likely formed the hematite can be gained by considering geologic evidence inferred from orbital data. On the basis of such

Table 6. Meridiani Planum Site[a]

Topic	Hypotheses to be Evaluated	Key Observations	Key Measurement Requirements	Implications
Hematite occurrence	Is hematite present?	Unequivocal evidence for the presence of hematite inferred from Athena observations.	Pancam multispectral and Mini-TES mosaics, combined with detailed observations of key deposits to derive and analyze reflectance and emission spectra. Mössbauer spectra.	Validation of inferences from TES. Key ground truth for orbital observations in general since the site is thought to be unusual in mineralogical properties. Starting point for further data acquisition and hypothesis testing.
Hematite formation mechanisms	Did hematite form via aqueous processes and under what environmental conditions?	Hematite occurrence detailed and determined to be due to platy outcrops, discrete specular grains, or as hematite particles embedded in volcanic glass or as coatings on lithic fragments of basaltic or other composition. Minerals formed with hematite defined and inferences derived as to whether the ensemble formed via low-temperature (lacustrine) or high-temperature (hydrothermal) aqueous processes or via anhydrous oxidation (magmatic or ambient). Local geologic setting defined, including grain size distributions and other textural parameters, presence of layering and primary sedimentary features, including how hematite-bearing deposits fit in.	Ensemble of Athena observations.	The extent to which the deposits formed or were modified by aqueous processes. Environmental conditions associated with aqueous processes (lacustrine, hydrothermal) or perhaps anhydrous oxidation and associated environmental conditions. Implications for preservation of biosignatures through the development of coatings and other minerals that formed when hematite formed (e.g., silica deposits). Implications for geochemical cycles of biological relevance.
Geologic setting associated with hematite-bearing materials	Are hematite-bearing materials the top stratum of an extensive layered deposit draped over the ancient cratered terrain? Did the layered deposits form via lacustrine, volcaniclastic, or other means? Is basalt present as indicated by TES spectra?	Exploration and characterization of the dark materials evident at the site as plains and dark dunes. Exploration and characterization of the bright substrate evident at the site as subdued crater rims, bright plains, and bright dunes. Search for and characterize crater ejecta from underlying cratered terrain crust. Use all data to develop stratigraphic column and test the model with continued observations.	Mobility to get to various locations and the ensemble of Athena observations to characterize the sites and materials. OMEGA hyperspectral observations (0.36-5.2 μm) to provide mineralogical inferences at few hundred meter scale (acquisition while MER is operational).	Fundamental to understanding if the landing site is located on the upper strata of a vast lacustrine (or marine) deposit or if the site is on the top of a thick (hundreds of meters) volcaniclastic pile, with or without evidence for aqueous alteration processes. Implications for defining planetary habitability and the extent to which subsurface or surface habitats may have existed.

[a]Compiled by R. Arvidson and F. Seelos. Pros: specific, well-defined hypotheses can be tested that relate to the geologic history and set of processes that have operated, with a focus on the extent to which aqueous processes have been involved. The Athena payload and the MER mobility system are very well matched to testing the hypotheses. Spectral signatures relative to the rest of the planet and the low-albedo, dust-free nature of the site make it a good site for ground truth calibration of orbital data. Cons: there may not be evidence for aqueous processes and the site does not have a lot of topography for exciting vistas.

Table 7. Gusev Crater Site[a]

Topic	Hypotheses to be Evaluated	Key Observations	Key Measurement Requirements	Implications
Determine the origin of the primary materials filling Gusev crater (requires rocks, bedrock) and evaluate role of water in shaping crater filling deposits.	Wind-related deposits (global dust mantle versus local saltation versus volcanic, air fall).	Very fine grained, massive homogenous beds versus well-sorted, rounded grains <4 mm, with cross bedding. Locally derived compositions versus angular, massive, fine-grained, glass shards, silicate compositions (e.g., from Apollinaris Patera).	Imaging, RAT, spectroscopy (grain sizes below resolution; compositions not unique). Imaging spectroscopy (ambiguous; could be well-sorted sands of fluvial origin, but frosted likely aeolian).	
	Lacustrine (distal versus proximal materials).	Thin, fine-grained beds (rythmites), mud cracks, ripples; authigenic aqueous minerals (e.g., carbonates, evaporite salts).	Imaging, RAT, spectroscopy.	
	Fluvial.	Clastic materials, rounded, variably sized; graded or cross bedding, imbrication, variety of compositions (carbonates?).	Imaging, RAT, spectroscopy.	May constrain evolution of hydrologic cycle, implications for water inventory. Any outcome can help evaluate changing role of processes through time.
	Volcanic, effusive (i.e., lava flows).	Fine-grained crystalline rocks (phenocrysts, vesicles, corded textures or vesicle "trains").	Imaging, RAT, spectroscopy (flow features unlikely to be preserved/observed, and vesicle-like features can be nonvolcanic).	
	Impact (i.e., ejecta deposits).	Clastics, brecciated, poorly sorted, variable sized, Noachian impact melt matrix compositions, schlieren, shatter cones; hydrothermal alteration.	Imaging, RAT, spectroscopy.	Access to materials with good to fair preservation potential if lacustrine or fluvial.
	Mass wasting (e.g., debris flows, solifluction).	Clastics, poorly sorted, sizes and shapes dependent upon source material; little if any internal bedding structure; compositions correlative with likely source area.	Imaging, spectroscopy.	
Determine the origin of dark streaks (can have more than one origin).	Exposed bedrock (i.e., removal of bright dust from the surface).	Bedrock surface is observed and it is darker than the surrounding area.	Imaging, spectroscopy.	Verification of first two hypotheses indicative of high-energy wind regime, whereas third indicates low-energy regime).
	Lag deposit (e.g., stone pavement).	Clastic materials darker or larger than dust (may form pavement).	Wheel trenching; imaging of surface and subsurface materials.	May identify access to bedrock or in situ indurated sediments.
	Deposit of dark material.	Deposit of dark particles <4 μm; composition correlates with source.	Imaging, spectroscopy.	
Determine the origin of drift deposits.	Active wind-transported material (e.g., dunes or ripples).	Grains >60 μm and coarsening up indicate ripples; grains fining up indicate dune transport.	Imaging.	Determine whether drift represents wind-transported materials versus remnant of mantle (aeolian, volcanic, fluvial, colluvial, other).
	Remnant of former mantle (sand, dust, fluvial, or mass-wasting).	Internal structure (e.g., cross-beds of former dunes versus larger fluvial or mass-wasting clastics).	Imaging.	
Determine possible secondary/ alteration processes.	Weathering in a wet environment.	Clay minerals (pedogenic or as sulfates and salts if hydrothermal).	Spectroscopy.	Determine weathering environment of Mars near-surface over time.
	Alteration in a relative water-free environment.	Crystalline minerals or mineraloids associated with primary minerals.	Imaging, spectroscopy.	Constrain role of water in weathering. Constrain modern hydrologic cycle.
	Hydrothermal alteration.	Porous carbonate deposits, siliceous sinter.	Imaging, spectroscopy.	

[a]Compiled by R. Greeley. Pros: (1) Relatively clear geological models can be posed and tested, including that involving long-duration aqueous environments; (2) depending on the outcome of "hypothesis testing," the results are directly relevant to the primary MER project goals; (3) results (e.g., a channel intersecting a flat-floored, large crater) can be applied to other areas and carry significant implications for the general geological evolution of Mars; (4) secondary objectives (origin of dark streaks, drifts) can also give insight to these features seen elsewhere on Mars. Cons: (1) Many of the hypotheses do not have definitive tests using the Athena payload; (2) most of the "primary geology" (modes of origin for the floor materials) are dependent on having access to the relevant materials; processes, such as solifluction, might have emplaced thick (m??) materials not related to the primary floor-filling; we will be dependent on small impact craters to have excavated the relevant materials and on our being able to differentiate among the potential sources of the ejecta materials; (3) Gusev is a geologically complex area with an interesting history that can be difficult to deconvolve.

Table 8. Isidis Planitia Site[a]

Topic	Evaluated Hypotheses	Key Observations	Measurement Requirements	Implications
Early Mars was wetter than today.	(1) Ellipse in Isidis Basin lies within an ancient alluvial fan depositional environment.	Detailed evaluations of rock shapes and surface morphology, e.g., rock shapes (roundness).	PANCAM	Noachian Rocks from Isidis rim present within landing ellipses.
		Juxtaposition of landforms (bar and swale).	PANCAM, THEMIS, MOC	Transport from Isidis rim into basin involved streams and alluvial fans.
		Presence of weathering/alteration products (hydration minerals).	MB, Mini-TES and RAT	Mars had an active hydrologic system involving overland flow and active drainage networks.
		Fragment composition/petrology, textures (crystalline or clastic, veins).	APXS, MB, Mini-TES, MI before and after RAT	Place limits on climate evolution.
	(2) Isidis Basin was once the site of a standing body of water (''lake'').	Landforms (benches or berms, cuspate forms).	PANCAM, THEMIS, MOC	Shoreline features are present and indicate that either near shore or pelagic deposits comprise near-surface materials and embay the highlands.
		Rock shape and structure (sorted, rounded, sediments).	PANCAM and MI	If near-shore, high-energy environment, lower preservation potential.
		Rock type/petrology (mature versus immature, major versus minor component composition, crystalline versus clastic).	MB, APXS, MI, Mini-TES before and after RAT	If pelagic, low-energy environment, higher preservation potential.
		Stratigraphy (any low-angle truncations, accretion or forset beds, orientation relative to basin margin, continuity).	PANCAM	Mars had an active hydrologic system involving overland flow and active drainage networks. Place limits on water budget, cycling, and climate
	(3) Isidis Basin is floored by basalt that embays the highlands.	Rock textures (grain sizes, glasses, phenocrysts).	PANCAM, MI, RAT (MI before and after RAT)	Materials erupted in Isidis Basin and flowed to edge of basin.
		Rock structures (vesicles, jointing, banding).	PANCAM, MI	Constrain timing and inventory of volcanics.
		Morphology (typical of flows, aa, pahoehoe, tumuli).	PANCAM, THEMIS, MOC	Does not resolve role played by water in evolution of site or early Mars conditions.
		Stratigraphy.	PANCAM, Mini-TES	
		Composition (major and minor minerals and elements).	RAT, MB, APXS, Mini-TES	

[a]Compiled by G. McGill. Scientific pros: (1) Water and habitability involved with hypotheses 1 and 2; (2) water, habitability, and preservation in Noachian tested by hypothesis 1; (3) abundant rocks, which may be rounded and thus less dangerous to landing for hypotheses 1; (4) obtain compositions of highland rocks for hypothesis 1; (5) Good view! Scientific cons: (1) For hypothesis 3 the site does not address mission goals; (2) habitability and preservation difficult in an alluvial fan environment (but water alteration in veins good for habitability and preservation).

Table 9. Elysium Planitia "Wind Safe" Site[a]

Topic	Testable Hypothesis	Key Observation	Measurement Requirement	Implications
Can geologic setting be deconvolved so as to identify where highlands material might be sampled (either in situ or subsequent to transport)?	(1) Bench is a sequence of interbedded volcanic flows and pyroclastics overlying a Noachian basement.	Surface morphology: flows, outcrop textures, etc.	PANCAM	Not able to sample Noachian highlands materials or address most mission science objectives.
		Rock fabric (massive, vesicular, friable, etc.);	PANCAM, MI, RAT	
		Rock mineralogy.	Mini-TES, MB, APXS, RAT	
	(2) Bench is a marine terrace, comprised of layered marine sediments derived from highland front and underlying Noachian basement.	Presence of terraces, layered sediments.	PANCAM	Mars had a robust hydrologic system involving overland flow and oceans. Place limits on water budget, cycling, and climate. Possible access to materials with good preservation potential
		Sedimentary fabrics: sorting, cement, ripples, rounding, etc.	PANCAM	
		Rock mineralogy: evaporites, cement; rock mineralogy: fractionation, sorting.	PANCAM, MI, RAT, APXS, MB	
	(3) Bench consists of layered alluvium/colluvium derived from highland front and overlying Noachian basement.	Surface morphology: channels, debris flows, layering.	PANCAM	Might be able to sample reworked and transported Noachian highlands material (might be very difficult to identify), but little context. Difficult to address many mission objectives.
		Sedimentary fabrics and rock mineralogy as in 2 above.	PANCAM, MI, RAT, Mini-TES, APXS, MB	
	(4) Bench consists of layered alluvium/colluvium derived from highlands, overlying Noachian basement, and modified by mud volcanism and/or local groundwater seepages.	Same as above, except make observations on pancake-like structures and indistinct flows observed in orbiter images.	Same as above.	Might be able to sample reworked and transported Noachian highlands material (might be very difficult to identify), but little context. Access to widely scattered forms that may be mud volcanoes or springs might permit assessment of aspects of more modern hydrologic cycle, possible life.

[a]Compiled by M. Carr. Scientific pros: (1) May provide opportunity to examine a former marine environment; (2) local knobs appear to be highland basement and bench, most likely a degradation product of the highlands, so highland rocks may be abundant; (3) bench material may have been emplaced by aqueous processes (fluvial, solifluction, etc.) so may provide an opportunity to study such processes. Scientific cons: (1) No satisfactory geologic model for the origin of the bench on which the landing site is located; (2) great uncertainty about what will be found and whether the findings will relate to the main goals of the Mars exploration program, the role of water, and the prospects for life.

evidence, two models have been put forward. One suggests deposition in an aqueous environment like a lake [*Christensen et al.*, 2000, 2001b]. In this case the hematite would have formed either by direct precipitation from highly oxygenated iron-rich lake waters, or via alteration by percolating fluids after burial (processes 1 or 3 above). The second model suggests that the units are a volcaniclastic sequence deposited soon after tilting of the lithosphere and dissection of the Noachian cratered terrain [*Arvidson et al.*, 2003]. In this model, the hematite is emplaced either directly in volcanic materials (as discrete grains [*Noreen et al.*, 2001] or within glassy coatings), or via alteration after burial of the deposits (processes 2, 3, 4, 5, or 6 above).

[70] The two models continue to be debated. The lack of clear evidence for a topographic basin argues against the lacustrine model, and the lack of obvious source vents or volcanic landforms argues against the volcaniclastic model. With present orbital data, neither model can be shown to be correct. All of the possible hematite formation processes may be viable. Exploration of Meridiani Planum by one of the MER rovers would allow the hematite formation process to be investigated and perhaps determined conclusively (Table 6). The geologic models could be tested, and new ones could be developed if necessary.

[71] Pancam and the Microscopic Imager could be used to investigate the geologic setting and key geologic relationships, from regional to microscopic scales. What major stratigraphic units are present? Are primary sedimentary or volcanic features observed? What processes can be inferred from grain sizes and shapes?

[72] All of the compositional instruments could be used to determine what minerals are found in association with hematite. This investigation might be particularly effective, because the Athena Payload is very well suited to investigation of iron-bearing alteration phases. Are accessory minerals typical of those formed during volcanic activity, during hydrothermal alteration of mafic materials, or are they typical of low-temperature aqueous precipitates? To what extent and by what manner has water interacted with the rocks, and what are the products? The full suite of instruments, plus the Rock Abrasion Tool, could be used to investigate the physical distribution of hematite and associated minerals. Are they distributed through massive sedimentary or volcanic deposits, or are they present in veins or coatings?

9.2. Gusev Crater

9.2.1. Geologic Setting

[73] The prime Gusev landing ellipse is EP55A2 (Figure 4). It is centered at 14.640°S, 175.298°E as defined in the planetocentric IAU 2000 coordinate frame. It has margined 3σ dimensions of 96 × 19 km, with a long axis oriented at a heading of 76°. Gusev is a 160 km diameter, flat-floored crater of Noachian age, close to the highland-lowland boundary south of Elysium. Its southern rim is breached by Ma'adim Vallis, one of the largest branching valley networks on the planet. Ma'adim is over 800 km long, and in places over 25 km wide and over 2 km deep. It has only a few tributaries comparable in width to the main valley, but the valley walls and adjacent uplands are dissected by numerous small valleys. In the likely event that it was cut by running water, Gusev would have acted as a settling pool for sediment carried by the water that cut Ma'adim before it exited through a gap in the northern rim of the crater. A landing in Gusev therefore would provide an opportunity to study fluvial sediments derived from the southern highlands, and deposited in a lacustrine environment. Such sediments may provide important clues about environmental conditions on early Mars, which are, of course, of particular interest for the planet's potential habitability.

[74] *Cabrol et al.* [1996, 1998a, 1998b] and *Kuzmin et al.* [2000] concluded on the basis of crater counts that the cutting of Ma'adim took place over an extended period of time from the late Noachian into the Hesperian, a period of possibly as long as 2×10^9 years. *Irwin et al.* [2002], on the other hand, have suggested that Ma'adim was cut more rapidly near the end of the Noachian as large lakes at the valley's upstream end drained into it. These two scenarios differ in their timing and duration, but in both instances sustained fluvial erosion, rather than a catastrophic event, is implied.

[75] Like many large upland craters, Gusev has a shallow, flat floor with a surface that is significantly younger than the crater itself, estimated by *Cabrol et al.* [1998a, 1998b] to be Late Hesperian to Early Amazonian. Three main units form the floor of Gusev: cratered plains, etched plains, and possible delta deposits at the mouth of Ma'adim. Additional units have been identified in THEMIS thermal and visible images [*Milam et al.*, 2003]. The landing ellipse is located near the central, lowest part of the crater. It is almost entirely within the cratered plains, although it includes some small etched areas near the center of the ellipse. Also included are some low hills with etched surfaces that could be outliers of the higher-standing etched plains to the east or of the delta deposits to the south.

[76] The cratered plains themselves are featureless except for superimposed craters, wrinkle ridges that resemble Mare ridges on the Moon, and wind streaks and splotches. Their morphology reveals little about their origin. Lacustrine sediments may be at the surface, but these plains also resemble Hesperian ridged plains elsewhere on the planet, which are generally interpreted to be volcanic. Lacustrine sediments may therefore be covered with a veneer of younger volcanics and/or aeolian material and making them accessible only via impact ejecta. The eastern end of the ellipse straddles the western rim of the ~20 km diameter crater Thira, which stands tens of meters above the plains. North of the western end of the ellipse is a 6 km diameter crater, whose ejecta can be traced into the ellipse.

9.2.2. Science Objectives and Testable Hypotheses

[77] The primary scientific objectives at the Gusev site would be to determine the processes that filled the crater, and to study their implications for a possibly habitable past environment (Table 7). Given the length and depth of Ma'adim Valles and the shallow relatively flat floor of Gusev crater, the quantity of lacustrine sediments within Gusev is likely to be substantial. However, because the present surface might be volcanic or aeolian, access to subsurface materials is of concern. Craters that could excavate to 10–20 m depth are common throughout the ellipse, so ejecta from this range of depths are likely to be

accessible. Sampling to deeper levels becomes less likely: there are only five craters within the ellipse that would have excavated to ~200 m. Erosion around a crater near the center of the ellipse and hints of layering within the crater wall suggest that portions of the near surface are layered at the scale of tens of meters or less, so small crater ejecta could likely contain this material.

[78] Several processes could have contributed to the filling of Gusev, including lacustrine sedimentation and possible lava eruptions. Air fall deposits from Appolinaris Patera, which is located north of Gusev, could be present. Several large nearby craters could have contributed impact ejecta. If lakes were formerly present, they may have on occasion evaporated and left behind evaporite deposits. Much of the cratered uplands has undergone repeated burial and exhumation [*Malin and Edgett*, 2001], possibly as a result of aeolian processes, and Gusev has likely been similarly affected. Stratigraphic relations within the crater therefore may be complex, with water-lain sediments intercalated and intermixed with other materials. This may prove advantageous in that a wide variety of materials may be accessible using the rover's mobility, but it is also likely to complicate geologic interpretation.

[79] Assuming that water-lain sediments can be located, analysis using the Athena instruments has the potential to reveal much about the fluvial and lacustrine processes that were involved in their deposition and about the climatic conditions that prevailed at the time (Table 7). The scale of any layering and the degree of intercalation with other rock types as observed by Pancam would provide clues about duration and continuity of deposition. Lithological characteristics such as grain size, sorting, rounding, varves, and diagenetic structures observed by the Microscopic Imager, perhaps with help from the RAT, would reveal important clues about the fluvial regimes such as whether deposition was the result of a succession of short energetic episodes or continuous, quiet, lower-energy activity. The chemical and mineralogical composition of the sediments as revealed by the APXS, Mini-TES and Mössbauer would provide strong indications about the environments under which erosion and deposition occurred, whether there were weathering episodes between depositional episodes, whether the postulated lake ever evaporated, and whether there was chemical alteration after deposition, such as might have occurred as a result of hydrothermal activity.

[80] A landing at Gusev could also allow study of the nature of the cratered uplands. Any sediment present will have been derived from the uplands, and some fraction of the impact ejecta at the surface must be from the surrounding uplands as well. Questions that can be addressed include: What is the chemical composition of the cratered uplands? Are the cratered uplands simply brecciated igneous rocks or is there a significant sedimentary component? What weathering processes have the cratered uplands materials experienced, and what do the weathering products imply about climatic conditions in the Noachian?

9.3. Isidis Planitia

9.3.1. Geologic Setting

[81] The prime Isidis Planitia landing ellipses are IP84A2 and IP96B2 (Figure 6). Both are centered at 4.220°N, 88.148°E as defined in the planetocentric IAU 2000 coordinate frame. The first ellipse has margined 3σ dimensions of 132 × 16 km, with a long axis oriented at a heading of 88°. The second ellipse is 140 × 16 km, with a long axis orientation of 91°.

[82] The landing site is immediately north of Libya Montes, in the plains that fill the Isidis basin. The ellipse lies mostly in intermontane plains thought to consist of coalescing alluvial fans formed as sediment debouched from the highlands onto the plains [*Crumpler*, 1999]. These materials transition northward to knobby plains that comprise the bulk of materials within Isidis Planitia, in which the Beagle 2 landing ellipse resides [*Bridges et al.*, 2003]. Small cones, commonly arranged in chains, cut across portions of these central Isidis plains.

[83] The region in which the ellipse is located is high in both thermal inertia and albedo relative to average Martian values. It is also spectrally reddish relative to average Mars [*Golombek et al.*, 1997a]. A plausible interpretation is that cemented soils (forming duricrust) are common in this region, although the reddish color is also indicative of dust [*Ruff and Christensen*, 2002].

9.3.2. Science Objectives and Testable Hypotheses

[84] The main scientific objective at the Isidis Planitia site would be to investigate the possibility that the plains consist of the distal ends of a bajada or coalescing alluvial fan complex (Table 8). If this interpretation is correct, then study of this region would be important for two reasons. First, the materials comprising the fans would have washed down from ancient cratered terrain to the south, and would allow study of the oldest mapped Noachian crustal materials [*Greeley and Guest*, 1987]. Second, transport and possible alteration of these materials by liquid water could lead to preserved evidence of the environmental conditions at the time the transport and/or alteration took place.

[85] An important test of the plains materials' origin would be to use Pancam images to search for evidence of relict landforms typically associated with alluvial fans, including washboard structures and abandoned sections that have become terraces. It would also be important to use the Microscopic Imager to search for evidence for the poorly sorted sedimentary deposits typical of fan depositional environments, with a mix of local and highlands rocks. Alternative hypotheses, particularly toward the northern part of the ellipse, is that the deposits were emplaced by local volcanic activity or an ancient lake or ocean. Again, both Pancam and MI images would be important in searching for the morphologic clues that would support this hypothesis. Mixtures of fluvial, lacustrine and volcanic processes are also possible.

[86] A second objective would be to evaluate the extent to which the deposits have been altered by interactions with aqueous fluids. This could occur by shallow groundwater emanating from fan surfaces, or via hydrothermal activity. Either process could be expected to produce distinctive assemblages of alteration minerals that could be detected using the Athena Payload. In particular, the rover and payload could be used to investigate why the site has high thermal inertia and yet is also bright and red. The presence of duricrust is one possibility. Another is that high-velocity slope winds have removed dust and left behind intrinsically red rocks. What types of rocks are present, and to what extent does the color indicate the extent of oxidation,

particularly in a hydrous environment? All of the payload's compositional capabilities (Pancam multispectral imaging, Mini-TES, Mössbauer, APXS) would be useful in this regard. In addition, the rover wheels could be used to excavate shallow trenches within and through duricrust, allowing study of soil composition as a function of depth.

9.4. Elysium

9.4.1. Geologic Setting

[87] The prime Elysium landing ellipse is EP78B2 (Figure 13). It is centered at 11.73°N, 123.958°E as defined in the IAU 2000 coordinate frame. It has margined 3σ dimensions of 155 × 16 km, with a long axis oriented at a heading of 94°.

[88] In contrast to the other three sites just described, the Elysium site was chosen primarily because of its inferred low winds in mesoscale atmospheric circulation models, rather than for its geologic properties. As a result, the scientific rationale for the site is less compelling than for the other sites.

[89] The site is located on a low, wide bench south of Elysium Planitia, between heavily cratered terrain to the south and the gently sloping plains of Elysium Planitia to the north. Most of the bench has a gently rolling topography caused by low rounded hills, muted ridges, and gentle, quasi-circular depressions. To the north, the bench merges with the plains of Elysium Planitia, along a complicated transitional boundary. Farther north, the bench complexly interfingers with the lower-lying plains, and islands of bench-like materials, surrounded by plains are isolated from the main part of the bench. Occasional sharply defined hills, a few kilometers across, occur within the bench and these become more common to the south as the gradational boundary with the heavily cratered upland is approached. The site itself is roughly in the middle of the bench. *Greeley and Guest* [1987] mapped the bench as Hesperian ridged plains, interpreted as volcanic. *Parker et al.* [1989, 1993] and *Clifford and Parker* [2001] mapped the inner and outer boundaries of the bench as shorelines. *Jons* [1985, 1986] ascribed many of the features of the highland-lowland boundary in general to large-scale mass wasting.

9.4.2. Science Objectives and Testable Hypotheses

[90] The main science issues at the Elysium site concern the origin of the bench material, and what other materials are likely to be available for sampling (Table 9). Several formation mechanisms for the bench are possible.

[91] 1. The bench is composed of Hesperian volcanic flows and pyroclastic deposits. The gently rolling topography, vague circular structures, subdued ridges, and lack of flow features all argue against a primary surface of volcanic flows for most of the bench. However, the bench might be formed of easily erodible, layered ash deposits that could be deflated by the wind. A counterargument is that it lacks obvious wind erosion features, and there is little supporting evidence for a volcanic source.

[92] 2. The bench was formerly part of the floor of a northern ocean. *Head et al.* [1999] have argued that the southern boundary of the bench is unlikely to be a shoreline because of the large range in elevations along it. The ragged, etched-appearing nature of the northern boundary of the bench also argues against a marine origin for that escarpment. Regardless of the origin of the bench, marine processes could still have played a role at the site if the northern plains were filled with water to the appropriate level.

[93] 3. The near-surface materials of the bench were shed by mass wasting from local highs and from the main highland front to the south [*Jons*, 1985, 1986; *Tanaka et al.*, 2002, 2003]. The rolling topography of the bench surface and the vague circular structures suggest that a near-surface deposit is draped over a cratered surface at shallow depth. The main argument against such an origin is the low regional slope (typically about 0.002°). It is doubtful whether material could move several hundred km across such low slopes by any mechanism other than water transport.

[94] 4. The near-surface materials were eroded by fluvial activity from the highland front and deposited north of the front to form the bench [*Tanaka et al.*, 2002, 2003]. In support of this hypothesis are the numerous valleys in the highlands just to the south of the highland front. Arguing against the hypothesis is the complete lack of evidence for fluvial activity on the bench itself.

[95] 5. The near-surface materials were deposited over a preexisting surface by aeolian activity or volcanic air fall of volcanic ash. This is certainly possible, but there is little or no evidence of wind deposition other than dunes scattered over the surface of the deposit.

[96] All of these hypotheses are in principle testable using elements of the Athena payload. The most important tools will be Pancam for establishing regional and local geologic relationships, and the Microscopic Imager for studying fine-scale textural details that may yield clues to the formation mechanisms of the materials encountered.

[97] At least two materials may be present within the landing ellipse. One is the bench-forming material itself. In addition, craters are common in and around the ellipse, and they are likely to have penetrated the bench-forming deposits and brought to the surface materials from the older terrain at depth. This site may therefore offer an opportunity to study unaltered highland rocks and ancient crustal formation processes. All of the elements of the Athena payload, including particularly the compositional spectrometers (Mini-TES, APXS, Mössbauer) would be useful for this purpose.

10. Atmospheric Properties of the Final Sites

[98] As described in section 7, the atmospheric profile model is generalized to cover all the possible landing sites for the MER mission. Thus the only variation in atmosphere between the landing sites is the landing elevation and the obvious (but important) associated surface pressure and thus column density changes. The winds from the mesoscale models vary significantly from site to site. This results in the potential of winds playing a significant role in discriminating between the various possible landing sites. The details of the differences are listed in *Kass et al.* [2003], *Rafkin and Michaels* [2003] and *Toigo and Richardson* [2003].

[99] The Meridiani Planum site is a broad flat region with little regional or global circulation. This leads to a vigorous convective system developing to a depth of ~5 km. The sustained horizontal winds are modest with overall moderate, but vertically extensive wind shears. The deep convec-

tive system does develop strong vertical winds. Gusev crater's walls have a large impact on the circulation at the landing site. This is further enhanced by the preferential location of a low-level global jet over the crater. The net result is moderate horizontal winds and fairly significant shear (Table 10), although much of the high-frequency shear is confined to the shallow boundary layer. The Isidis landing site is dominated by a strong, persistent upslope flow driven by the basin wall. This also compresses the boundary layer, creating a very turbulent, but shallow region. The complex topographic structure does introduce a significant longer (vertical) wavelength shear component at the site. Finally, the Elysium site has the same modest winds as seen at Meridiani, although they appear to be organized by the upslope flow along the nearby north-south dichotomy boundary. The boundary layer is not as deep (perhaps due to the more organized regional wind field), leading to weaker vertical winds but somewhat more turbulence.

[100] It is interesting to compare the winds at the four selected landing sites to those at a potential site in Melas Chasma. There, the average sustained (or mean) winds were quite high (over three times as fast as what was modeled at the Meridiani landing site with peak values significantly higher still). While the average shear on the canyon floor was comparable to the inside of Gusev crater, locations and times of significantly higher shear occurred regularly. Overall, the mesoscale models predict that the Meridiani site and Elysium site (as intended) have modest wind conditions. Gusev crater and the Isidis basin have more dynamic winds and other candidates sites are potentially even worse (Table 10).

[101] Minimum nighttime temperatures at the landing sites set limits on power available for science activities, and mission lifetime. *Martin et al.* [2003] derive these temperatures at the end of the nominal 90 Sol primary mission from TES thermal inertia and albedo, estimated opacity, and predictions of 1-m air temperatures from a one-dimensional atmospheric model. Mapping these results onto the probability density distribution of the landing ellipses shows that of the primary sites, Meridiani is the coldest, with an 8% chance of encountering minimum nighttime temperatures below the −97°C value (defined by a line with thermal inertia of 243 at 0.30 and 177 at 0.10) considered a practical limit for operations. Elysium and Gusev are at 7% and 3%, respectively, whereas Isidis has no computed 1 m air temperatures below −97°C (defined at Gusev by a line with thermal inertia of 251 at 0.30 and 187 at 0.10). Preliminary high-resolution THEMIS observations of nighttime surface temperatures show similar results.

11. Surface Characteristics of the Final Sites

11.1. Thermal Inertia, Rock Abundance, and Albedo

[102] Bulk thermal inertias of all of the prospective landing sites fall within the extremes or are similar to those sampled at the Viking and Mars Pathfinder landing sites (Table 10). IRTM and TES thermal inertia for the landing sites are also consistent with each other and range from 230 at Meridiani to 450 J m^{-2} $s^{-0.5}$ K^{-1} or SI units at Isidis. Preliminary THEMIS derived thermal inertias are also generally consistent with TES results [*Fergason and Christensen*, 2003] and none of the final four sites show marked variability in thermal inertia within the ellipses. The TES thermal inertia of the VL1 site is ~320, the VL2 site ~240, and the Pathfinder site ~400 (Figure 14). Fine component thermal inertias at all of the prospective landing sites also fall within the extremes or are similar to those sampled at the Viking and Mars Pathfinder landing sites. The IRTM fine component thermal inertia of the prospective sites range from ~250 at Gusev to 385 at Isidis, compared to ~250 at the VL1 site, ~175 at the VL2 site (by inference from the bulk TES inertia and the rock abundance), and ~344 at the Pathfinder site. The Isidis site has slightly higher bulk and fine component thermal inertia than the Mars Pathfinder site, but this is likely due to a more cemented duricrust [*Jakosky and Mellon*, 2001; *Golombek et al.*, 2003b]. In all of these cases, the thermal inertias suggest the surfaces are dominated by duricrust (at the high end of the fine component range), to cemented soil-like materials or cohesionless sand or granules [*Jakosky and Christensen*, 1986; *Golombek et al.*, 1997a]. In any case, the surfaces should be competent, load bearing and pose no special risk to landing or roving. None of the surfaces are likely to have thick deposits of fine-grained, non-load-bearing dust.

[103] IRTM thermal differencing indicates rock abundances at the sites that are generally lower than VL1, VL2 or Pathfinder (16%, 17% and 18% respectively). Average rock abundance at Meridiani and Elysium are ~5% and below the global mode of ~8% [*Christensen*, 1986b]. Rock abundance at Gusev, on average, is higher at 7.5%. Rock abundance at the other sites ranges from 12 to 17% (Table 10). Model rock size-frequency estimates of the areas covered by potentially hazardous rocks >1 m diameter

Note to Table 10

[a]Latitude and longitude +W is planetographic MDIM 2.0 coordinates [*USGS*, 2001], positive west. Longitude +E is planetocentric MOLA IAU91 coordinates, positive east. MOLA elevations with respect to the MOLA geoid (see text) are measured from the center of mass (COM). 1.2 km bidirectional (bi-dir) and adirectional (a-dir) slopes are calculated as described in the text, respectively. Pulse width [G] is slope corrected data (slopecor) from *Garvin et al.* (1998) and *Smith et al.* [2001a]. Pulse width [N] is both not slope corrected and slope corrected (slopecor); data from *Neumann et al.* [2003]. Self affine 100 m Allan deviation and RMS slope are from *Anderson et al.* [2003] as described in the text; *n* is the number of data, which for these are the same as the 1.2 km bi-dir slopes. The MOC derived bidirectional RMS slope from *Kirk et al.* [2003] is derived from stereogrammetry (stereo) at 10 m DEM resolution and PC, at 3–6 m DEM resolution and corrected via Hurst exponent for 5 m baseline. Radar data are 3.5 cm X-band measures of RMS slope and reflectivity for Meridiani, Isidis, Athabasca, and MPF and estimates from nearby surfaces of the same geologic unit for the others as described in *Haldemann et al.* [2003] and *Anderson et al.* [2003]. The IRTM data set is from P. Christensen as described in the text. The TES data are from *Mellon et al.* [2000], *Jakosky and Mellon* [2001], and *Pelkey et al.* (2003). All thermal inertia values are in SI units or J m^{-2} $s^{-0.5}$ K^{-1}. The number of TES albedo points is the same as the number of TES thermal inertia (I). Percent (%) area covered by rocks >1 m diameter (0.5 m high) from model size-frequency distribution curves are pinned to total rock abundance as described by *Golombek and Rapp* [1997] and *Golombek et al.* [2003b]. Horizontal winds are as calculated from the MRAMS [*Rafkin et al.*, 2003] and the Mars MM5 mesoscale models [*Toigo and Richardson*, 2003], wind shear is as estimated by the models, and the wind turbulence is as estimated by the MRAMS model, all as summarized in *Kass et al.* [2003]. The latter two are scaled relative to the model of wind shear used by the MPF project.

Table 10. Landing Site Ellipse Data[a]

Site	Meridiani	Gusev	Elysium	Isidis	Melas	Eos	Athabasca	VL1	VL2	MPF
Latitude, deg	−2.07	−14.82	11.91	−4.31	−8.88	−13.34	8.92			
Longitude, deg + W	6.08	184.85	236.10	271.97	77.48	41.39	205.21			
Latitude, deg	−2.06	−14.64	11.73	4.22	−8.75	−13.2	8.83	22.27	47.67	19.09
Longitude, deg + E	353.77	175.06	123.72	87.91	282.36	318.46	154.67	311.81	134.04	326.51
MOLA elevation, km, center	−1.440	−1.920	−2.940	−3.740	−3.700	−3.850	−2.640	−3.6	−4.5	−3.7
Range	−1.37–1.58	−1.8–1.93	−2.68–3.20	−3.68–3.74	−2.35–4.13	−3.2–4.03	−2.51–2.66			
Geoid, km, COM	3395.526	3394.227	3395.239	3396.115	3395.758	3394.427	3395.096	3339.299	3386.349	3393.482
1.2 km bi-dir slope, deg, mean ± SD	0.15 ± 0.18	0.20 ± 0.44	0.48 ± 0.55	0.19 ± 0.24	1.22 ± 1.35	1.22 ± 1.87	0.20 ± 0.36	0.26 ± 0.96	0.29 ± 0.29	0.25 ± 0.66
RMS, deg	0.26	0.49	0.73	0.30	1.80	2.23	0.41			
n	680	679	934	782	698	686				
1.2 km a-dir. slope, deg, mean ± SD	0.24 ± 0.47	0.19 ± 0.29	0.41 ± 0.29	0.14 ± 0.10	1.10 ± 0.66	1.02 ± 1.08	0.20 ± 0.29	0.33 ± 0.95	0.28 ± 0.21	0.30 ± 0.51
RMS, deg	0.53	0.34	0.51	0.17	1.29	1.48	0.35			
n	208	277	361	315	307	262				
Pulse width, slopecor [G], m, mean ± SD	0.75 ± 0.24	1.42 ± 0.44	1.10 ± 0.4	1.10 ± 0.35	1.21 ± 0.74	1.06 ± 1.14	1.18 ± 0.35			
RMS, m	0.8	1.5	1.1	1.2	1.4	1.6	1.2			
n	1152	1340	1366	1140	1028	1026				
Pulse width [N], m, mean ± SD	0.8 ± 0.9	1.5 ± 1.3	1.9 ± 2.8	5.1 ± 1.8	3.1 ± 2.2	4.7 ± 6.2	1.9 ± 2.6	2.1 ± 3.7	1.1 ± 0.4	2.0 ± 3.6
n	531	101	478	8	554	422	387	3640	921	2742
Pulse width, slopecor [N], m, mean ± SD	0.8 ± 0.8	1.1 ± 1.0	1.5 ± 1.7	1.8 ± 2.8	3.4 ± 4.1	3.9 ± 6.8	1.6 ± 2.4	1.7 ± 2.9	1.1 ± 0.4	2.0 ± 4.1
n	544	296	5879	7078	18,206	16,518	1867	535	921	1755
Self affine 100 m Allan dev, m	3.4	5.8	4.0	2.6	9.9	11.5	4.3	1.8		5.0
RMS slope, deg	1.9	3.3	2.3	1.5	5.7	6.6	2.5	1.0		2.9
MOC RMS slope, deg, bi-dir, 3–10 m	1.3–2.5	2.3–12.6	1.9–3.5	2.4–5.8	9.9–13.0	5.8–10.5	0.9–4.0			3.2
a-dir, 3–10 m	1.8–3.8	4.1–16.1	2.7–5.1	3.1–8.8	12.7–15.5	7.0–13.6	1.5–5.3			4.5
bi-dir, 5 m	1.2–2.7	2.3–13.2	2.0–3.5	2.4–6.0	11.7–14.3	5.4–10.5	1.0–4.0			3.5
a-dir, 5 m	1.7–4.0	4.1–16.9	2.8–5.1	3.1–9.1	14.3–17.9	6.5–13.6	1.6–5.4			4.9
3.5 cm radar RMS slope, deg	1.4 ± 0.2	4.7 ± 1.6	3.0 ± 1.1	3.3 ± 0.5	4.3 ± 2.4	4.7 ± 1.6	2.3 ± 0.4	4.7 ± 1.8	2.0 ± 0.3	4.5 ± 1.8
3.5 cm radar reflectivity	0.05 ± 0.02	0.04 ± 0.02	0.05 ± 0.03	0.03 ± 0.01	0.02 ± 0.01	0.04 ± 0.02	0.03 ± 0.01	0.04 ± 0.03	0.06 ± 0.01	0.05 ± 0.01
IRTM I, SI, mean ± SD	319 ± 5	284 ± 0	320 ± 2	451 ± 32	302 ± 6	385 ± 0	333 ± 8	355	338 ± 14	434
Range	314–326	284–284	318–322	418–489	293–305	385–385	322–343	330–360	321–355	396–533
n	4	4	4	8	4	3	8		16	
TES I, SI, mean ± SD	232 ± 37	274 ± 35	264 ± 22	455 ± 41	310 ± 16	386 ± 57	313 ± 51	320 ± 15	242 ± 16	418 ± 36
Range	158–271	213–373	213–355	384–574	159–606	266–647	184–514		192–292	
n	8053	7195	9716	8127	7173	6904	9442	570	450	512
IRTM FC I, SI, mean ± SD	307 ± 9	248 ± 22	303 ± 13	384 ± 19	246 ± 13	305 ± 36	272 ± 30	284 ± 21	260 ± 12	338 ± 16
Range	297–318	230–276	292–322	347–405	230–259	280–347	238–326	260–326	238–280	317–363
n	4	4	4	8	4	3	8		16	
IRTM albedo, mean ± SD	0.138 ± −0.055	0.150 ± 0.069	0.261 ± 0.004	0.180 ± 0.056	0.148 ± 0.068	0.117 ± 0.047	0.209 ± 0.075	0.250	0.243 ± 0.060	0.215
Range	0.090–0.190	0.090–0.211	0.256–0.266	0.090–0.224	0.090–0.214	0.090–0.171	0.090–0.266	0.23–0.25		0.19–0.23
TES albedo, mean ± SD	0.171 ± 0.026	0.222 ± 0.023	0.229 ± 0.005	0.228 ± 0.003	0.148 ± 0.017	0.136 ± 0.011	0.245 ± 0.006	0.255 ± 0.006	0.304 ± 0.012	0.218 ± 0.01
Range	0.124–0.235	0.173–0.265	0.211–0.244	0.217–0.235	0.107–0.241	0.108–0.159	0.214–0.263			
Rock abun. %, mean ± SD	5 ± 3	7.5 ± 1	5 ± 3	14 ± 1	12 ± 1	17 ± 5	13 ± 5	16	17	18
Range	1–7	7–8 (bit of 3)	1–8 (bit of 11)	13–15	10–13	12–22	6–19	8–19		18–25
n	4	2	7	2	4	3	8			
% area >1 m diameter, mean	0.04	0.15	0.04	0.7	0.5	1.0	0.6	0.8	1	1
Range	0.001–0.15	0.15–0.2	0.001–0.2	0.6–0.8	0.34–0.6	0.5–1.8	0.005–1.1	0.15–1.1		1–2
Horiz. wind, m/s, MRAMS	4 ± 2	7 ± 2	4 ± 2	9 ± 1	14 ± 5					
MM5	4 ± 2	3 ± 1		11 ± 2	1 ± 1					
Shear MRAMS	0.4	0.9	0.3	0.7	0.8					
MM5	0.2	0.5		1.4	0.5					
Mean turbulance	0.7	1.8	1.5	2.0	1.6					

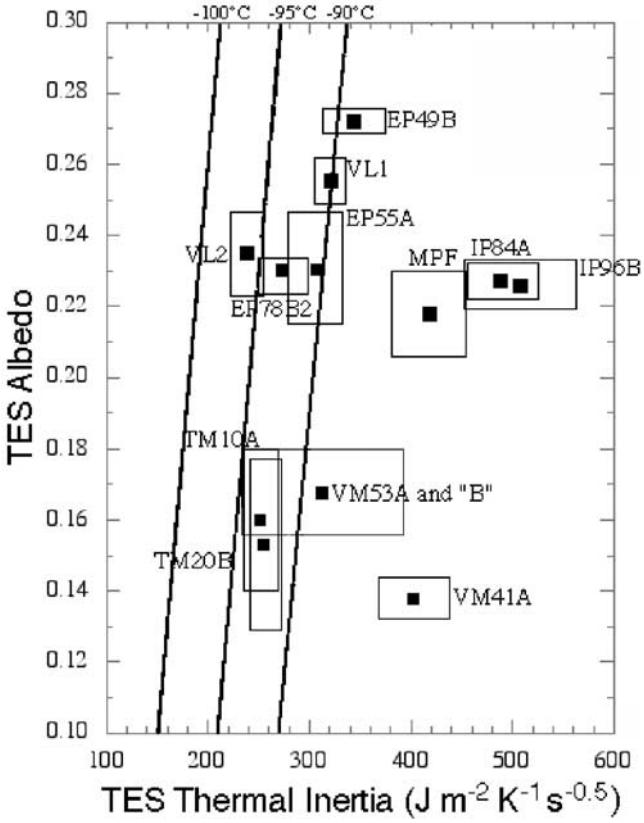

Figure 14. Thermal inertia versus albedo for the seven landing sites investigated in detail and the VL1, VL2, and MPF landing sites. Although the thermal inertia of these sites falls within the extremes or are similar to the VL1, VL2, and MPF landing sites, the sites fall into two groups based on albedo. One group of sites (Isidis, IP84A and IP96B; Athabasca, EP49B; Gusev, EP55A; and Elysium, EP78B) have generally high albedo (>0.21) and are similar to the VL1, VL2, and MPF landing sites, suggesting moderately dusty surfaces; another group of sites (Eos, VM41A; Melas, VM53A; and Meridiani, TM20B and TM10A) have low albedo (<0.18), suggesting relatively dust-free surfaces. Data are high-resolution TES data *Pelkey and Jakosky* [2002] and *Jakosky and Mellon* [2001] from within the ellipses shown in Figures 3–8 and 13; the square is the mean of the data within the ellipses, and boxes are the standard deviation. Three lines of constant 1 m air temperature are from *Martin et al.* [2003].

(0.5 m high) [*Golombek and Rapp*, 1997; *Golombek et al.*, 2003b] suggest ~0.04% at Meridiani and Elysium, ~0.2% at Gusev, and 0.8% at Isidis. *Golombek et al.* [2003b] calculate the probability of impacting such a potentially hazardous rock in the first two bounces for the average rock abundance at the sites as ~1% at Meridiani and Elysium, ~5% at Gusev and ~12% at Isidis. All of the sites meet the engineering requirement of <20% rock abundance, although the probability of impacting >1 m diameter rocks during the first two bounces is ~30% at such rocky sites. A total of 14, 10, 3, and 0 boulder fields composed of blocks 1.5–20 m diameter are visible in MOC images around impact craters in the Gusev, Isidis, Elysium, and Meridiani sites [*Golombek et al.*, 2003b]. Although these boulder fields have higher rock size-frequency distributions than the model, they do not add significantly to the hazardousness of the site because all relatively fresh craters are already assumed to be fatal in the simulations (section 12.2). Rocks large enough to place contact sensor instruments against and abrade should be plentiful within an easy Sol's drive at any of the sites [*Golombek et al.*, 2003b]. None of the rock abundance estimates are too high for the rovers to drive through, although progress would be slower at Isidis than at Meridiani, Elysium or Gusev.

[104] Comparison of the thermophysical properties of the sites with the Viking and Pathfinder landing sites (Figure 14 and Table 10) allows an interpretation of their surface characteristics. The Meridiani site has moderate thermal inertia and fine component thermal inertia and very low albedo. This site will likely look very different from the three previous landing sites in having a darker surface, few rocks and little dust. Melas Chasma has moderate thermal inertia and fine component thermal inertia and low albedo. This site will likely be moderately rocky (except where the surface is covered by sand dunes) but with less dust than the MPF and VL landing sites. Gusev crater and Elysium have comparable thermal inertia, fine component thermal inertia and albedo to the VL sites and so will likely be similar to these locations (just as dusty), but with fewer rocks. The Athabasca Valles site has high albedo and moderate thermal inertia, suggesting a moderately rocky and dusty site. The Isidis and Eos sites have high to very high thermal inertias suggesting a crusty surface. The Isidis site has moderate albedo and a high red/blue ratio, suggesting a rocky weathered crusty surface with some dust. Eos has low albedo with moderate to high thermal inertia, suggesting a rocky and crusty surface with some dust. These assessments are consistent with the formal TES derived measure of dustiness [*Ruff and Christensen*, 2002], which suggests Meridiani, Melas [*Pelkey and Jakosky*, 2002] and Eos should be relatively dust-free, and Athabasca, Isidis and Gusev should be relatively dusty compared with the VL1 or Mars Pathfinder landing sites.

11.2. Slopes

[105] Different analyses of hectometer and kilometer scale slope were carried out in support of landing site safety analysis, including the measurement and mapping of 1.2 km slopes at the landing sites and the mapping of 100 m slopes in and near the ellipses to directly compare with the engineering requirements [*Anderson et al.*, 2003]. To generate 1.2-km scale slope statistics for the landing sites, *Haldemann and Anderson* [2002] and *Anderson et al.* [2003] calculate bidirectional slopes (component of slope measured in a fixed direction) along individual laser altimeter tracks and then average the results in bins: 300 m to calculate statistics and 1.2 km to display the results in map view. Adirectional slopes (slope in downhill direction, or gradient) are calculated by averaging all MOLA elevation samples in a 1.2 km grid, and then evaluating the maximum slope between adjacent grid points, being careful to omit grids that have no MOLA measurements. These statistics are reported as averages (with standard deviations) and RMS over the landing ellipses. The km-scale slopes throughout the final four landing sites meet the engineering requirement of <2° (Table 10). Meridiani,

Gusev, Isidis and Athabasca appear smoothest at 1 km with average slopes ~0.2°, comparable with the VL1, 2 and MPF sites. Elysium appears slightly rougher at these wavelengths with an average slope of ~0.5°. The Melas and Eos landing sites are rougher at this scale with average slopes of ~1.2°, consistent with parts of their ellipses on the lower sloping parts of the canyon walls; these sites clearly have areas that exceed the engineering requirement of 2°.

[106] Slopes over 100 m length scales (required to be <5°) are addressed in two ways [*Anderson et al.*, 2003]. The first approach is to use MOLA pulse-width measurements as a measure of footprint-scale roughness [*Garvin et al.*, 1999; *Smith et al.*, 2001a; *Neumann et al.*, 2003], at the MOLA footprint size of 75–150 m, which can be used to infer upper limits for footprint-scale slopes. Early results from *Garvin et al.* [1999] and *Smith et al.* [2001a] that subtract out regional slopes, indicate pulse widths of <2 m had relief of <10 m, which corresponds to the slope requirement of <5° over 100 m baselines. These data show Gusev has the highest pulse spread (1.5 m), Meridiani the lowest (0.8 m), with the other sites in between (~1 m). Newer analysis that includes improvements in the estimated laser spot size (~75 m) and estimates of the RMS relief with and without longer slopes removed by *Neumann et al.* [2003], show Meridiani as having the lowest pulse spread (0.8 m) and Melas and Eos the highest (>3 m). The other sites cannot be readily distinguished from the VL1, 2 and MPF landing sites (~1–2 m). By these data, all of the four final landing sites should be acceptable and should be no worse than the three locations on Mars (VL1, 2 and MPF) where radar altimeters have worked satisfactorily in successfully landing spacecraft. The second approach to estimate relief and slopes over 100 m length scales is to assume that the Martian surface in the regions of the landing sites obeys self-affine statistics and to extrapolate the Allan deviation (relief) at 0.3, 0.6, 0.9, and 1.2 km MOLA shot intervals down to 100 m length scale via the Hurst exponent and determine the Allan variation and RMS slope [*Haldemann and Anderson*, 2002; *Anderson et al.*, 2003]. This method can be used to map the resulting 100 m slopes in and around the ellipses at about 0.2° resolution. These results are generally consistent with the pulse spread results (Table 10) showing Meridiani, Elysium and Isidis to be smooth, Melas and Eos as particularly rough and Gusev being the roughest of the final four sites at this scale.

[107] Stereogrammetry and PC results by *Kirk et al.* [2003] show slope probability distributions that are long tailed, with greater slopes at the extremes, compared with Gaussian distributions with the same RMS slopes. Bidirectional and adirectional RMS slopes at 3–6 m PC and 10 m stereo length scales are reported from *Kirk et al.* [2003] in Table 10. Bidirectional and adirectional slopes at a common 5 m length scale, corrected via the Hurst exponent [*Kirk et al.*, 2003], are discussed in this section and also reported in Table 10. These data indicate Meridiani is the smoothest site with adirectional RMS slopes of 2°–4°. The Elysium site is slightly rougher (3°–5° RMS slope) and comparable to the Mars Pathfinder site (~5° RMS). Isidis is slightly rougher (3°–9° RMS), followed by Gusev (4°–17°), Eos (7°–14°), and Melas (15°–18°). RMS bidirectional slope versus baseline derived from stereogrammetry and PC results [*Kirk et al.*, 2003] agree with 1.2 km baseline MOLA RMS bidirectional slopes, 100 m baseline MOLA Hurst exponent extrapolated slopes, and roughly 2 m baseline radar derived RMS slopes, suggesting all of these different techniques are producing consistent results for the final four landing sites. We now summarize the DEMs for the final four MER landing sites.

11.2.1. Gusev Crater

[108] Gusev has the greatest variety of morphologic/hazard units, from smooth cratered plains to much rougher, etched units [*Kirk et al.*, 2002, 2003]. Most units have relatively little albedo variation, and slopes from PC agree with those from stereo. RMS slopes derived from these units show a range from 9° to 17° for the etched terrain to lower values for the cratered plains (~5°).

11.2.2. Isidis Planitia

[109] The single stereo DEM inside the Isidis ellipse is dominated by a dense cluster of secondary impact craters (9°). The dark floors of the craters preclude use of PC. Spot stereo measurements were used to calibrate PC for two areas of cratered plains with more uniform albedo. Stereo-derived slopes were not estimated for these areas but the PC-derived slopes were 2°–3° [*Kirk et al.*, 2002, 2003].

11.2.3. Meridiani Planum

[110] This site is so smooth that stereo matching failed to produce usable results for several image pairs initially. In the absence of stereo data, a haze estimate for PC was obtained by comparing the heights and slopes of local dune forms to similar ones elsewhere for which better data were available [*Kirk et al.*, 2002]. Slopes obtained in a typical bland area of the site by this approach were small (1°–2°); apparent slopes in areas with prominent albedo variations were higher but could be discarded as artifacts. Subsequent successful stereo mapping of two image pairs with larger convergence angles, yielded low slopes (1°–2° RMS) in excellent agreement with those previously obtained from PC. Subdued craters had slightly higher slopes (2.5°).

11.2.4. Elysium Planitia

[111] Two stereo pairs in this ellipse have been analyzed, yielding slopes comparable to the smooth cratered plains in Gusev. A large wrinkle ridge crosses the stereo pair, so the model appears rougher (~3°–5° RMS) than typical for the ellipse. A PC solution in the cratered plains shows RMS slopes of 2°–4°.

11.3. Radar Reflectivity and Roughness

[112] The specular scattering regime radar cross sections at 3.5 cm meet the MER radar altimeter (5 cm wavelength) design requirement for six of the seven proposed sites (Table 10). The requirement is for the radar altimeter to acquire and maintain track over surfaces with an equivalent Hagfors Fresnel reflectivity greater than 0.03 and a Hagfors model RMS surface roughness less than 8°. Radar reflectivities have been measured at Meridiani (0.05) and at Isidis (0.03), with acceptable values, and estimated to be acceptable at Gusev (~0.04) and at Elysium (~0.05). The proposed Melas Chasma site falls just below the reflectivity requirement (0.02), although this assessment is based on sparse data from regions near, but not in the landing ellipse. Reflectivity values such as these indicate a surface with loosely constrained, but reasonable bulk densities

[*Golombek et al.*, 1997a] of ~1500 kg/m^3 at Meridiani and Elysium, ~1200 kg/m^3 at Gusev and ~1000 kg/m^3 at Isidis, that should pose no special problem to landing or roving and are similar to the range of bulk densities of soils that were successfully landed on and roved over by Mars Pathfinder [*Moore et al.*, 1999].

[113] Quasi-specular scattering can be analyzed to provide RMS slope values for length scales in the range of 10–100 times the wavelength. The RMS slope values at X-band (Table 10) are lower at the Meridiani (1.4°) and Isidis (3.3°) sites than at the Pathfinder landing site (4.5°). The Gusev site observed at S-band has a quasi-specular RMS slope of 1.7° and is smoother than the Viking 1 landing site (6°). Meter-scale RMS slopes are similar to those estimated from MOC stereo and PC analysis, with Meridiani the smoothest, Elysium and Isidis also smooth, and Gusev rougher. The diffuse scattering data provide information on the decimetric roughness of the sites that are of particular importance to rover trafficability. In general the sites appear benign for rover driving; as for the specular data, most of the sites are as rough, or less rough than the Viking and Pathfinder sites in the diffuse scattering channel. The notable exception is the proposed Athabasca site where at both 3.5 cm and 12.6 cm wavelengths the diffuse component of backscatter is very enhanced, suggesting decimeter roughness akin to that of a'a lava surfaces [*Harmon et al.*, 1999]. Gusev is the next roughest at decimeter scales. The X-band diffuse cross section there is not a concern, but the near equality of the diffuse scattering measured in both senses of circular polarization suggests that volume scattering in the near subsurface at Gusev is more important than at previous landing sites. Finally, *Haldemann et al.* [2003; submitted manuscript, 2003] make predictions regarding the appearance of the final four landing sites by comparisons to previous Mars landing sites. They suggest that (1) the Isidis and Elysium Planitiae sites will resemble the Viking 1 or Pathfinder site with gently rolling terrains, (2) the Meridiani Planum site will be much less rocky and smoother than the Viking 2 site, and (3) the Gusev crater site will have a combination of roughness at decimeter scales similar to or greater than the Viking 1 and Pathfinder sites, but will be smoother at meter scales.

11.4. Relative Landing Site Safety and Site Pairing

[114] Evaluation of the dominant three safety criteria (slopes, rocks and winds) indicates that Meridiani is probably the safest of the sites, followed by Elysium, Gusev and Isidis. Specifically, horizontal winds and wind shear are lowest at Meridiani and Elysium and higher at Gusev and Isidis. Rock abundance is lowest at Meridiani and Elysium, slightly higher at Gusev and higher still at Isidis. Slopes at the scale of the airbags are, in order of increasing slopes, Meridiani, Elysium, Isidis and Gusev.

[115] Because of their respective latitudes, to maximize surface lifetime only MER-A would go to Gusev and only MER-B would go to Elysium (either lander can go to Meridiani and Isidis). As a result, for the highest science priority sites, MER-A would go to Gusev and MER-B would go to Meridiani. For the two safest sites, MER-A would go to Meridiani and MER-B would go to Elysium. For Meridiani and Isidis, either lander could go to either site, although mission lifetime would be maximized if MER-A went to Meridiani (farther south) and MER-B went to Isidis (farther north).

12. Landing Success Assessment

12.1. Landing Simulation

[116] EDL analysis with respect to differentiating system performance between the four candidate landing sites was conducted using a three-stage Monte Carlo simulation employing 2000 individual trials per scenario run. Each scenario examined the effects of different assumptions regarding the specific terrain, winds, ground hazards, and vehicle performance. The output of this process is a landing site-dependent probability that the vehicle will encounter a situation with respect to its velocity, or the terrain, that is considered to be within the validated performance capability of the system.

[117] An important aspect of the simulation analysis is that the goal is to provide a means to gauge relative risk between sites rather than provide an absolute metric quantifying the probability of success or failure. Consequently, results were binned as either "within specification" or "out of specification." There are two prime reasons for this subtle distinction. First, no provisions were made to model the probability that electronic components or mechanical subassemblies will fail due to causes such as stochastic variations in the quality of manufacturing. Cases judged to be "out of specification" only resulted from interaction of the system with environmental factors such as winds, rocks, and slopes, or from performance variations of properly operating systems. Second, the landing system contains very few sharp thresholds where crossing a validated subsystem performance boundary will result in certain failure. As a simplifying assumption, no provisions were made to model degraded, but possibly survivable performance beyond validated limits. Consequently, the simulation results may underestimate the actual reliability of the system with respect to the landing site environments.

[118] In the evaluation process, key system parameters such as velocities, forces, temperatures, and time constraints were checked against a set of performance "redline" limits during each of the three simulation stages. Within a stage, individual Monte Carlo trials that satisfied all of the constraints of that particular phase of the descent were judged to be within specification. Subsequently, those trials were allowed to continue to the next successive simulation stage with the output state vector of the current stage serving as the input conditions for the following stage.

[119] The first of these three stages involved a 6-degree-of-freedom simulation of the vehicle's trajectory from the atmospheric entry point at 125 km altitude to the point of parachute deployment. The primary statistical factors that were considered in this phase included the capability to accurately target the vehicle to its atmospheric entry aim point, aerodynamic properties of the entry capsule under hypersonic flight conditions, and atmospheric density variations. Results from this stage of the simulation are not discussed in this paper because over 99.5% of all scenarios run were judged to be within specification against the performance metrics. In addition, postsimulation analysis revealed that the results of this stage did not vary significantly between the landing sites.

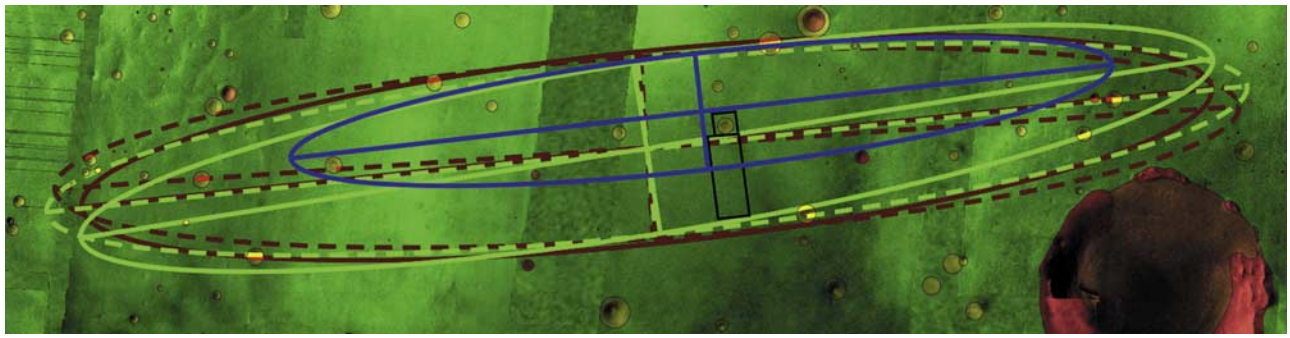

Figure 15. Hazard unit map of the Meridiani Planum site. Ellipses are as in Figure 3. The green unit is background plains. The stereo 10 m DEM for this unit is the southern rectangle (MOC image is Figure 16). Yellow circles are degraded, low-relief subdued craters. The stereo 10 m DEM for the degraded crater is the northern box (MOC image is Figure 16). Red circles are fresh craters. See Table 11 for areas, slopes, and relief of each unit.

[120] Stage two involved an 18-degree-of-freedom simulation of the vehicle's trajectory from parachute deployment to a point just after retrorocket burn completion, but prior to ground impact. In this phase, the vehicle is in what is referred to as ''multibody configuration'' with the backshell suspended under the parachute, and lander suspended under the backshell via a 20-m-long bridle. Six degrees of freedom each are modeled for these three components. Major statistical variations that contributed to dispersions in this stage's output included parachute aerodynamic stability properties, wind variations, performance of various terminal descent sensors, and the accuracy of retrorocket performance. In addition, the actual flight software code that will be used to fire the retrorockets was incorporated into the simulation.

[121] Although all trials for all scenarios were judged to be within specification for stage two, there was significant variation in system performance across the four landing sites due to differences in wind conditions predicted by meoscale modeling efforts [*Kass et al.*, 2003]. For example, the contribution of prevailing winds to the final touchdown velocity at the Meridiani and Elysium sites is less than 5 m/s on average, while values at Gusev and Isidis are in the range of 8–10 m/s on average with peaks near 20 m/s. In addition, the turbulence at Gusev and Isidis, as compared to the other two sites, results in higher touchdown velocities and creates more stressing conditions for airbag survival in the final stage.

[122] The third and final stage involved a three-degree-of freedom simulation of the airbag-encapsulated lander bouncing across the Martian surface from the point of first impact to roll stop. On any given bounce, a check was performed to determine whether the vehicle's velocity relative to the simulated terrain exceeded the expected survival threshold. This velocity limit was derived from full-scale drop testing in a vacuum chamber at the NASA Plum Brook station in Sandusky, Ohio and is a function of impact incident angle, spin rate, and the size and shape of any rocks struck. Depending on the specific conditions, the airbags are expected to survive at impacts as high as 26 m/s.

12.2 Surface Hazard Terrains

[123] The simulated terrain consisted of 3-m or 10-m resolution digital elevation maps (several square kilometers in area) generated by *Kirk et al.* [2003] using stereogrammetry and photoclinometry techniques on MOC stereo images of representative portions of the landing ellipse. Rocks were randomly scattered on this digital terrain using the standard exponential size-frequency distribution with rock abundance percentage derived from Viking IRTM data [*Golombek and Rapp*, 1997; *Golombek et al.*, 2003b].

[124] Hazard terrain maps were generated for each landing area so that the specific DEMs could be extrapolated to other areas throughout the ellipse. The maps are based on geomorphology and surface roughness and slope derived from MOC and THEMIS images. For each ellipse, two to four terrains were identified and correlated to specific DEMs [*Kirk et al.*, 2003] for use throughout the ellipse.

[125] The Meridiani hazard map (Figure 15) includes a background terrain and degraded low-relief craters (Figure 16). Both of these units have low slopes and low relief (Table 11). About 70 degraded low-relief craters ranging is diameter from 0.5 to <2 km, were mapped within the ellipses. Stereo 10-m DEMs were used to simulate landing in each of these terrains with slope and relief for these DEMs shown in Table 11. The Meridiani Planum site has a 94% chance of landing in extremely benign terrain (RMS slope $\sim 2^\circ$) and a 4% chance of landing in fairly smooth subdued craters with $\sim 4^\circ$ RMS slope.

[126] Elysium (Figure 17) has a background cratered plains unit ($\sim$100 m relief; Figure 18a) and a higher relief unit ($\sim$150 m) defined by large wrinkle ridges and mounds (Figure 18b), represented by 3-m PC and 10-m stereo DEMs, respectively (Table 11). The Elysium Planitia site has a 91% chance of landing in cratered plains with an RMS slope of $\sim 4^\circ$ and a 7% chance of landing in slightly rougher terrain (RMS slope of $\sim 5^\circ$).

[127] Isidis (Figure 19) has a background plains unit with low slopes (Figure 20a), a more heavily cratered plains unit with higher slopes (Figure 20b), and a secondary crater swarm unit with still higher slopes (Figure 20c), represented by two 3-m PC and one 10-m stereo DEMs, respectively. The Isidis Planitia site has about a 91% chance of landing in cratered plains with an RMS slope of $\sim 3^\circ$ and a 5% chance of landing in slightly rougher terrain (4.5° RMS slope).

[128] Gusev (Figure 21) has a background cratered plains unit (Figure 22a), a more heavily cratered plains unit

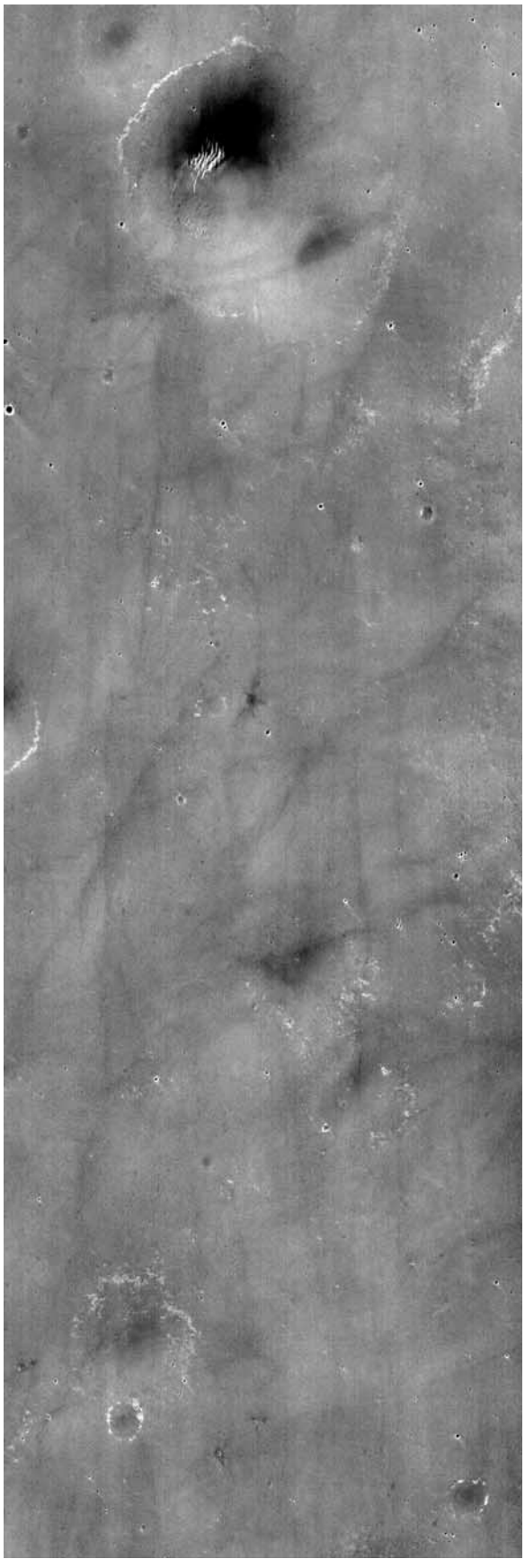

(Figure 22b), and an etched terrain unit (Figure 22c), which are represented by a 6-m PC and two 3-m PC DEMs, respectively; two of these units have moderate slopes and the etched terrain has high relief and high slopes. The Gusev crater site has an 85% chance of landing in cratered plains with an RMS slope of ~4°, a 6% chance of landing in only slightly rougher terrain (4.5° RMS slope) and a 6% chance of landing in very rough terrain (RMS slope of 9.5°).

[129] All of the ellipses have a unit of fresh craters larger than ~200 m that appear to have fresh bowl shapes and are morphologically distinct from the craters in the units just described. The largest fresh crater in any of the ellipses is ~2 km. The Meridiani, Elysium, Isidis and Gusev ellipses have about 2, 22, 75 and 70 fresh craters with a 0.5%, 0.8%, 1.1% and 1.5% probability of landing in these fresh craters, respectively (Table 11). Because of the steep slopes that could spoof the altimeter and cause mistimed firing of the retrorockets, landing in these areas was assumed to be not survivable in the simulation, even though landing inside many of these craters would be survivable. Total relief of these craters are assumed similar to fresh bowl shaped craters with depths of ~20% and rim heights ~4% of their diameters.

[130] These hazard maps are consistent with the slopes over the ellipses derived from photoclinometry [*Beyer et al.*, 2003] and the geologic and morphologic maps [e.g., *Milam et al.*, 2003; *Arvidson et al.*, 2003]. The slopes and relief of the hazard units within the ellipses further demonstrate that the Meridiani site has the lowest slopes, followed by Elysium and Isidis sites, with parts of Gusev having the highest slopes at the 3–10 m scale.

12.3. Landing Simulation Results

[131] Overall, the simulation results indicate that the Meridiani Planum site is likely to be the safest among the four candidates with 96% in-specification landings weighted for the three hazard units. The high rating is due to low expected winds, combined with a low rock abundance of 6% and relatively gentle slopes (the dominant three concerns). Sensitivity studies of results at this site were robust to modeling uncertainties. For example, increasing the rock abundance by the 5% to account for the 20% uncertainty in the estimate, or doubling the wind speed, or assuming a 10% degradation in airbag performance capability reduced the percentage of in-specification landings to no lower than 90%.

[132] Simulations at Elysium Planitia indicated 95% of landing are within specification weighted for the three hazard units within the ellipse. This result is statistically indistinguishable from Meridiani from a risk evaluation perspective due to an estimated ±3% calculation uncertainty within the simulation. This figure includes statistical run to

Figure 16. (opposite) MOC image of hazard units in the Meridiani Planum site for which DEMs were used in the landing simulations. The subdued, shallow, degraded crater is a box around the northernmost crater in the image. The rest of the image is the background plains. MOC image E18-01595 is about 4.1 km wide, with north up. The image is outlined in the hazard map of Figure 15. See Table 11 for areas, slopes, and relief of units.

Table 11. Hazard Units in Ellipses[a]

Unit	% Area in Ellipse	Landing Probability, %	RMS Slope, deg	Mean Slope, deg	Max Relief, m
		Meridiani			
Fresh craters	0.2	0.49	>15		310
Subdued craters	4.6	4.40	3.7	2.9	70
Background plains	95.2	93.97	1.9	1.5	47
		Elysium			
Fresh craters	1.4	0.83	>15		410
Large wrinkle ridges and mounds	6.2	7.43	5.2	4.3	143
Cratered plains	92.5	90.6	4.0	3.4	108
		Gusev			
Fresh craters	1.6	1.55	>15		500
Etched terrain	4.7	5.96	9.5	7.8	232
Heavily cratered plains	3.2	6.17	4.5	3.6	49
Cratered plains	90.5	85.18	4.1	3.2	52
		Isidis			
Fresh craters	1.1	1.12	>15		290
Secondary swarms	3.4	1.28	8.4	6.2	79
Heavily cratered plains	10.1	5.51	4.5	3.4	55
Cratered plains	85.4	90.95	3.1	2.4	66

[a]Landing probability is the probability of landing in that unit within the 3σ ellipses discussed in section 9. RMS and mean slope are from MOC stereo and/or PC 3 or 10 m (comparable) DEM sample for that unit. Max relief is the maximum relief found within the DEM sample from *Kirk et al.* [2003]. The maximum relief is assumed to be 0.24 times the largest fresh crater diameter in the ellipse (the depth is 20% and the rim height is 4% of the diameter, respectively).

run variations due to the Monte Carlo sample size and an estimation of known physical second-order effects not modeled. However, the uncertainty does not include an estimation of the accuracy of environmental models such as rocks or wind. Similar to Meridiani, Elysium results are relatively insensitive to modeling uncertainty and are influenced primarily by low winds, low rocks, and low slopes.

[133] Scenarios run for the Gusev crater site resulted in 91% of landings that were within specifications, weighted for the four hazard units within the ellipse. This figure is slightly lower than Meridiani and Elysium due to higher expected winds, higher turbulence, a slightly elevated rock abundance of 8%, and slightly steeper slopes. Furthermore, the in specification landings decrease to roughly 80% by increasing the winds or decreasing airbag performance, so uncertainties in modeling assumptions are important at this site. The etched terrain within the Gusev ellipse is the most hazardous unit, resulting in only 75% of landings that are within specification.

[134] Simulations of landings at Isidis Planitia produced results statistically similar to Gusev. About 89% of landings at this site were within specification for the four hazard units within the ellipse. The two sites are different in that Isidis has higher rock abundance (14%), but has slightly lower expected winds than Gusev. To first order, these two differences offset each other within the simulation.

[135] The simulations also produced critical data not evident in a cursory examination of the aggregate in-specification percentages. Data were saved for all the Monte Carlo trials, and analysis was performed to determine the root cause of cases that were judged to be out of specification. This type of analysis enabled the project to make qualitative assessments of risk between the four candidate landing sites, and also enabled the engineering team to fine tune software control parameters to increase successful landing at each site.

12.4. Final Landing Site Positioning

[136] Updated analysis of margins and navigation delivery accuracy yielded smaller ellipses that allowed fine tuning of their exact location within the landing sites. These ellipses varied from 80 to 115 km long and 10 to 12 km wide for MER-A and MER-B, respectively. Because the Gusev site includes etched terrain that had the lowest percentage of within specification landings (~75%), ellipses that minimized the probability of landing in this terrain were sought. To facilitate this search a hazard map of the entire Gusev crater (Figure 21) based on a THEMIS visible image (18 m/pixel) mosaic (Figure 23) was produced. Multiple ellipses were quantitatively tested to find the ellipse with the lowest total probability of out of specification landings by convolving the probability landing ellipse with the in specification probability of the individual terrains within each ellipse. Results indicated 91% in specification landings with the 81 × 12 km ellipse oriented at an azimuth of 75° (designated EP55A3) centered at

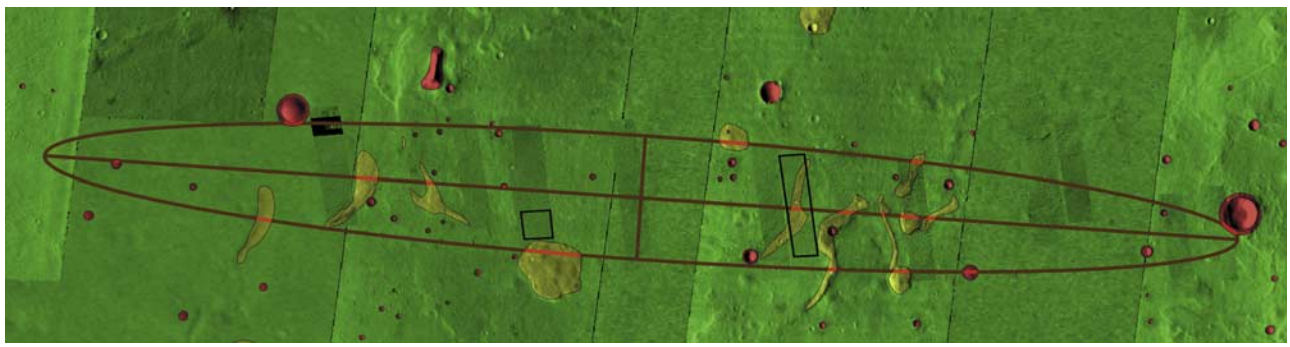

Figure 17. Hazard unit map of the Elysium Planitia site. The ellipse is as in Figure 13. The green unit is the background cratered plains. The yellow unit is large wrinkle ridges and large mounds. Red circles are fresh craters. The left box is the location of the 3 m PC DEM used for the cratered plains (MOC image is Figure 18a). The right rectangle is the location of the 10 m stereo DEM used for the wrinkle ridge and mound unit (MOC image is Figure 18b). See Table 11 for areas, slopes, and relief of each unit.

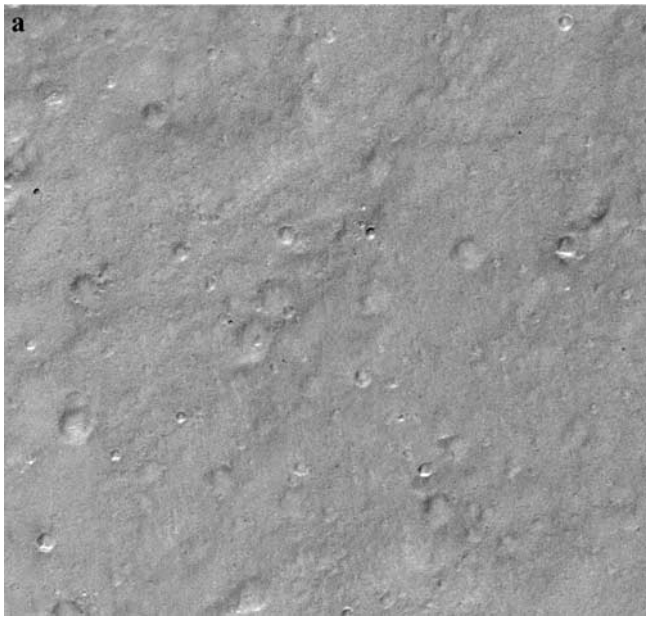
a


b

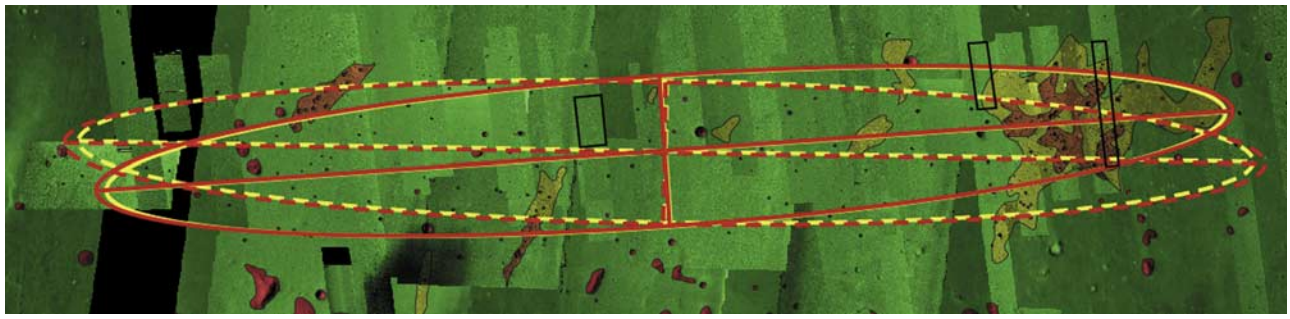

Figure 19. Hazard unit map of the Isidis Planitia landing site. Ellipses are as in Figure 6. The green unit is the background cratered plains. The west rectangle is the location of the 3 m PC DEM used for the cratered plains (MOC image is Figure 20a). The yellow unit is more heavily cratered terrain. The central rectangle is the location of the 3 m PC DEM used for this unit (MOC image is Figure 20b). The brown unit is secondary crater swarms. The eastern rectangle is the location of the 10 m stereo DEM used for this unit (MOC image is Figure 20c). Red circles are fresh craters or hills. See Table 11 for areas, slopes, and relief of each unit.

14.59°S, 175.30°E in the MOLA IAU 2000 coordinate frame.

[137] Analysis of minimum nighttime temperatures using TES data indicated that the Meridiani site is the coldest with the lowest temperatures in the western portion of the ellipse [*Martin et al.*, 2003]. THEMIS thermal images were used to create a thermal inertia map [*Fergason and Christensen*, 2003] that was converted to a minimum predicted nighttime temperature map (Figure 24). The THEMIS results confirm the western portion of the ellipse is relatively cold and the ellipse was positioned to maximize the surface temperature within the area of greatest MOC image coverage (Figure 3) for the longest surface mission. This ellipse is designated TM20B3 and is centered at 1.98°S, 353.06°E in MOLA IAU 2000 coordinate frame and is 81.5 × 11.5 km oriented at an azimuth of 84.5°.

13. Final Deliberations, Reviews, and Selection

[138] Activities at the fourth Landing Site Workshop concentrated on documenting scientific hypotheses related to the evolution of each site that could be evaluated using the Athena science payload. The purpose was to ensure that all ideas related to the setting of the sites had been vetted and how the Athena science payload might specifically help test competing hypotheses. The workshop resulted in a list of scientific "pros" and "cons" for each site and hypotheses for each site together with observations and measurements required to test them (Tables 6–9). The lists of testable hypotheses form the basis for initial operations on Mars and confirmed that the Meridiani Planum and Gusev crater sites were the top two sites based on science, with Isidis and Elysium ranked considerably lower.

[139] The Athena Science Team met shortly after the fourth landing site workshop and provided site recommendations based only on science considerations. Recommendations were based upon scientific characteristics of the sites, the objectives of the Athena investigation, the capabilities of the Athena payload and the MER rovers, and other factors like mission lifetime that impact science return. The Athena Science Team recommendations were wholly consistent with the community consensus voiced at the landing site workshops that concluded Meridiani Planum and Gusev crater were the top choices for science. In addition, the Science Team also considered alternate scenarios regarding the science potential of the sites. For example, if safety issues were to eliminate both the Gusev crater and Isidis Planitia sites from consideration, there was near-unanimous consensus that the two sites should be Meridiani Planum and Elysium Planitia, rather than sending both rovers to Meridiani. Finally, if a launch accident or other events were to make it necessary to choose a single landing site, the Science Team preferred Meridiani over Gusev by a ~2:1 margin. The MER project considered all safety, engineering, and science factors, and recommended that MER-A be sent to Gusev and MER-B be sent to Meridiani. This selection acknowledged that the slightly greater risk at Gusev was warranted by the compelling case for addressing the scientific objectives of the mission at this site. An external peer review of the entire process occurred in late March 2003 and endorsed the site selection process and the selected sites. NASA Headquarters selected the Gusev and Meridiani landing sites for MER-A and MER-B, respectively, in April 2003 and explicitly accepted the slightly higher risk at Gusev for the potentially greater science return.

14. Summary/Conclusions

[140] 1. Selection of the MER landing sites has spanned more than two years and incorporated the participation of broad sections of the planetary sciences community. For the first time, the science community selected high science priority sites from hundreds of potential sites that met the

Figure 18. (opposite) MOC images of terrain hazard types in the Elysium Planitia landing site for which DEMs were used in the landing simulations. (a) Background cratered plains. MOC image E22-00378 is about 3.75 km wide, with north up. (b) Wrinkle ridge and mound unit. MOC image E18-00429 is about 3.2 km wide, with north up. The images are outlined in the hazard map of Figure 17. See Table 11 for areas, slopes, and relief of units.

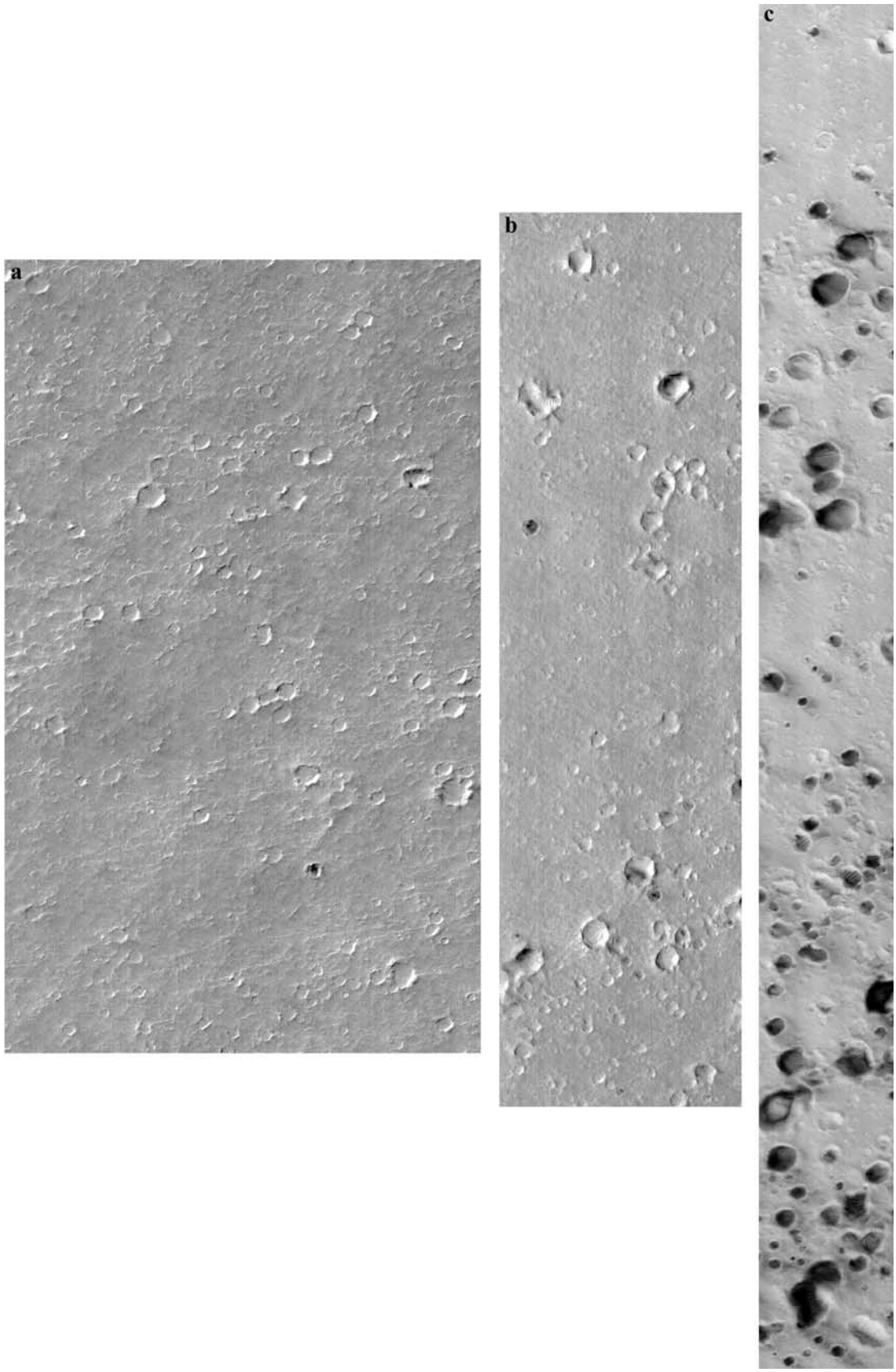

Figure 20. MOC images of terrain hazard types in the Isidis Planitia site for which DEMs were used in the landing simulations. (a) Cratered plains. MOC image E22-00281 is about 3.1 km wide, with north up. (b) Heavily cratered terrain. MOC image E18-00196 is about 2.1 km wide, with north up. (c) Secondary swarm. MOC image E14-01522 is about 1.2 km wide, with north up. The images are outlined in the hazard map of Figure 19. See Table 11 for areas, slopes, and relief of units.

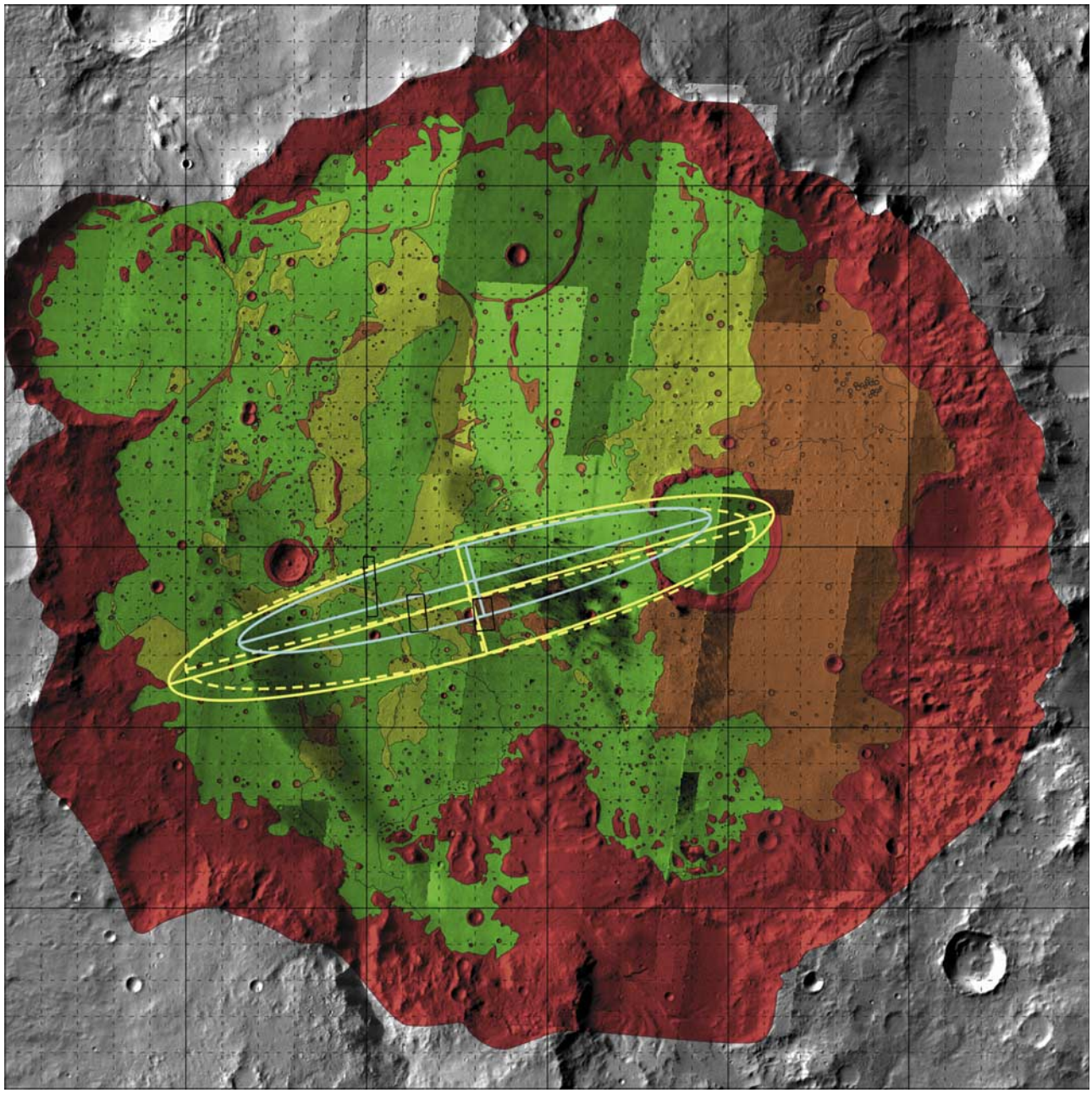

Figure 21. Hazard unit map of the Gusev crater site based on 18 m/pixel THEMIS visible and MOC images. Ellipses are as in Figure 4. The small blue ellipse is final after the positioning discussed in section 12.4. The green unit is the background cratered plains. The PC 3 m DEM for this unit is shown by the westernmost rectangle (MOC image is Figure 22a). The yellow unit is more heavily cratered plains. The PC 6 m DEM for this unit is shown by the central rectangle (MOC image is Figure 22b). The brown unit is etched terrain. The PC 3 m DEM for this unit is shown by the easternmost rectangle (MOC image is Figure 22c). Red circles are fresh craters. See Table 11 for areas, slopes, and relief of each unit. Solid grid lines are 0.5° in latitude and longitude in the IAU 2000 reference frame. The area shown is 174°–177°E, 13°–16°S. The final (small) ellipse shown (EP55A3) is centered at 14.59°S, 175.30°E and is 81 × 12 km, oriented at an azimuth of 75°.

basic engineering criteria. These sites were targeted for acquisition of orbital data from MGS and Mars Odyssey that allowed prospective sites to be studied for both science and safety to an unprecedented level. The final sites are the most imaged, most thoroughly studied locations on Mars.

[141] 2. Mapping first-order engineering constraints for landing sites onto Mars eliminates 95% of the surface area of the planet, leaving a thin equatorial band, below −1.3 km elevation that is not dominated by potentially thick deposits of fine-grained dust. Of the remaining terrain, approximately 100 potential landing sites 80–220 × 30 km were sited for

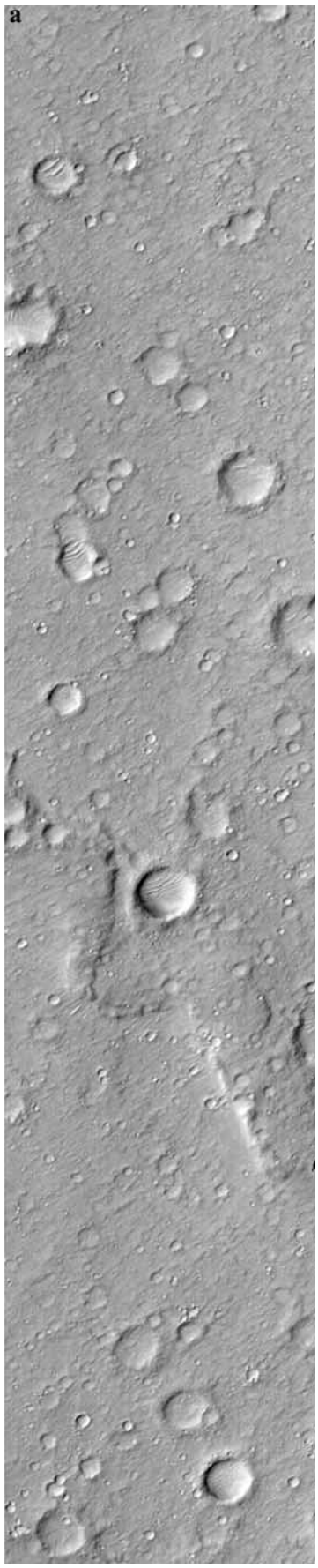

MER-A between 15°S and 5°N and ~85 potential landing sites 130–330 × 30 km were sited for MER-B between 10°S and 10°N in areas free of obvious hazards in Viking digital image mosaics.

[142] 3. The science objectives of the mission to search for evidence of past aqueous activity and assess the past habitability of the environment formed the basis for selecting the 25 highest-priority landing sites for study at the First Landing Site Workshop. After acquisition of MGS data from these sites, the six highest-priority landing sites were selected at the Second Landing Site Workshop on the basis of science and safety for further study.

[143] 4. Engineering sensitivity studies showed that the three most important criteria for landing site safety are horizontal winds, shear and turbulence in the lowest few kilometers of the atmosphere (which imparts a horizontal velocity to the lander), 10-m-scale slope that contributes to airbag bounce and spin-up, and rocks that can abrade or exceed the stroke of the airbags. Atmospheric models argued for high winds at the sites inside Valles Marineris and combined with concerns related to high slopes eliminated Melas and Eos Chasmata from further consideration at the Third Landing Site Workshop. Athabasca Valles was later removed from consideration due to concerns over extreme decimeter-scale roughness (that could negatively impact landing safety and rover trafficability) indicated by extraordinary radar returns.

[144] 5. The search for an additional safe, low-wind site, involved evaluating atmospheric circulation models for quiet regions for the season and time of arrival with relaxed elevation and latitude constraints. Three areas, Terra Meridiani, Elysium Planitia and southeast of Isidis Planitia, were investigated in more detail using higher-resolution wind models to verify that the atmosphere was quiet and by evaluating potential ellipses for their science potential and safety. Two sites on the highland/lowland boundary in Elysium Planitia were judged the highest science potential and were targeted for acquisition of new MOC and THEMIS images. One ellipse was selected for further consideration based on slightly lower winds, lower relief and slopes, and lower rock abundance.

[145] 6. The final four landing sites that remained under consideration were Meridiani Planum, Gusev crater, Isidis Planitia and Elysium Planitia. Of these sites, Meridiani Planum, which shows clear mineralogical evidence of coarse grained hematite that may have formed via precipitation from liquid water or hydrothermal alteration, and Gusev crater, which shows clear morphological evidence that it was a crater lake with interior sediments deposited in standing water, are the highest-priority science sites. Isidis and Elysium Planitiae are located to sample ancient

Figure 22. (opposite) MOC images of terrain hazard types in the Gusev crater site for which DEMs were used in the landing simulations. (a) Cratered plains. MOC image M03-01042 is about 2.8 km wide, with north up. (b) Heavily cratered plains. MOC image E19-00218 is about 2.9 km wide, with north up. (c) Etched terrain. MOC image E18-00184 is about 3 km wide, with north up. The images are outlined in the hazard map of Figure 21. See Table 11 for areas, slopes, and relief of units.

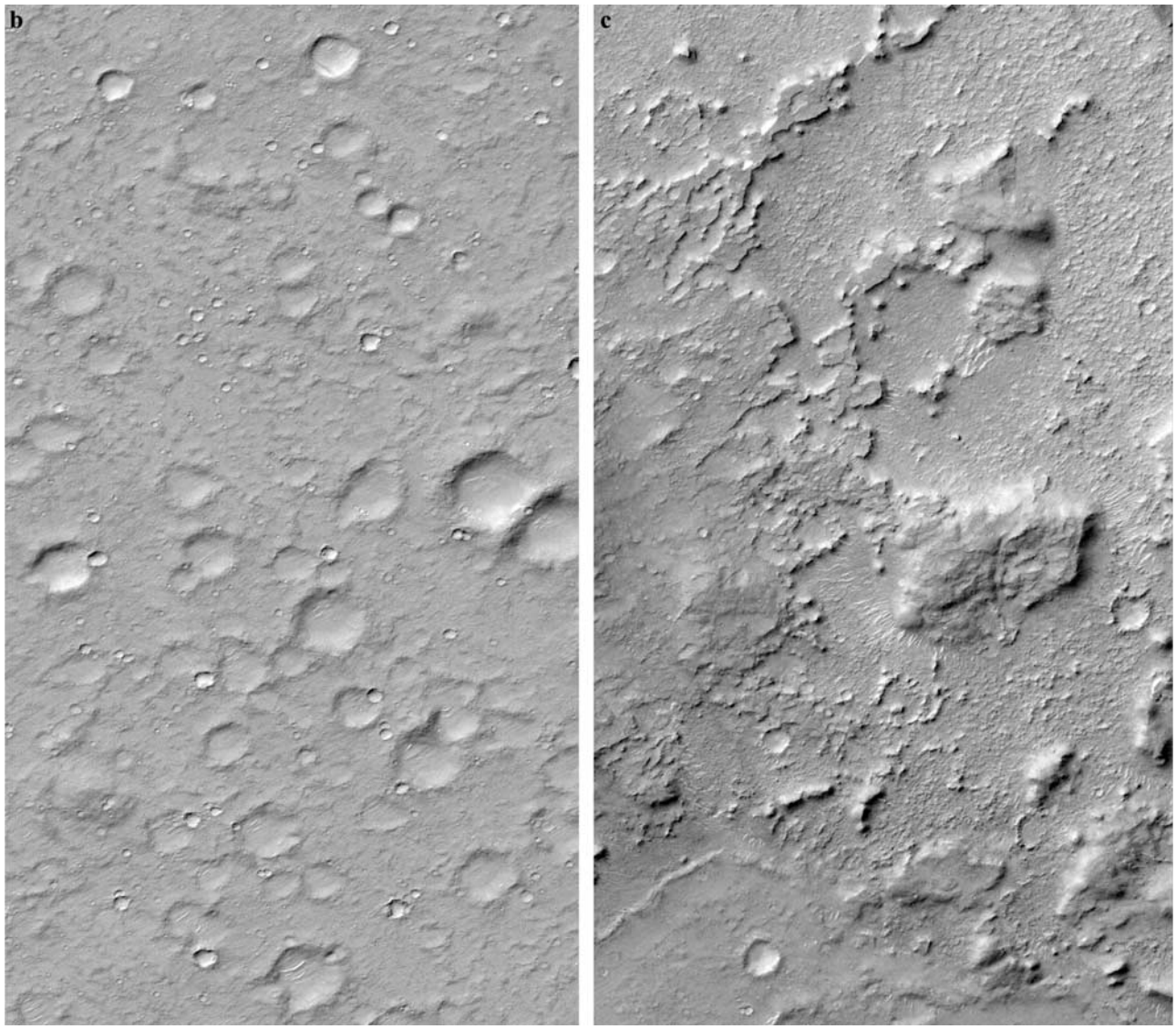

Figure 22. (continued)

Noachian highland rocks and have lower science priority, respectively.

[146] 7. Comparison of the thermophysical properties of the sites with the Viking and Pathfinder landing sites allows an interpretation of their surface characteristics. The Meridiani site has moderate thermal inertia and fine component thermal inertia and very low albedo. This site will likely look very different from the VL and MPF landing sites in having a darker surface, few rocks and little dust. Gusev crater and Elysium have comparable thermal inertia, fine component thermal inertia and albedo to the VL sites and so will likely be similar to these locations (just as dusty), but with fewer rocks. The Isidis site has high thermal inertia (bulk and fine component) moderate albedo and a high red/blue ratio, suggesting a rocky, weathered crusty surface with some dust.

[147] 8. Evaluation of the dominant three safety criteria (winds, 10-m-scale slopes, and rocks) indicates that Meridiani is probably the safest of the sites, followed, in order, by Elysium, Gusev and Isidis. Specifically, horizontal winds and wind shear are lowest at Meridiani and Elysium and higher at Gusev and Isidis. Rock abundance is lowest at Meridiani and Elysium, slightly higher at Gusev, and higher still at Isidis. Slopes at the scale of the airbags are in order of increasing slopes: Meridiani, Elysium, Isidis and Gusev.

[148] 9. Mapping of hazard units in the ellipses and application of 10 m to 3 m digital elevation models for these units for simulations of landing success at each site further underscores the general safety characterization. The Meridiani Planum site has a 94% chance of landing in extremely benign terrain (RMS slope $<2^\circ$) and a 4% chance of landing in fairly smooth subdued craters with $\sim 4^\circ$ RMS slope. The Elysium Planitia site has a 90% chance of landing in cratered plains with an RMS slope of $\sim 4^\circ$ and a 7% chance of landing in slightly rougher terrain (RMS slope of $\sim 5^\circ$). The Isidis Planitia site has about a 90% chance of landing in cratered plains with an RMS slope of $\sim 3^\circ$ and a 5% chance of landing in slightly rougher terrain (4.5° RMS slope). The final Gusev crater site has an 86% chance of landing in cratered plains with an RMS slope of

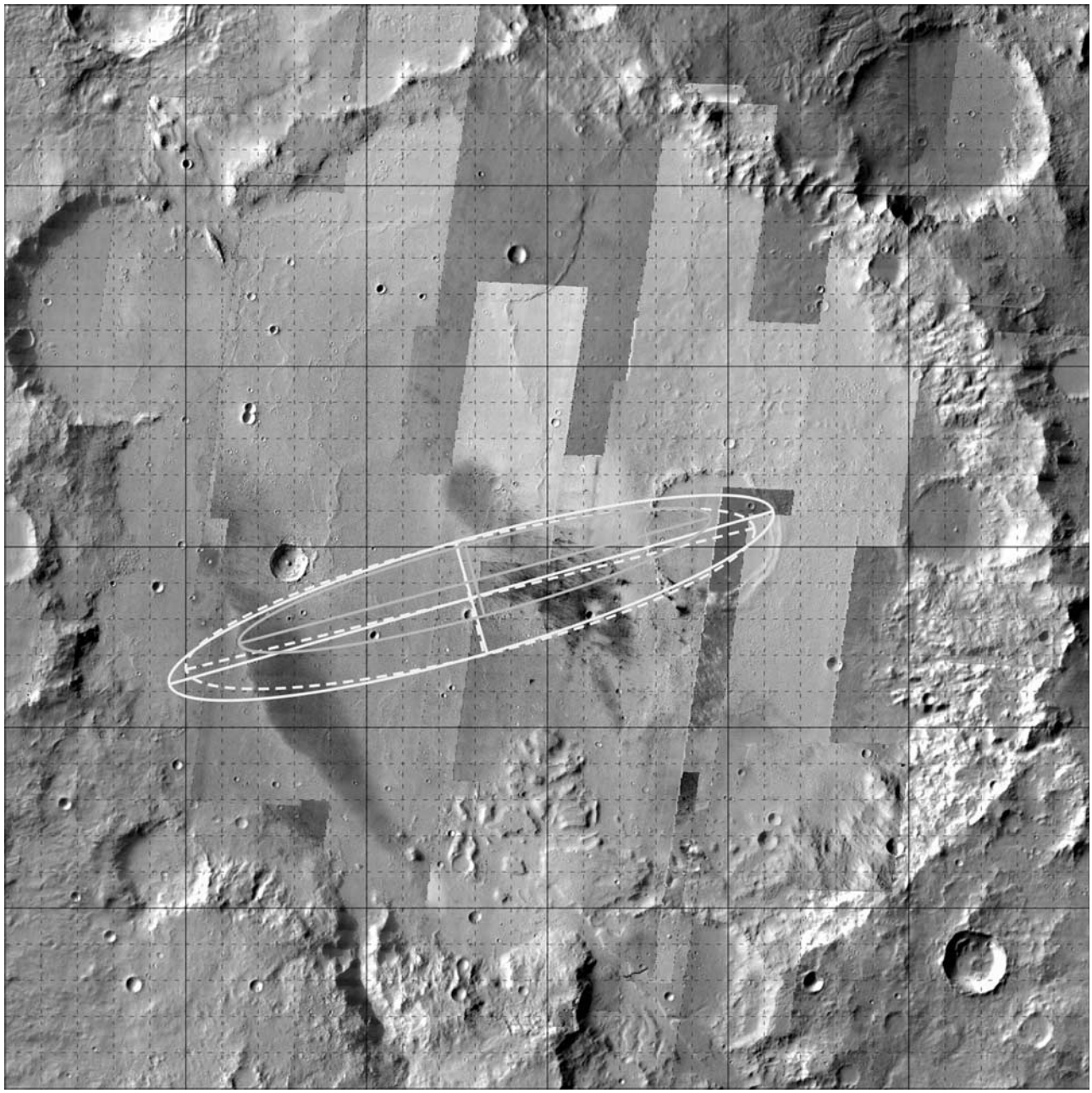

Figure 23. THEMIS visible image (18 m/pixel) and daytime thermal image (100 m/pixel) mosaic used to map hazard units throughout Gusev crater (Figure 21). Visible images are roughly 20-km-wide swaths oriented north-northeast and were particularly useful for extending hazardous units defined in high-resolution MOC images concentrated in the ellipse to broader areas where MOC images were not present. The mosaic shows larger ellipses used for science (section 9) and safety (section 11) evaluations and smaller final ellipses positioned to minimize the probability of landing in hazardous terrain. The ellipses and the area shown are the same as in Figure 21. Solid grid lines are 0.5° in latitude and longitude in the IAU 2000 reference frame. The final (small) ellipse shown (EP55A3) is centered at 14.59°S, 175.30°E and is 81 × 12 km, oriented at an azimuth of 75°.

~4°, a 11% chance of landing in only slightly rougher terrain (4.5° RMS slope), and a 2% chance of landing in very rough terrain (RMS slope of 9.5°).

[149] 10. A sophisticated three-stage Monte Carlo simulation of landing, including atmospheric entry, descent, and landing on mapped hazard unit digital elevation models indicated that about 96% of the cases were within specification of the landing system at Meridiani, followed by 95% at Elysium, and ~90% at Gusev and Isidis, consistent with the evaluation of relative site safety based on the dominant three safety criteria.

[150] 11. Final ellipses that included updated analysis of margins and navigation delivery accuracy varied from 80 to 115 km long and 10 to 12 km wide for MER-A and MER-B,

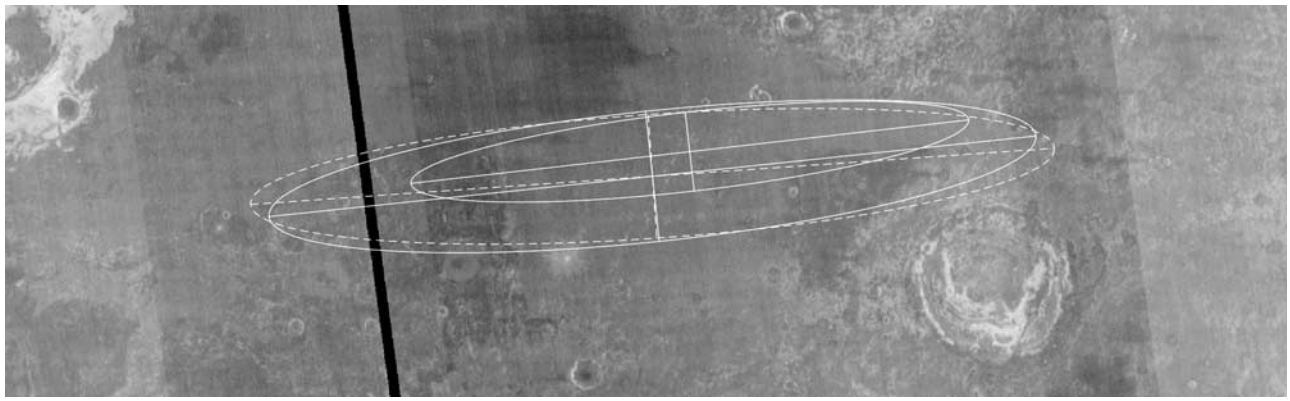

Figure 24. THEMIS predicted minimum nighttime temperature mosaic of Meridiani Planum for L_s = 25.0 (end of the 90 Sol nominal MER-B mission) at 6:00. The mosaic was produced by converting THEMIS thermal images (100 m/pixel) to thermal inertia maps via the method described by *Fergason and Christensen* [2003] and then converting them using the same assumptions to a common minimum predicted nighttime surface temperature. The mosaic confirms colder temperatures observed in TES thermal inertia maps in the western portion of the larger ellipse used for science (section 9) and safety (section 11) evaluations (Figures 3 and 15). The smaller ellipse is located to maximize surface temperature in regions with significant MOC coverage (Figure 3). The final (small) ellipse shown (TM20B3) is centered at 1.98°S, 354.06°E and is 81.5 × 11.5 km, oriented at an azimuth of 84.5°. Surface temperatures vary between 168 K (dark) and 200 K (light).

respectively, and were sited to minimize the chances of landing in potentially hazardous terrain mapped in THEMIS visible images in Gusev crater and to maximize the surface lifetime indicated by warm surface temperatures derived from THEMIS thermal images at Meridiani Planum. The final ellipse at Gusev is designated EP55A3 and is centered at 14.59°S, 175.30°E in the MOLA IAU 2000 coordinate frame and is 81 × 12 km oriented at an azimuth of 75°. The final ellipse at Meridiani is designated TM20B3 and is centered at 1.98°S, 354.06°E in MOLA IAU 2000 coordinate frame and is 81.5 × 11.5 km oriented at an azimuth of 84.5°. Both ellipses have nearly complete MOC coverage.

[151] 12. The Athena Science Team and MER project recommended Meridiani and Gusev for the final two landing sites based on the combined science and safety evaluations and the results of the landing simulations. The process and recommendation were approved of by an independent peer review group and NASA Headquarters selected the Meridiani and Gusev landing sites in April 2003, acknowledging the slightly higher risk for the potentially greater science return at Gusev. MER-A, Spirit will land in Gusev crater on 4 January 2004 and MER-B, Opportunity will land at Meridiani Planum on 25 January 2004.

[152] **Acknowledgments.** Landing site selection was enabled by the unselfish sharing of information by MGS and Mars Odyssey instrument Principal Investigators. In particular, we thank D. Smith and M. Zuber for providing MOLA data, J. Garvin and G. Neumann for providing processed MOLA pulse spread data, and B. Jakosky, M. Mellon and S. Pelkey for providing processed TES thermal inertia and albedo data, all before general data release or publication. The site selection activity is particularly indebted to M. Malin and K. Edgett for successfully targeting hundreds of MOC images of potential landing sites, many of which required spacecraft ROTO maneuvers to accomplish. We thank R. Haberle and J. Schaeffer for providing the Ames MGCM results for the MER landing season and local time for definition of the atmosphere for landing as well as searching for a low-wind site, the latter also assisted by M. Richardson and S. Rafkin. We also thank J. Murphy and T. Martin for surface temperature analysis and near-surface atmospheric thermal models and M. Smith for access to the TES temperature retrievals and assistance in selecting the appropriate observations. This work was supported by the MER Project as well as grants from the Mars Data Analysis Program, National Aeronautics and Space Administration, some of which were to the Jet Propulsion Laboratory, California Institute of Technology.

References

Aharonson, O., M. T. Zuber, and D. H. Rothman, Statistics of Mars' topography from the Mars Orbiter Laser Altimeter: Slopes, correlations, and physical models, *J. Geophys. Res.*, *106*, 23,723–23,735, 2001.

Anderson, F. S., and M. P. Golombek, Using MOC and MOLA data to assess landing site safety, *Lunar Planet. Sci.* [CD-ROM], *XXXII*, abstract 2173, 2001.

Anderson, F. S., A. F. C. Haldemann, N. T. Bridges, M. P. Golombek, and G. Neumann, Analysis of MOLA data for the Mars Exploration Rover landing sites, *J. Geophys. Res.*, *108*(E12), 8084, doi:10.1029/2003JE002125, in press, 2003.

Arvidson, R. E., F. P. Seelos, K. Deal, W. Koeppen, N. O. Snider, J. M. Kieniewicz, B. M. Hynek, M. T. Mellon, and J. B. Garvin, Mantled and exhumed terrains in Terra Meridiani, Mars, *J. Geophys. Res.*, *108*(E12), 8073, doi:10.1029/2002JE001982, 2003.

Barnes, J., Midlatitude disturbances in the Martian atmosphere: A second Mars year, *J. Atmos. Sci.*, *38*, 225–234, 1981.

Bell, J. F., III, et al., Mars Exploration Rover Athena Panoramic Camera (Pancam) investigation, *J. Geophys. Res.*, *108*(E11), 8063, doi:10.1029/2003JE002070, in press, 2003.

Beyer, R. A., and A. S. McEwen, Photoclinometry measurements of meter-scale slopes for the potential landing sites of the 2003 Mars Exploration Rovers, *Lunar Planet. Sci.* [CD-ROM], *XXXIII*, abstract 1443, 2002.

Beyer, R. A., A. S. McEwen, and R. L. Kirk, Meter-scale slopes of candidate MER landing sites from point photoclinometry, *J. Geophys. Res.*, *108*(E12), 8085, doi:10.1029/2003JE002120, in press, 2003.

Bridges, J. C., et al., Selection of the landing site in Isidis Planitia of Mars probe Beagle 2, *J. Geophys. Res.*, *108*(E1), 5001, doi:10.1029/2001JE001820, 2003.

Burr, D. M., A. S. McEwen, and S. E. H. Sakimoto, Recent aqueous floods from the Cerberus Fossae, Mars, *Geophys. Res. Lett.*, *29*(1), 1013, doi:10.1029/2001GL013345, 2002a.

Burr, D. M., J. A. Grier, A. S. McEwen, and L. P. Keszthelyi, Repeated aqueous flooding from the Cerberus Fossae: Evidence for very recently extant, deep groundwater on Mars, *Icarus*, *159*, 53–73, 2002b.

Butler, B. J., 3.5-cm radar investigation of Mars and Mercury: Planetological implications, Ph.D. thesis, Calif. Inst. of Technol., Pasadena, 1994.

Cabrol, N. A., E. A. Grin, and G. Dawidowicz, Ma'adim Vallis revisited through new topographic data: Evidence for an ancient intravalley lake, *Icarus*, *123*, 269–283, 1996.

Cabrol, N. A., E. A. Grin, and R. Landheim, Ma'adim Vallis evolution: Geometry and models of discharge rate, *Icarus*, *132*, 362–377, 1998a.

Cabrol, N. A., E. A. Grin, R. Landheim, R. O Kuzmin, and R. Greeley, Duration of the Ma'adim Vallis/Gusev crater hydrologic system, *Icarus*, *133*, 98–108, 1998b.

Cabrol, N. A., et al., Exploring Gusev Crater with Spirit: Review of science objectives and testable hypotheses, *J. Geophys. Res.*, *108*(E12), 8076, doi:10.1029/2002JE002026, in press, 2003.

Campbell, B. A., R. R. Ghent, and M. K. Shepard, Limits on inference of Mars small-scale topography from MOLA data, *Geophys. Res. Lett.*, *30*(3), 1116, doi:10.1029/2002GL016550, 2003.

Christensen, P. R., Martian dust mantling and surface composition: Interpretation of thermophysical properties, *J. Geophys. Res.*, *87*, 9985–9998, 1982.

Christensen, P. R., Regional dust deposits on Mars: Physical properties, age, and history, *J. Geophys. Res.*, *91*, 3533–3545, 1986a.

Christensen, P. R., The spatial distribution of rocks on Mars, *Icarus*, *68*, 217–238, 1986b.

Christensen, P. R., and M. C. Malin, High resolution thermal imaging of Mars, *Lunar Planet. Sci.*, *XIX*, 180–181, 1988.

Christensen, P. R., and H. J. Moore, The Martian surface layer, in *Mars*, edited by H. H. Kieffer et al., pp. 686–727, Univ. of Ariz. Press, Tucson, 1992.

Christensen, P. R., et al., Detection of crystalline hematite mineralization on Mars by the Thermal Emission Spectrometer: Evidence for near-surface water, *J. Geophys. Res.*, *105*, 9632–9642, 2000.

Christensen, P. R., et al., Mars Global Surveyor Thermal Emission Spectrometer experiment: Investigation description and surface science results, *J. Geophys. Res.*, *106*, 23,823–23,871, 2001a.

Christensen, P. R., R. V. Morris, M. D. Lane, J. L. Bandfield, and M. C. Malin, Global mapping of Martian hematite mineral deposits: Remnants of water-driven processes on early Mars, *J. Geophys. Res.*, *106*, 23,873–23,886, 2001b.

Christensen, P. R., et al., Morphology and composition of the surface of Mars: Mars Odyssey THEMIS results, *Science*, *300*, 2056–2061, 2003a.

Christensen, P. R., et al., Miniature Thermal Emission Spectrometer for the Mars Exploration Rovers, *J. Geophys. Res.*, *108*(E12), 8064, doi:10.1029/2003JE002117, in press, 2003b.

Clifford, S. M., and T. J. Parker, The evolution of the Martian hydrosphere: Implications for the fate of a primordial ocean and the current state of the northern plains, *Icarus*, *154*, 40–79, 2001.

Collins, M., S. R. Lewis, P. L. Read, and F. Hourdin, Baroclinic wave transitions in the Martian atmosphere, *Icarus*, *120*, 344–357, 1996.

Crisp, J. A., M. Adler, J. R. Matijevic, S. W. Squyres, R. E. Arvidson, and D. M. Kass, Mars Exploration Rover mission, *J. Geophys. Res.*, *108*(E12), 8061, doi:10.1029/2002JE002038, 2003.

Crumpler, L. S., Southwestern Isidis Planitia, Mars: A Mars Surveyor landing site at the geologic contact between three units, *Lunar Planet. Sci.* [CD-ROM], *XXIX*, abstract 1946, 1999.

Crumpler, L., and K. Tanaka, Geology and MER target site characteristics along the southern rim of Isidis Planitia, Mars, *J. Geophys. Res.*, *108*(E12), 8080, doi:10.1029/2002JE002040, in press, 2003.

Fergason, R. L., and P. R. Christensen, Thermal inertia using THEMIS infrared data, *Lunar Planet. Sci.* [CD-ROM], *XXIV*, abstract 1785, 2003.

Garvin, J. B., J. J. Frawley, and J. B. Abshire, Vertical roughness of Mars from Mars Orbiter Laser Altimeter, *Geophys. Res. Lett.*, *26*, 381–384, 1999.

Golombek, M., and D. Rapp, Size-frequency distributions of rocks on Mars and Earth analog sites: Implications for future landed missions, *J. Geophys. Res.*, *102*, 4117–4129, 1997.

Golombek, M. P., R. A. Cook, H. J. Moore, and T. J. Parker, Selection of the Mars Pathfinder landing site, *J. Geophys. Res.*, *102*, 3967–3988, 1997a.

Golombek, M. P., et al., Overview of the Mars Pathfinder Mission and assessment of landing site predictions, *Science*, *278*, 1743–1748, 1997b.

Golombek, M. P., H. J. Moore, A. F. C. Haldemann, T. J. Parker, and J. T. Schofield, Assessment of Mars Pathfinder landing site predictions, *J. Geophys. Res.*, *104*, 8585–8594, 1999.

Golombek, M., et al., Preliminary engineering constraints and potential landing sites for the Mars Exploration Rovers, *Lunar Planet. Sci.* [CD-ROM], *XXXII*, abstract 1234, 2001.

Golombek, M., et al., Downselection of landing sites for the Mars Exploration Rovers, *Lunar Planet. Sci.* [CD-ROM], *XXXIII*, abstract 1245, 2002.

Golombek, M., et al., Selection of the final four landing sites for the Mars Exploration Rovers, *Lunar Planet. Sci.* [CD-ROM], *XXXIIII*, abstract 1754, 2003a.

Golombek, M. P., A. F. C. Haldemann, N. K. Forsberg-Taylor, E. N. DiMaggio, R. D. Schroeder, B. M. Jakosky, M. T. Mellon, and J. R. Matijevic, Rock size-frequency distributions on Mars and implications for Mars Exploration Rover landing safety and operations, *J. Geophys. Res.*, *108*(E12), 8086, doi:10.1029/2002JE002035, 2003b.

Gorevan, S., et al., Rock Abrasion Tool Mars Exploration Rover Mission, *J. Geophys. Res.*, *108*(E12), 8068, doi:10.1029/2003JE002061, in press, 2003.

Greeley, R., and J. E. Guest, Geologic map of the eastern equatorial region of Mars, *U.S. Geol. Surv. Misc. Geol. Invest. Map, I-1802B*, 1987.

Greeley, R., R. O. Kuzmin, S. C. R. Rafkin, T. I. Michaels, and R. Haberle, Wind-related features in Gusev crater, Mars, *J. Geophys. Res.*, *108*(E12), 8087, doi:10.1029/2002JE002006, 2003.

Haberle, R. M., M. M. Joshi, J. R. Murphy, J. R. Barnes, J. T. Schofield, G. Wilson, M. Lopez-Valverde, J. L. Hollingsworth, A. F. C. Bridger, and J. Schaeffer, General circulation model simulations of the Mars Pathfinder atmospheric structure investigation/meteorology data, *J. Geophys. Res.*, *104*, 8957–8974, 1999.

Haldemann, A. F., and F. S. Anderson, Mars Exploration Rover landing site hectometer slopes, *Eos Trans. AGU*, *83*(47), Fall Meet. Suppl., Abstract P22A-0390, 2002.

Haldemann, A. F. C., D. L. Mitchell, R. F. Jurgens, M. A. Slade, and D. O. Muhleman, Mars Pathfinder landing site assessment with Goldstone delay-Doppler and CW radar experiments, *J. Geophys Res.*, *102*, 4097–4106, 1997.

Haldemann, A. F. C., K. W. Larsen, R. F. Jurgens, M. A. Slade, B. J. Butler, R. E. Arvidson, and J. K. Harmon, Gusev and Meridiani will look different: Radar scattering properties of the Mars Exploration Rover landing sites, paper presented at the Sixth International Conference on Mars, abstract 3272, Lunar and Planet. Inst., Pasadena, Calif., July 2003.

Harmon, J. K., R. E. Arvidson, E. A. Guinness, B. A. Campbell, and M. A. Slade, Mars mapping with delay-Doppler radar, *J. Geophys. Res.*, *104*, 14,065–14,089, 1999.

Head, J. W., H. Hiesinger, M. A. Ivanov, M. A. Kreslavsky, S. Pratt, and B. J. Thomson, Possible ancient oceans on Mars: Evidence from Mars Orbiter Laser Altimeter data, *Science*, *286*, 2134–2137, 1999.

Herkenhoff, K., et al., Athena Microscopic Imager investigation, *J. Geophys. Res.*, *108*(E12), 8065, doi:10.1029/2003JE002076, 2003.

Hollingsworth, J. L., R. M. Haberle, J. R. Barnes, A. F. C. Brider, J. B. Pollack, H. Lee, and J. Schaeffer, Orographic control of storm zones on Mars, *Nature*, *380*, 413–416, 1996.

Hynek, B. M., and R. J. Phillips, Evidence for extensive denudation of the Martian highlands, *Geology*, *29*, 407–410, 2001.

Hynek, B. M., R. E. Arvidson, and R. J. Phillips, Geologic setting and origin of Terra Meridiani hematite deposits on Mars, *J. Geophys. Res.*, *107*(E10), 5088, doi:10.1029/2002JE001891, 2002.

Irwin, R. P., I. T. A. Maxwell, A. D. Howard, R. A. Craddock, and D. W. Leverington, A large paleolake basin at the head of Ma'adim Vallis, Mars, *Science*, *296*, 2209–2212, 2002.

Ivanov, A. B., and J. J. Lorre, Analysis of Mars Orbiter Camera stereo pairs, *Lunar Planet. Sci.* [CD-ROM], *XXXIII*, abstract 1845, 2002.

Jakosky, B. M., On the thermal properties of Martian fines, *Icarus*, *66*, 117–124, 1986.

Jakosky, B. M., and P. R. Christensen, Global duricrust on Mars: Analysis of remote-sensing data, *J. Geophys. Res.*, *91*, 3547–3559, 1986.

Jakosky, B. M., and M. T. Mellon, High-resolution thermal inertia mapping of Mars: Sites of exobiological interest, *J. Geophys. Res.*, *106*, 23,887–23,907, 2001.

Jakosky, B. M., M. T. Mellon, H. H. Kieffer, P. R. Christensen, E. S. Varnes, and S. W. Lee, The thermal inertia of Mars from the Mars Global Surveyor Thermal Emission Spectrometer, *J. Geophys. Res.*, *105*, 9643–9652, 2000.

Jons, H.-P., Late sedimentation and late sediments in the northern lowlands on Mars, *Lunar Planet. Sci.*, *XVI*, 414–415, 1985.

Jons, H.-P., Arcuate ground undulations, gelifluxion-like features and "front tori" in the northern lowlands of Mars—What do they indicate?, *Lunar Planet. Sci.*, *XVII*, 404–405, 1986.

Joshi, M., R. Haberle, J. Hollingsworth, and D. Hinson, A comparison of MGS Phase 1 aerobraking radio occultation data and the NASA Ames Mars GCM, *J. Geophys. Res.*, *105*, 17,601–17,615, 2000.

Kass, D., J. T. Schofield, T. Michaels, S. Rafkin, M. Richardson, and A. Toigo, Analysis of atmospheric mesoscale models for entry, descent, and landing, *J. Geophys. Res.*, *108*(E12), 8090, doi:10.1029/2003JE002065, in press, 2003.

Kieffer, H. H., T. Z. Martin, A. R. Peterfreund, B. M. Jakosky, E. D. Miner, and F. D. Palluconi, Thermal and albedo mapping of Mars during the Viking Primary Mission, *J. Geophys. Res.*, *82*, 4249–4291, 1977.

Kirk, R. L., and B. Archinal, Topographic analysis of candidate Mars Exploration Rover landing sites from MOC Narrow-Angle stereoimages, *Lunar Planet. Sci.* [CD-ROM], *XXXIII*, abstract 1988, 2002.

Kirk, R. L., K. T. Thompson, T. L. Becker, and E. M. Lee, Photometric modelling for planetary cartography, *Lunar Planet. Sci.* [CD-ROM], *XXXI*, abstract 2025, 2000.

Kirk, R. L., K. T. Thompson, and E. M. Lee, Photometry of the Martian atmosphere: An improved practical model for cartography and photoclinometry, *Lunar Planet. Sci.* [CD-ROM], *XXXII*, abstract 1874, 2001.

Kirk, R., E. Howington-Kraus, B. Redding, D. Galuszka, T. M. Hare, B. Archinal, L. A. Soderblom, and J. Barrett, High-resolution topomapping of candidate MER landing sites with Mars Orbiter Camera narrow-angle images, *J. Geophys. Res.*, *108*(E12), 8088, doi:10.1029/2003JE002131, in press, 2003.

Klingelhöfer, G., et al., Athena MIMOS II Mössbauer spectrometer investigation, *J. Geophys. Res.*, *108*(E12), 8067, doi:10.1029/2003JE002138, in press, 2003.

Kreslavsky, M. A., and J. W. Head III, Kilometer-scale slopes on Mars and their correlation with geologic units: Initial results from Mars Orbiter Laser Altimeter (MOLA) data, *J. Geophys. Res.*, *104*, 21,911–21,924, 1999.

Kreslavsky, M. A., and J. W. Head III, Kilometer-scale roughness of Mars: Results from MOLA data analysis, *J. Geophys. Res.*, *105*, 26,695–26,711, 2000.

Kuzmin, R. O., R. Greeley, R. Landheim, N. A. Cabrol, and J. Farmer, Geologic map of the MTM-15182 and MTM 15187 Quadrangles, Gusev crater-Ma'adim Valles Region, Mars, *U.S. Geol. Sur. Misc. Geol. Invest. Map*, *I-2666*, 2000.

Lane, M. D., R. V. Morris, S. A. Mertzman, and P. R. Christensen, Evidence for platy hematite grains in Sinus Meridiani, Mars, *J. Geophys. Res.*, *107*(E12), 5126, doi:10.1029/2001JE001832, 2002.

Malin, M. C., and K. S. Edgett, Mars Global Surveyor Mars Orbiter Camera: Interplanetary cruise through primary mission, *J. Geophys. Res.*, *106*, 23,429–23,570, 2001.

Martin, T. Z., N. T. Bridges, and J. R. Murphy, Near-surface temperatures at proposed Mars Exploration Rover landing sites, *J. Geophys. Res.*, *108*(E12), 8089, doi:10.1029/2003JE002063, 2003.

Masursky, H. H., and N. L. Crabill, The Viking landing sites: Selection and certification, *Science*, *193*, 809–812, 1976a.

Masursky, H. H., and N. L. Crabill, Search for the Viking 2 landing site, *Science*, *194*, 62–68, 1976b.

Masursky, H. H., and N. L. Crabill, Viking site selection and certification, *Rep. SP-429*, 34 pp., NASA, Washington, D. C., 1981.

McEwen, A., P. Lanagan, R. Beyer, L. Keszthelyi, and D. Burr, Potential 2003 landing sites in the Cerberus plains, SE Elysium Planitia (abstract), in *First Landing Site Workshop for the 2003 Mars Exploration Rovers*, *Contrib. 1079*, pp. 51–52, Lunar and Planet. Inst., Houston, Tex., 2001.

Mellon, M. T., B. M. Jakosky, H. H. Kieffer, and P. R. Christensen, High-resolution thermal inertia mapping from the Mars Global Surveyor Thermal Emission Spectrometer, *Icarus*, *148*, 437–455, 2000.

Milam, K. A., K. R. Stockstill, J. E. Moersch, H. Y. McSween Jr., L. L. Tornabene, A. Ghosh, M. B. Wyatt, and P. R. Christensen, THEMIS characterization of the MER Gusev crater landing site, *J. Geophys. Res.*, *108*(E12), 8078, doi:10.1029/2002JE002023, in press, 2003.

Minitti, M. E., J. F. Mustard, and M. J. Rutherford, Effects of glass content and oxidation on the spectra of SNC-like basalts: Applications to Mars remote sensing, *J. Geophys. Res.*, *107*(E5), 5030, doi:10.1029/2001JE001518, 2002.

Moore, H. J., and B. M. Jakosky, Viking landing sites, remote sensing observations, and physical properties of Martian surface materials, *Icarus*, *81*, 164–184, 1989.

Moore, H. J., and J. M. Keller, Surface material maps of the Viking landing sites on Mars (abstract), in *Reports of Planetary Geology and Geophysics Program—1989*, *Tech. Mem. 4210*, pp. 533–535, NASA, Washington, D. C., 1990.

Moore, H. J., and J. M. Keller, Surface material maps of the Viking landing sites on Mars (abstract), in *Reports of Planetary Geology and Geophysics Program—1990*, *Tech. Mem. 4300*, pp. 160–162, NASA, Washington, D. C., 1991.

Moore, H. J., and T. W. Thompson, A radar-echo model for Mars, *Proc. Lunar Planet. Sci. Conf.*, *21st*, 457–472, 1991.

Moore, H. J., D. B. Bickler, J. A. Crisp, H. J. Eisen, J. A. Gensler, A. F. C. Haldemann, J. R. Matijevic, L. K. Reid, and F. Pavlics, Soil-like deposits observed by Sojourner, the Pathfinder rover, *J. Geophys. Res.*, *104*, 8729–8746, 1999.

Neumann, G. A., J. B. Abshire, O. Aharonson, J. B. Garvin, X. Sun, and M. T. Zuber, Mars Orbiter Laser Altimeter pulse width measurements and footprint-scale roughness, *Geophys. Res. Lett.*, *30*(11), 1561, doi:10.1029/2003GL017048, 2003.

Noreen, E., K. L. Tanaka, and M. G. Chapman, TES hematite landing sites in Sinus Meridiani for 2003 Mars Exploration Rover, paper presented at the 2003 MER Landing Site Workshop, abstract 9014, Lunar and Planet. Inst., Houston, Tex., 2001.

Nowicki, S. A., and P. R. Christensen, Mars surface rock abundance from Thermal Emission Spectrometer (TES) mapping data, paper presented at the Fifth International Conference on Mars, abstract 6191, Lunar and Planet. Inst., Pasadena, Calif., 18–23 July 1999.

Palluconi, F. D., and H. H. Kieffer, Thermal inertia mapping from 60°S to 60°N, *Icarus*, *45*, 415–426, 1981.

Parker, T. J., R. S. Saunders, and D. M. Schneeberger, Transitional morphology in the west Deuteronilus Mensae region of Mars: Implications for modification of the lowland/upland boundary, *Icarus*, *82*, 111–145, 1989.

Parker, T. J., D. S. Gorsline, R. S. Saunders, D. C. Pieri, and D. M. Schneeberger, Coastal geomorphology of the Martian northern plains, *J. Geophys. Res.*, *98*, 11,061–11,078, 1993.

Pelkey, S. M., and B. M. Jakosky, Surficial geologic surveys of Gale Crater and Melas Chasma, Mars: Integration of remote sensing data, *Icarus*, *160*, 228–257, 2002.

Phillips, R. J., et al., Ancient geodynamics and global-scale hydrology on Mars, *Science*, *291*, 2587–2591, 2001.

Pleskot, L. K., and E. D. Miner, Time variability of Martian bolometric albedo, *Icarus*, *45*, 179–201, 1981.

Pollack, J. B., C. B. Leovy, Y. H. Mintz, and W. Van Camp, Winds on Mars during the Viking season: Predictions based on a general circulation model with topography, *Geophys. Res. Lett.*, *3*, 479–483, 1976.

Pollack, J. B., R. M. Haberle, J. Schaeffer, and H. Lee, Simulations of the general circulation of the Martian atmosphere: 1. Polar processes, *J. Geophys. Res.*, *95*, 1447–1473, 1990.

Rafkin, S. C. R., and T. I. Michaels, Meteorological predictions for 2003 Mars Exploration Rover high-priority landing sites, *J. Geophys. Res.*, *108*(E12), 8091, doi:10.1029/2002JE002027, 2003.

Richardson, M. I., and R. J. Wilson, Investigation of the nature and stability of the Martian seasonal water cycle with a general circulation model, *J. Geophys. Res.*, *107*(E5), 5031, doi:10.1029/2001JE001536, 2002.

Rieder, R., R. Gellert, J. Brückner, G. Klingelhöfer, G. Dreibus, A. Yen, and S. W. Squyres, The new Athena alpha particle X-ray spectrometer for the Mars Exploration Rovers, *J. Geophys. Res.*, *108*(E12), 8066, doi:10.1029/2003JE002150, 2003.

Ruff, S. W., and P. R. Christensen, Bright and dark regions on Mars: Particle size and mineralogical characteristics based on Thermal Emission Spectrometer data, *J. Geophys. Res.*, *107*(E12), 5127, doi:10.1029/2001JE001580, 2002.

Schofield, J. T., et al., The Mars Pathfinder atmospheric structure investigation meteorology (ASI/MET) experiment, *Science*, *278*, 1752–1758, 1997.

Scott, D. H., and K. L. Tanaka, Geologic map of the western equatorial region of Mars, *U.S. Geol. Surv. Misc. Geol. Invest. Map, I-1802A*, 1986.

Shepard, M. K., B. A. Campbell, M. H. Bulmer, T. G. Farr, L. R. Gaddis, and J. J. Plaut, The roughness of natural terrain: A planetary and remote sensing perspective, *J. Geophys. Res.*, *106*, 32,777–32,795, 2001.

Simpson, R. A., J. K. Harmon, S. H. Zisk, T. W. Thompson, and D. O. Muhleman, Radar determination of Mars surface properties, in *Mars*, edited by H. H. Kieffer et al., pp. 652–685, Univ. Ariz. Press, Tucson, 1992.

Smith, D. E., and M. T. Zuber, The relationship between MOLA northern hemisphere topography and the 6.1-mbar atmospheric pressure surface of Mars, *Geophys. Res. Lett.*, *25*, 4397–4400, 1998.

Smith, D. E., et al., Mars Orbiter Laser Altimeter: Experiment summary after the first year of global mapping of Mars, *J. Geophys. Res.*, *106*, 23,689–23,722, 2001a.

Smith, M. D., J. C. Pearl, B. J. Conrath, and P. R. Christensen, Thermal Emission Spectrometer results: Mars atmospheric thermal structure and aerosol distribution, *J. Geophys. Res.*, *106*, 23,929–23,945, 2001b.

Soderblom, L. A., and R. L. Kirk, Meter-scale 3D models of the Martian surface from combining MOC and MOLA data, *Lunar Planet. Sci.* [CD-ROM], *XXXIV*, abstract 1730, 2003.

Squyres, S. W., et al., Athena Mars Rover science investigation, *J. Geophys. Res.*, *108*(E12), 8062, doi:10.1029/2003JE002121, in press, 2003.

Tanaka, K., J. Skinner, and T. Hare, Geology of the "Elysium" Mars Exploration Rover candidate landing site in southeastern Utopia Planitia, *Eos Trans. AGU*, *83*(47), Fall Meet. Suppl., Abstract P22A-0388, 2002.

Tanaka, K. L., M. H. Carr, J. A. Skinner, M. S. Gilmore, and T. M. Hare, Geology of the MER 2003 "Elysium" candidate landing site in southeastern Utopia Planitia, Mars, *J. Geophys. Res.*, *108*(E12), 8079, doi:10.1029/2003JE002054, in press, 2003.

Toigo, A. D., and M. I. Richardson, Meteorology of proposed Mars Exploration Rover landing sites, *J. Geophys. Res.*, *108*(E12), 8092, doi:10.1029/2003JE002064, in press, 2003.

Tyler, G. L., G. Balmino, D. P. Hinson, W. L. Sjogren, D. E. Smith, R. A. Simpson, S. W. Asmar, P. Priest, and J. D. Twicken, Radio science observations with Mars Global Surveyor: Orbit insertion through one Mars year in mapping orbit, *J. Geophys. Res.*, *106*, 23,327–23,348, 2001.

U.S. Geological Survey, Mission to Mars: Digital image maps, vers. 2.0, PDS vol. VO_2001 V2-VO_2006 V2, 2001.

Weitz, C. M., T. J. Parker, M. H. Bulmer, F. S. Anderson, and J. A. Grant, Geology of the Melas Chasma landing site for the Mars Exploration

Rover, *J. Geophys. Res.*, *108*(E12), 8082, doi:10.1029/2002JE002022, in press, 2003.

Zurek, R. W., et al., Dynamics of the atmosphere of Mars, in *Mars*, edited by H. H. Kieffer et al., chap. 26, pp. 835–933, Univ. Ariz. Press, Tucson, 1992.

M. Adler, N. T. Bridges, J. A. Crisp, M. P. Golombek, A. F. C. Haldemann, D. M. Kass, P. C. Knocke, W. J. Lee, T. J. Parker, R. B. Roncoli, J. T. Schofield, and R. W. Zurek, Jet Propulsion Laboratory, California Institute of Technology, 4800 Oak Grove Drive, Pasadena, CA 91109 USA. (joy@glassy.jpl.nasa.gov; nathan.bridges@jpl.nasa.gov; joy.crisp@jpl.nasa.gov; mgolombek@jpl.nasa.gov; albert@shannon.jpl.nasa.gov; david.m.kass@jpl.nasa.gov; philip.c.knocke@jpl.nasa.gov; wayne@cranberry.jpl.nasa.gov; timothy.j.parker@jpl.nasa.gov; ralph.b.roncoli@jpl.nasa.gov; tim@scn1.jpl.nasa.gov; rzurek@jpl.nasa.gov)

F. S. Anderson, Hawaii Institute of Geophysics and Planetology, School of Ocean and Earth Science and Technology, University of Hawaii, 1680 East-West Road, POST 602B, Honolulu, HI 96822, USA. (anderson@higp.hawaii.edu)

R. E. Arvidson, Department of Earth and Space Sciences, Washington University, Campus Box 1169, One Brookings Drive, St. Louis, MO 63130, USA. (arvidson@wunder.wustl.edu)

M. H. Carr, U.S. Geological Survey, Mail Stop 975, 345 Middlefield Road, Menlo Park, CA 94025, USA. (carr@usgs.gov)

P. R. Christensen, R. L. Fergason, and J. W. Rice Jr., Department of Geological Sciences, Arizona State University, Campus Box 871404, Tempe, AZ 85287-6305, USA. (phil.christensen@asu.edu; robin.fergason@asu.edu; james.rice@asu.edu)

J. A. Grant, Center for Earth and Planetary Studies, National Air and Space Museum, Smithsonian Institution, 4th and Independence SW, Washington, DC 20560-0315, USA. (grantj@nasm.si.edu)

R. L. Kirk, Geologic Division/Branch of Astrogeology, U.S. Geological Survey, 2255 North Gemini Drive, Flagstaff, AZ 86001, USA. (rkirk@usgs.gov)

S. W. Squyres, Department of Astronomy, Cornell University, 428 Space Sciences Building, Ithaca, NY 14853-6801, USA. (squyres@astrosun.tn.cornell.edu)

C. M. Weitz, NASA Headquarters, Mail Code SE,300 E Street SW, Washington, DC 20546, USA. (cweitz@hq.nasa.gov)